Title	Self-similar Solutions and the Stability of Dynamically Condensing Gas Layers : Towards Understanding of the Formation of Interstellar Clouds
Author(s)	Iwasaki, Kazunari
Citation	大阪大学, 2010, 博士論文
Version Type	VoR
URL	https://hdl.handle.net/11094/1235
rights	
Note	

Self-similar Solutions and the Stability of Dynamically Condensing Gas Layers:

Towards Understanding of the Formation of Interstellar Clouds

Kazunari Iwasaki

A thesis presented for the degree of
Doctor of Science

Theoretical Astrophysics Group,

Department of Earth and Space Science, Graduate School of Science,

Osaka University, Toyonaka OSAKA 560-0043, Japan

February, 2010

Self-similar Solutions and the Stability of Dynamically Condensing Gas Layers:

Towards Understanding of the Formation of Interstellar Clouds

(動的に凝縮するガス層を記述する自己相似解とその安定性:

星間雲形成の理解へ向けて)

Self-similar Solutions and the Stability of Dynamically Condensing Gas Layers:

Towards Understanding of the Formation of Interstellar Clouds

Kazunari Iwasaki

Submitted for the degree of Doctor of Science
February, 2010

Abstract

Since molecular clouds are birthplace of stars, understanding how molecular clouds form is crucial to determine the initial condition of star formation. One of the promising mechanisms to produce molecular clouds is thermal instability that can be induced by shock waves (e.g. supernova shocks). In one-dimensional model, thermal instability leads to a runaway cooling and condensation of thin gas layer in the shock-compressed region. A cold gas layer is generated that is precursor of molecular clouds. In order to understand the size and shape of the cold clouds, it is important to investigate multi-dimensional behavior of the condensing layer. Linear analyses in previous works predict that the condensing layer splits into fragments with smaller scales than the cooling length that the sound wave travels during the cooling. However, two-dimensional simulations show that many fragments are larger than the cooling length. This contradicts with linear analyses in previous works. This is because the unperturbed states in previous works were assumed to be spatially uniform and/or their time dependences were neglected for simplicity. Therefore, they cannot describe the dynamically condensing layer well.

In this thesis, first, we propose new self-similar solutions describing runaway cooling gas layers as the more realistic unperturbed state. We confirm that the self-similar solutions approximate results of hydrodynamical numerical simulations using a realistic cooling rate of the interstellar medium very well. A net cooling rate per unit mass is assumed to be $\propto \rho T^{\alpha}$, where ρ, T and α are density, temperature and an index parameter, respectively. Given α, we find a family of self-similar solutions with another free parameter η that ranges from 0 to 1. The parameter η relates with the ratio of the cooling length to the scale length of the condensing region. For $\eta \sim 0$, the scale length of the condensing region is much larger than the cooling length. Therefore, the temperature drops while the density does not increase so much. This solution describes isochorically cooling layer. On the other hand, for $\eta \sim 1$, the scale length of the condensing region is much smaller than the cooling length. Therefore the gas condenses in pressure equilibrium with their surroundings. This solution describes isobarically condensing layer. The discovered family of the self-similar solutions describes the nonlinear developments of thermal instability in various scales in the one-dimensional model.

Second, the stability of the dynamically condensing layer is investigated by linear analysis of the self-similar solutions. We consider perturbations perpendicular, as well as parallel, to the direction of the condensation. The linear analysis reveals that the growth rate of the perturbation is independent of their transverse scales. Moreover, since the growth rate is sufficiently high, it is not long before the perturbations become nonlinear during the runaway condensation. Therefore, according to the linear analysis, the condensing layer is expected to split into fragments with various scales. These results are quite different from those in previous works. This linear analysis predicts the mass distribution of generated cold clouds is correlated with the power spectrum of fluctuations of the unstable gas. These results and predictions of the linear analysis are confirmed by two-dimensional hydrodynamical simulation with realistic cooling rate of the interstellar medium.

Acknowledgements

The author would like to thank Dr. Toru Tsuribe for his continuous support and encouragement. The thesis could not have been accomplished without his support. The author would like to thank Professor Dr. Fumio Takahara for his careful reading of this manuscript and numerous constructive remarks. He is also grateful to Dr. Tsuyoshi Inoue and Professor Dr. Shu-ichiro Inutsuka for valuable discussions about this research project. Moreover, he wishes to thank Dr. Yutaka Fujita and Dr. Hideyuki Tagoshi for variable supports and advises over the doctoral course. He would like to express deep gratitude to past and present members of theoretical astrophysics group. Finally, the author wishes to thank to his parents for their unconditional supports both before and during the doctoral course.

This work was in part supported by the 21st Century COE Program "Towards a New Basic Science; Depth and Synthesis" in Osaka University, funded by the Ministry of Education, Science, Sports and Culture of Japan. The author is supported by grants-in-aid for JSPS Fellow (21-1979).

Contents

Chapter 1

Introduction

The most amount of volume of galaxies is occupied by gases and dusts that exist between stars and they are called interstellar medium (ISM). The ISM and stars mutually affect each other. Stars supply matters and energies to the ISM via stellar wind, planetary nebulae, supernovae, and radiation. In contrast, a dense and cold component of the ISM is the birthplace of stars whose formation mechanism is one of the most important unresolved issues in astrophysics. Therefore, the ISM is a critical element to understand physical phenomena in galaxies. In this thesis, to understand initial condition of the star formation, we investigate the formation of cold clouds by considering basic physics of the ISM.

In this chapter, we review observational and theoretical background of this thesis, and present purposes of this thesis.

1.1 Overview of Interstellar Medium

Thanks to development of radio, infrared, optical, and X-ray observations, it has been revealed that the ISM consists of not one component but several components that are classified by their densities, temperatures and ionization degrees that are summarized in table 1.1. Hot ionized medium (HIM) with number density $n \sim 3 \times 10^{-3}$ cm^{-3} and temperature $T \sim 10^6$ K is made up of completely ionized hot gas, and is also called coronal gas. The HIM is produced by supernova shocks (McKee and Ostriker, 1977). There are two components that are made up of neutral hydrogen atom. One is warm and diffuse component with $n \sim 0.3$ cm^{-3} and $T \sim 8000$ K that is called warm neutral medium (WNM). The other is cold and dense component with $n \sim 30$ cm^{-3} and $T \sim 10^2$ K that is called cold neutral medium (CNM). The CNM is also called HI cloud, where "HI" denotes neutral hydrogen atom. The HIM and WNM occupy the most volume of the ISM. Figure 1.1 shows schematic plot of components of the ISM in (n, T) plane that was originally presented by Myers (1977). The upper and lower solid lines correspond to $P/k_{\rm B} = 10^2$ and 10^4 K cm^{-3}, respectively. Figure 1.1 indicates that the three "phases", HIM, WNM and CNM are roughly in pressure equilibrium with $P/k_{\rm B} = nT \sim 3 \times 10^3$ K cm^{-3} in the solar vicinity. The term of "phase" is used to denote that HIM, WNM and CNM can coexist in the same pressure. Molecular clouds are mainly made up of H_2 and are dense and cold enough to be gravitationally bound. Because of its self-gravity, the pressure of the molecular cloud is much larger than that of the three phases (see figure 1.1). The densest part of the molecular cloud, or the dense core, leads to gravitational collapse and finally stars form. HII region is produced by ionizing photons with $h\nu \geq 13.6$ eV emitted by massive stars, where "HII" denotes ionized hydrogen atom. HII region expands because its pressure is much larger than that of surrounding medium.

Component	n [cm^{-3}]	T [K]	nT [K cm^{-3}]	state of H
Hot Ionized Medium (HIM) Coronal Gas	$\sim 3 \times 10^{-3}$	$\sim 10^6$	$\sim 3 \times 10^3$	ionized
Warm Neutral Medium (WNM)	~ 0.3	~ 8000	$\sim 2.4 \times 10^3$	neutral
Cold Neutral Medium (CNM) HI Cloud	~ 30	~ 100	$\sim 3.0 \times 10^3$	neutral
Molecular Cloud	$\sim 10^3 - 10^7$	~ 10	$\sim 10^4 - 10^8$	molecule
HII Region	$\sim 10 - 10^5$	$\sim 10^4$	$\sim 10^5 - 10^9$	ionized

Table 1.1: Physical properties of components in the ISM

1.2 Observations

The physical properties and structures of the ISM have been revealed though observations with a wide range of wavelength, from radio to X-ray.

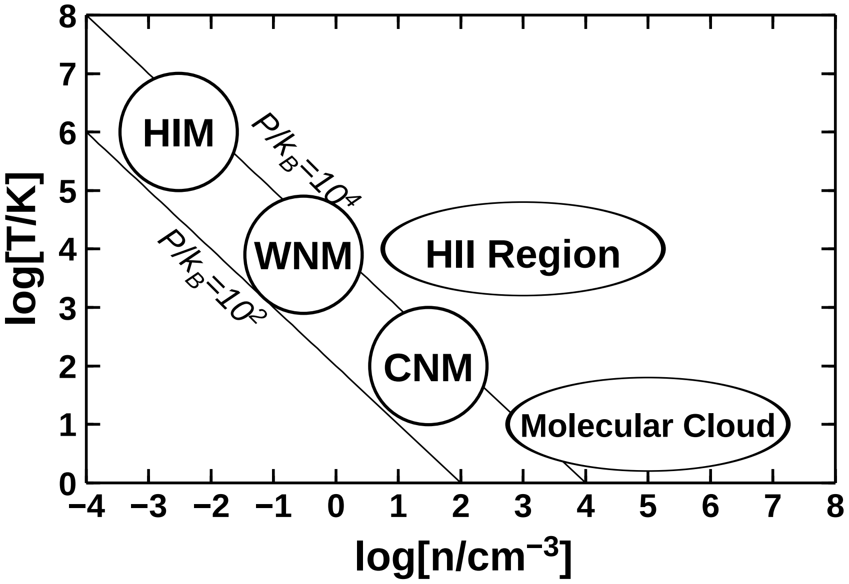

Figure 1.1: Schematic plot of components in the ISM in (n, T) plane. The upper and lower solid lines correspond to $P/k_\mathrm{B} = 10^2$ and 10^4 K cm^{-3}, respectively. This was originally presented by Myers (1977).

1.2.1 HI Gas (Cold Neutral and Warm Neutral Media)

The ground state of neutral atomic hydrogen has hyperfine lines arising from the interaction between the spins of electron and proton. The corresponding wavelength is 21 cm at radio regime. The ISM was first detected by the 21-cm line emission (Ewen and Purcell, 1951; Muller and Oort, 1951). This observation suggests that there is a large amount of neutral hydrogen in the Galaxy. Absorption line of HI gas was also observed by Hagen and McClain (1954) against bright continuum sources, and was confirmed by Hagen, Lilley, and McClain (1955). After the first detection, in 1950s, observations showed broad emission lines and narrow absorption lines in the same part of sky (Clark, Radhakrishnan, and Wilson, 1962). From these observations, Clark (1965) suggested that the ISM is not single component but is made up of cold and warm components that generate the narrow absorption lines and broad emission lines, respectively. The cold dense cloud (cold neutral medium, CNM) is embedded within a bath of warm diffuse medium (warm neutral medium, WNM), and these two components are in pressure equilibrium. This picture of ISM was theoretically supported by Field, Goldsmith, and Habing (1969) as shown in section 1.4.

Global Structure

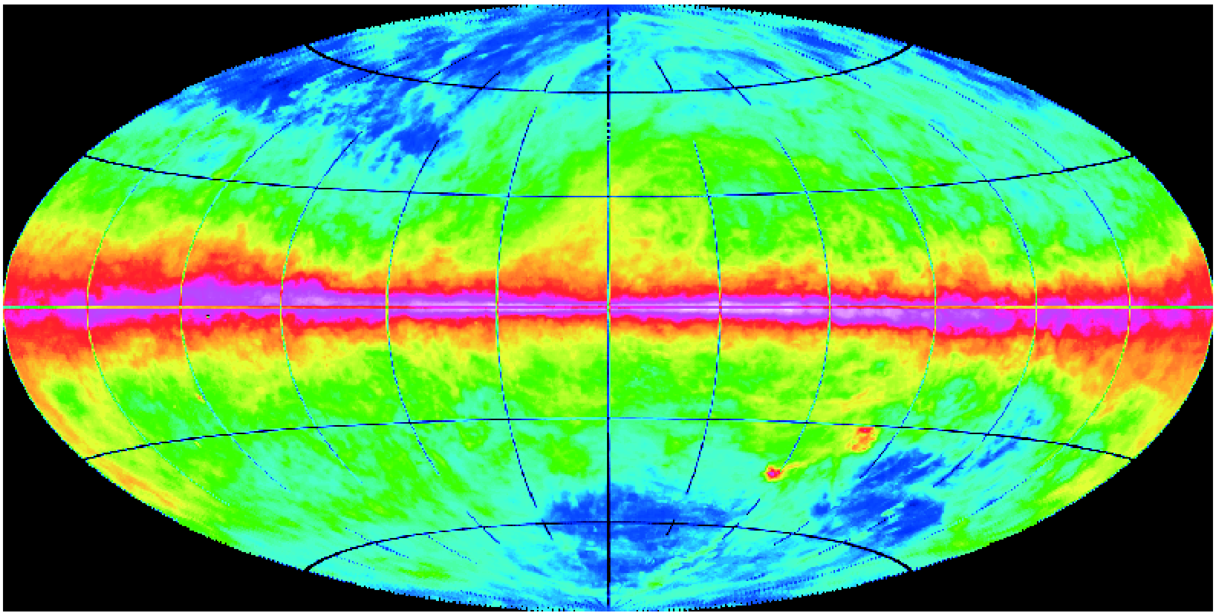

Figure 1.2: HI emission integrated over the velocity range of $-400 < v < 400$ km s^{-1}. The Galactic center is in the middle. The ordinate and abscissa axes denote Galactic latitude and longitude, respectively. The figure was presented in Kalberla et al. (2005).

Oort, Kerr, and Westerhout (1958) discovered that HI clouds are distributed in several spiral arms, suggesting that the Galaxy is a spiral galaxy (see also Kerr, 1969). They also derived the flat rotation curve of the Galaxy. The first survey of 21 cm emission has been presented by Weaver and Williams (1973) with the 85-foot telescope at the Hat Creek Observatory. Using the data of their survey, Heiles (1984, 1979) found HI shells and supershells in the northern sky (McClure-Griffiths et al., 2002, in the southern sky). Recently, Kalberla et al. (2005) presented observations of 21 cm emission from Galactic neutral hydrogen over the entire sky, that is referred to Leiden/Argentine/Bonn (LAB) survey. HI emission integrated over the velocity range $-400 < v < +400$ km s^{-1} is shown in figure 1.2 presented in Kalberla et al. (2005). The Galactic center is in the middle. From figure 1.2, it is clearly seen that HI gas concentrates in the Galactic plane. The thickness of HI gas in the solar vicinity is as high as ~ 200 pc. Moreover, figure 1.2 show that the shells, shell-like and filamentary structures are ubiquitous in the Galaxy with a very broad range of size (> 1 kpc ~ 1 pc). These shell structures are attributed to supernovae, the impact of infalling high-velocity clouds on the Galaxy disc, stellar winds, and molecular outflows.

These observations show that the ISM is frequently disturbed by energetic phenomena, such as supernovae, and is far from quiescent (McKee and Ostriker, 1977). Recently, surprisingly tiny and discrete HI clouds in the diffuse ISM have been discovered by Braun and Kanekar (2005); Stanimirović and Heiles (2005). This new population of HI clouds has very small sizes of $\sim 10^{-2}$ pc, and small column density of $\sim 10^{18}$ cm^{-2}.

1.2.2 Coronal Gas (Hot Ionized Medium)

Soft X-ray Background

The coronal gas was first detected by observations of soft X-ray background using an Aerobee rocket. Bowyer, Field, and Mack (1968) found an anisotropy of the soft X-ray background at 0.25 keV, and suggested that an anisotropic component is originated in sources in the Galaxy. This soft X-ray emission is attributed to Bremsstrahlung from rarefied and hot gas at $T \sim 10^6$ K. The soft X-ray background consists of different components that are extragalactic components for high energy > 10 keV, galactic components for low energy < 0.25 keV, and mixture of extragalactic and galactic for the intermediate energy (McCammon and Sanders, 1990).

Absorption Lines

The coronal gas is also observed as an absorption line, such as lithium-like atoms (O VI, N V, and C IV) at ultraviolet. Jenkins and Meloy (1974); Rogerson et al. (1973) discovered discovery of O VI absorption line toward O and B stars using *Copernicus* satellite, suggesting a large amount of very hot ($T \sim 10^6$ K) and tenuous component (hot ionized medium, HIM) Recently, observation with with *Far-Ultraviolet Spectroscopic Explorer (FUSE)* satellite has revealed kinematics and distribution of the HIM. Savage et al. (2000) observed O VI absorption line against far-ultraviolet spectra of active galactic nuclei. They showed that the scale height of the hot component is as high as $\sim$ 3kpc that is much higher than other components.

1.2.3 Molecular Cloud

As a tracer of molecular clouds, the emission lines of rotational transitions of carbon monoxide (CO) are used because hydrogen molecule that is main component does not have the electric dipole moment. The CO line emission was first detected by Wilson, Jefferts, and Penzias (1970) in the Orion Nebula at a frequency of 115GHz that corresponds to the transition from $J = 1$ to $J = 0$. Dame et al. (1987, 2001) performed large-scale CO surveys of molecular clouds in the Galaxy with a 1.2 m telescope in New York City and Cerro Tololo, Chile. The large scale structures of molecular clouds have been revealed by their survey. Figure 1.3 shows their velocity integrated CO map of the Galaxy. The molecular clouds concentrate in the Galactic disc and are distributed along the spiral arms like HI gas. The scale height of molecular clouds is as high as ~ 100 pc and is lower than that of HI clouds.

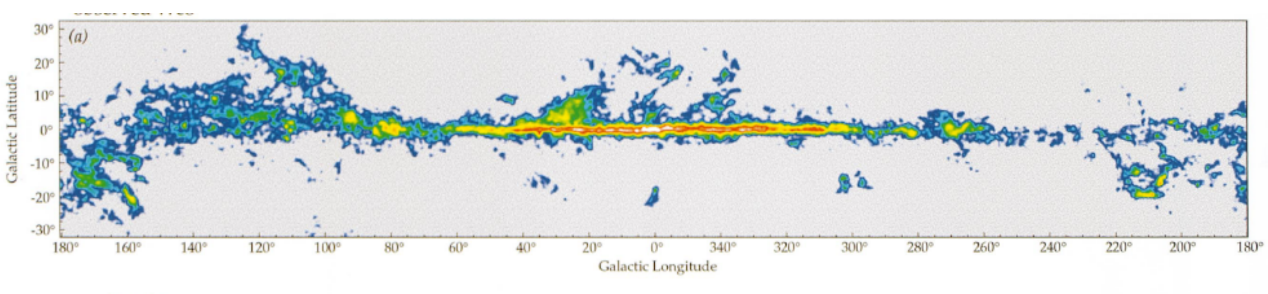

Figure 1.3: Velocity integrated CO map of the Galaxy. The Galactic center is in the middle. The ordinate and abscissa axes denote Galactic latitude and longitude, respectively. The figure was presented in Dame et al. (2001).

1.2.4 Supersonic Turbulence

The supersonic turbulent motion has been ubiquitously observed in the cold component of the ISM, or HI clouds and molecular clouds. Heiles and Troland (2003) presented Arecibo 21 cm absorption-line survey against intense radio continuum sources. They found that the mass-weighted velocity dispersion is 7.1 $\mathrm{km\,s^{-1}}$ for CNM and 11.4 $\mathrm{km\,s^{-1}}$ for WNM. The mass-weighted velocity dispersion of CNM is supersonic because the sound speed of CNM is ~ 1 $\mathrm{km\,s^{-1}}$. The mass-weighted velocity dispersion of WNM is marginally supersonic because the sound speed of WNM is ~ 8 $\mathrm{km\,s^{-1}}$. Combining many observations with 21-

cm and molecular lines, Larson (1979, 1981) discovered the velocity dispersion of the ISM increases systematically with region sizes, and derived the following empirical relation,

$$\Delta v \simeq 1 \text{ km s}^{-1} \left(\frac{L}{1 \text{ pc}}\right)^{0.38}, \tag{1.1}$$

where Δv and L are the velocity dispersion and the region size, respectively. Since the energy of the turbulent motion is comparable to the gravitational and magnetic energies in molecular clouds, the supersonic turbulent motion is expected to play an important role of star formation. However, the formation mechanism of the supersonic turbulent motion is not understood yet. As mentioned later, thermal instability of the ISM is a possible mechanism (Koyama and Inutsuka, 2002). Moreover, there is a problem of how to maintain the supersonic motion. Theoretically, supersonic isothermal magnetohydrodynamical turbulence decays rapidly in times of the dynamical time if there is not any continuous energy input (Gammie and Ostriker, 1996; Mac Low et al., 1998; Padoan and Nordlund, 1999). This decaying time scale ($\sim 10^{5-6}$yr) is several times smaller than the lifetime of molecular clouds ($\sim 10^7$yr). Therefore, some driving forces of supersonic turbulence are required. Many authors have suggested several driving sources, such as magnetorotational instability in the Galactic disk (Sellwood and Balbus, 1999), stellar outflows and winds from protostars (Franco and Cox, 1983) and thermal instability (Koyama and Inutsuka, 2002), and so on. However, the source of the supersonic turbulence is still controversial.

1.3 Cooling and Heating Processes in the Interstellar Medium

The density and temperature of the ISM are mainly determined by radiative cooling and heating due to external radiation field and cosmic rays (Field et al., 1969; Wolfire et al., 2003, 1995).

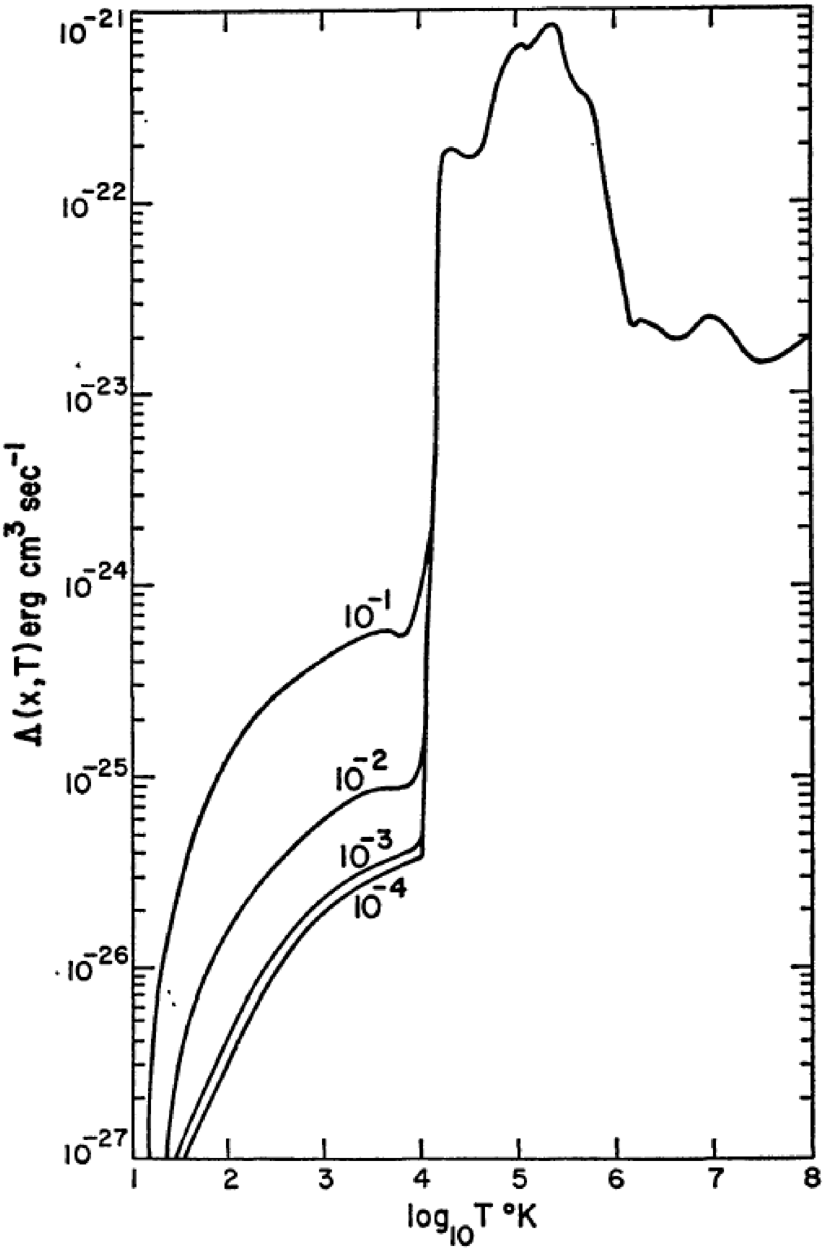

Figure 1.4: The interstellar cooling rate for a various values of the fractional ionization, x. The labels refer to the values of x. This figure was presented in Dalgarno and McCray (1972).

1.3.1 Heating Processes

Photoelectric Heating from Small Dust and Polycyclic Aromatic Hydrocarbons (PAHs)

A main heating process is the photoelectric heating from small grain and PAHs. The gas particles are heated by collision with photoelectrons expelled from dusts and PAHs by far-ultraviolet photons (Bakes and Tielens, 1994). The far-ultraviolet radiation field in the Galaxy is estimated by Habing (1968) using spectrums of O- and B-type stars and their number density in the Galaxy for the energy range of 6 eV $< h\nu <$ 13.6 eV (also see Gondhalekar and Wilson, 1975). Conventionally, the far-ultraviolet flux is expressed by G_0 in unit of the average far-ultraviolet flux of 1.6×10^{-3} erg cm^{-2} s^{-1} derived by Habing (1968). The value of G_0 depends on environments and can range from local average far-ultraviolet flux $G_0 \sim 1.7$ (Draine, 1978) to that near O- and B-type stars $G_0 \gtrsim 10^6$. In this thesis, we consider the heating by the local far-ultraviolet flux ($G_0 = 1.7$).

Cosmic Rays

Low-energy cosmic-rays ionize gas particles through collision. The cosmic-ray ionization rate is 1.8×10^{-17} s^{-1} per H nucleus that is typical value in the Galaxy (Wolfire et al., 1995). Since the ejected free electrons have a larger kinetic energy than that of thermal one, the free electron heat up surrounding gas particles through collision (Shull and van Steenberg, 1985).

Soft X-Rays

The gas particles are heated by collision with free electrons emitted due to ionization effect (Wolfire et al., 1995) by soft X-ray background (see section 1.2.2).

1.3.2 Cooling Processes

Dalgarno and McCray (1972) calculate cooling rate of low density gas enough for radiation to escape the system by considering the detailed atomic physics. In this situation, the cooling rate is determined by local physical quantities, such as the density, temperature, and ionization degrees and so on. Figure 1.4 shows the interstellar cooling rate for various values of the fractional ionization, x (Dalgarno and McCray, 1972). The labels refer to the values of x. Sutherland and Dopita (1993) presented cooling rates by considering more complex physical processes over a range of $10^4 - 10^{8.5}$ K and for a range of abundances.

- For the temperature range of $T > 10^{6-7}$ K, the gas mainly loses their energy through thermal Bremsstrahlung of completely ionized gas.

- For the temperature range of 10^4 K $< T <$ 10^6 K, a main coolant is spontaneous emission by collisionally excited gases though electronic transitions and recombination lines. This cooling process is contributed by a lot of elements that contain neutral and ionized state of H, He, O, C, S, Si, and Fe, and so on.

- For the temperature range of $T < 10^4$ K, the cooling rate suddenly drops in figure 1.4. This is because atoms cannot be excited to an upper electronic level via collision. In this temperature range, collisional excitation of the fine-structure lines of CII (158μm) and OI (63μm) are dominant coolant (Hollenbach and McKee, 1989; Wolfire et al., 1995). Additional coolings are provided by the fine-structure transitions of the ground state electronic state of CI, SiI, SiII, SI, FeI, and FeII.

1.4 Quiescent Two-Phase Model

Field, Goldsmith, and Habing (1969) proposed a model of the ISM based on detailed calculation of radiative cooling and heating by low-energy cosmic rays. Wolfire et al. (2003, 1995) revised and developed the results of Field, Goldsmith, and Habing (1969) by considering new heating source of photoelectric heating from small dusts and PAHs (Bakes and Tielens, 1994) and revised cosmic-ray ionization rate that is significant lower than that used in Field et al. (1969). Wolfire et al. (1995) plotted the thermal equilibrium curve in the (n, P) plane that is shown by the thick solid line in figure 1.5 (also see Field, Goldsmith, and Habing, 1969), where the far-ultraviolet flux is set to the local value of $G_0 = 1.7$. From figure 1.5, it is clearly seen that three phases in thermal equilibrium can coexist at the same pressure of $P/k_{\rm B} = 3 \times 10^3$ K cm^{-3} which is the value in the solar vicinity and they are shown by the open circles in figure 1.5.

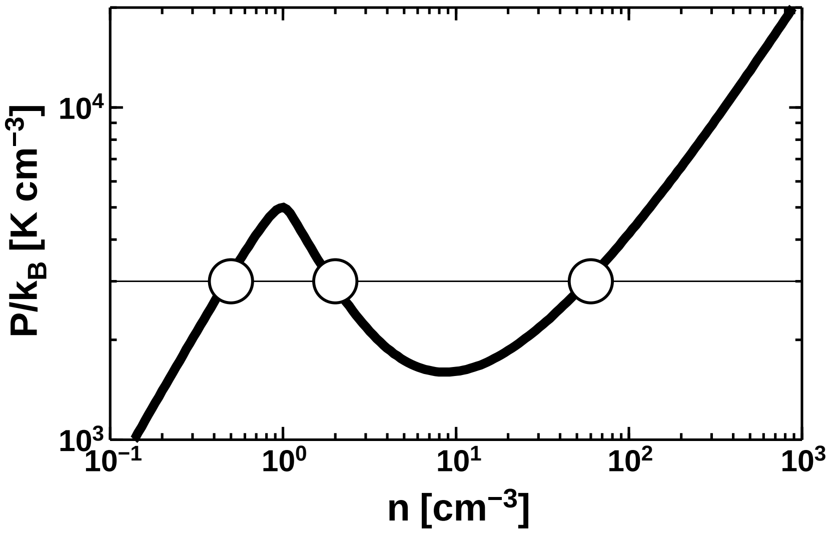

Figure 1.5: Phase diagram of thermal properties of ISM in (n, P) plane. The thick line indicates thermal equilibrium curve. The thin horizontal line corresponds to $P/k_{\rm B} = 3 \times 10^3$ K cm^{-3}.

1.4.1 Thermal Instability of Gas in Thermal Equilibrium State

Field (1965) investigated the stability of the gas in thermal equilibrium using linear analysis. He considered an uniform and static gas as the unperturbed state. In this section, we briefly review his linear analysis.

Cooling and heating rates per unit mass and time is defined as $\Lambda(\rho, T)$ and $\Gamma(\rho, T)$ (erg g^{-1} s^{-1}), respectively, as a function of density and temperature. The net cooling rate is defined as $\mathcal{L} = \Lambda - \Gamma$. As shown in section 1.3, for the low temperature range of $T < 10^4$ K, a main cooling process is spontaneous emission by collisionally excited gases. In this situation, the cooling rate per unit mass is determined by the collision rate that is proportional to ρ. The heating rate per unit mass from an external source is constant. In this thesis, we adopt the following simplified power-law formula as the net cooling rate per unit mass and time,

$$\mathcal{L}(\rho, T) = \Lambda_0 \rho T^\alpha - \Gamma_0 \ \ \text{erg g}^{-1} \text{ s}^{-1}, \tag{1.2}$$

where α is a free parameter that is determined by detailed atomic physics. As an characteristic timescale, we define cooling time by the internal energy divided by the radiative cooling as

$$t_{\rm cool} = \frac{P}{(\gamma - 1)\rho\Lambda} = \frac{C_V T}{\Lambda}, \tag{1.3}$$

where C_V is the specific heat at constant volume. The characteristic length is defined as

$$\lambda_{\mathrm{cool}} = c_{\mathrm{s}} t_{\mathrm{cool}}, \tag{1.4}$$

where c_{s} is the sound speed.

Criterion of thermal instability can be derived from simple physical arguments by focussing on a fluid element. The entropy of the fluid element evolves obeying the entropy equation,

$$\frac{\mathrm{D}S}{\mathrm{D}t} = -\frac{1}{T}\mathcal{L}(\rho, T), \qquad S = \frac{k_{\mathrm{B}}}{(\gamma - 1)\mu m_{\mathrm{H}}} \ln P\rho^{-\gamma}, \tag{1.5}$$

where S is the entropy and μ is the mean molecular weight of the gas in the unit of hydrogen mass, m_{H}. The operator $\mathrm{D}/\mathrm{D}t = \partial/\partial t + \vec{v} \cdot \vec{\nabla}$ is the Lagrangian time-derivative.

Let us perturb the fluid element. From the entropy equation (1.5), one can obtain the following perturbation equation,

$$\frac{\mathrm{D}\delta S}{\mathrm{D}t} = -\delta\left(\frac{\mathcal{L}(\rho, T)}{T}\right). \tag{1.6}$$

Hereafter, the subscript "0" denotes the value in the unperturbed state, and δQ denotes the perturbed variable of a physical variable Q. Since we consider the gas in thermal equilibrium, or $\mathcal{L}(\rho_0, T_0) = 0$, equation (1.6) becomes

$$\frac{\mathrm{D}\delta S}{\mathrm{D}t} = -\frac{1}{T_0}\delta\mathcal{L}(\rho, T). \tag{1.7}$$

We assume that the fluid element evolves leaving a thermodynamic variable, A, fixed. We consider a situation where the entropy of the fluid element is lower than that of the background fluid, or $\delta S < 0$. If $\delta\mathcal{L} < 0$, the fluid element gains entropy and the entropy returns to the background entropy. This indicates thermal stability. If $\delta\mathcal{L} > 0$, the fluid element continues to lose the entropy by the cooling. This indicates thermal instability. One can make the similar discussion for the case with $\delta S > 0$. Therefore, the fluid element is unstable if

$$\left(\frac{\partial\mathcal{L}}{\partial S}\right)_A < 0. \tag{1.8}$$

This criterion is called as the Field criterion.

In the above discussion, we did not specify the detailed evolution of the gas. In other words, A is unknown. To understand the detailed evolution of the gas, we need to consider the continuity equation and the equation of motion. However, we can roughly discuss the evolution of perturbation by considering some limiting behaviors. The time scale of the thermal instability is expected to be $\sim t_{\rm cool}$ that is defined in equation (1.3). The wavenumber of the perturbation is defined as k.

Asymptotic behaviors

For small scale perturbation, $k\lambda_{\rm cool} \gg 1$, the element evolves in pressure equilibrium with its surroundings because the sound wave can travel the scale of the element, $1/k$, many times during the cooling. This mode is called isobaric mode. The isobaric mode is also called condensation mode because the density increases as the temperature decreases. The specific heat at constant pressure is

$$C_p = \left(\frac{\partial H}{\partial T}\right)_P, \tag{1.9}$$

where H is the enthalpy. Using the first law of thermodynamics and equation (1.9), one can get

$$\left(\frac{\partial S}{\partial T}\right)_P = \frac{C_p}{T}. \tag{1.10}$$

Using equations (1.10) and (1.8), the Field criterion for the isobaric mode becomes

$$\left(\frac{\partial \mathcal{L}}{\partial T}\right)_P = \left(\frac{\partial \mathcal{L}}{\partial T}\right)_\rho - \frac{\rho_0}{T_0}\left(\frac{\partial \mathcal{L}}{\partial \rho}\right)_T < 0, \tag{1.11}$$

where the equation of state, $P \propto \rho T$ is used.

For large scale perturbation, $k\lambda_{\rm cool} \ll 1$, the density remains constant because the sound wave cannot travel the scale of the element within the cooling time. This mode is called isochoric mode. The specific heat at constant volume is

$$C_V = \left(\frac{\partial U}{\partial T}\right)_\rho, \tag{1.12}$$

where U is the internal energy. Using the first law of thermodynamics and equation (1.12), one can get

$$\left(\frac{\partial S}{\partial T}\right)_\rho = \frac{C_V}{T}. \tag{1.13}$$

Using equations (1.13) and (1.8), the Field criterion for the isochoric mode becomes

$$\left(\frac{\partial \mathcal{L}}{\partial T}\right)_\rho < 0. \tag{1.14}$$

The Effect of Heat Conduction

For small scale perturbations, the heat conduction is expected to stabilize thermal instability (Field, 1965). Therefore, there is a critical wavenumber, $k_{\rm crit}$, such that perturbations with larger wavenumbers are stabilized by the heat conduction. We evaluate $k_{\rm crit}$ using an order estimation. Using the characteristic time scale of the heat conduction, $t_{\rm diff}$, the diffusion equation is given by

$$\frac{1}{t_{\rm diff}}\left(\frac{P_0}{\gamma-1}\right) \sim k^2 K(T_0)T_0, \tag{1.15}$$

where K is the heat conduction coefficient. From equation (1.15), the diffusion timescale is given by

$$t_{\rm diff} \simeq \frac{P_0}{(\gamma-1)K(T_0)T_0}k^{-2}. \tag{1.16}$$

From equation (1.16), one can see that the diffusion timescale is small for large wavenumber. If $t_{\rm diff} < t_{\rm cool}$, the heat conduction is expected to stabilize thermal instability. Therefore, $k_{\rm crit}$ can be derived on the condition $t_{\rm diff} \sim t_{\rm cool}$ as

$$k_{\rm crit} \simeq \sqrt{\frac{k_{\rm K}}{\lambda_{\rm cool}}}, \quad \text{where} \quad k_{\rm K} \equiv \frac{P_0 c_0}{(\gamma-1)KT_0}. \tag{1.17}$$

Field (1965) derived similar critical wavenumber to equation (1.17). The wavelength, $1/k_{\rm crit}$, is referred to the Field length,

$$\lambda_{\rm F} = \sqrt{\frac{KT}{\rho\Lambda}}. \tag{1.18}$$

Perturbations for $\lambda_{\rm F} < \lambda < \lambda_{\rm cool}$ and $\lambda > \lambda_{\rm cool}$ grow in the isobaric and isochoric modes, respectively.

The Dispersion Relation

Field (1965) investigated stability of spatially uniform and static gas, and derived a dispersion relation. Detailed derivation of the dispersion relation is shown in Appendix A. From the linear analysis, the growth rates of the isobaric and isochoric modes are given by

$$\omega_{\rm isob} = -\frac{1}{t_{\rm cool}}\frac{T_0}{\gamma\Lambda_0}\left(\frac{\partial\mathcal{L}}{\partial T}\right)_P \tag{1.19}$$

and

$$\omega_{\rm isoc} = -\frac{1}{t_{\rm cool}}\frac{T_0}{\Lambda_0}\left(\frac{\partial\mathcal{L}}{\partial T}\right)_\rho, \tag{1.20}$$

respectively. From equations (1.19) and (1.20), it is clearly seen that the isobaric and isochoric criterions (1.11) and (1.14) are also valid in the detailed linear analysis. Using the power-law net cooling rate (equation (1.2)), $\omega_{\rm isob}$ and $\omega_{\rm isoc}$ become

$$\omega_{\rm isob} = \frac{1-\alpha}{\gamma t_{\rm cool}} \quad \text{and} \quad \omega_{\rm isoc} = \frac{-\alpha}{t_{\rm cool}}, \tag{1.21}$$

respectively. Therefore, the isobaric and isochoric criterions are given by

$$\begin{cases} \alpha < 1 & \text{for the isobaric mode} \\ \alpha < 0 & \text{for the isochoric mode} \end{cases} . \tag{1.22}$$

Figures 1.6a and 1.6b show the dispersion relations of real part of ω for $\alpha = 0.5$ and -0.5, respectively, where $k_{\rm K}\lambda_{\rm cool} = 10$. The solid and dashed lines indicate results with and without the heat conduction, respectively. From figures 1.6a and 1.6b, it is clearly seen that the heat conduction stabilizes thermal instability for large wavenumber. From equation (1.17) and $k_{\rm K}\lambda_{\rm cool} = 10$, the critical wavenumber is $k_{\rm crit}\lambda_{\rm cool} \sim \sqrt{10}$. Figures 1.6a and 1.6b show that thermal instability is completely stabilized around $k_{\rm crit}\lambda_{\rm cool} \sim \sqrt{10}$. The behaviors for small wavenumber of figures 1.6a and 1.6b are different. Since the isochoric mode is stable for $\alpha = 0.5$ from the Field criterion (equation (1.22)), the growth rate approaches zero for lower wavenumber in figure 1.6a. This reduction of the growth rate comes from finiteness of the sound speed. On the other hand, since the isochoric mode is unstable for $\alpha = -0.5$, the growth rate has the finite value of $\omega_{\rm isoc}$ for $k \sim 0$ in figure 1.6b.

1.4.2 Thermally Unstable Phase

Figure 1.5 shows there are three phases in thermal equilibrium state. However, one of them is thermally unstable. The segment of the dashed line of the thermal equilibrium curve in figure 1.7 shows the thermally unstable range where Field criterion for the isobaric mode (see equation 1.11) is satisfied. The isochoric mode is stable for 10^{-1} cm^{-3} $< n <$ 10^{3} cm^{-3}. Therefore, cold and warm phases are thermally stable, and the phase between them is thermally unstable in the isobaric mode. The cold phase ($n \sim 30$ cm^{-3}, $T \sim 100$ K) is identified with the cold neutral medium that is detected as narrow absorption 21-cm lines. On the other hand, the warm phase ($n \sim 0.3$ cm^{-3} and $T \sim 8000$ K) corresponds to the warm neutral medium that is detected as broad emission 21-cm lines. Therefore, the two-phase model can naturally explain the cold and warm components of the ISM. However, the two-phase model cannot address how these structures form.

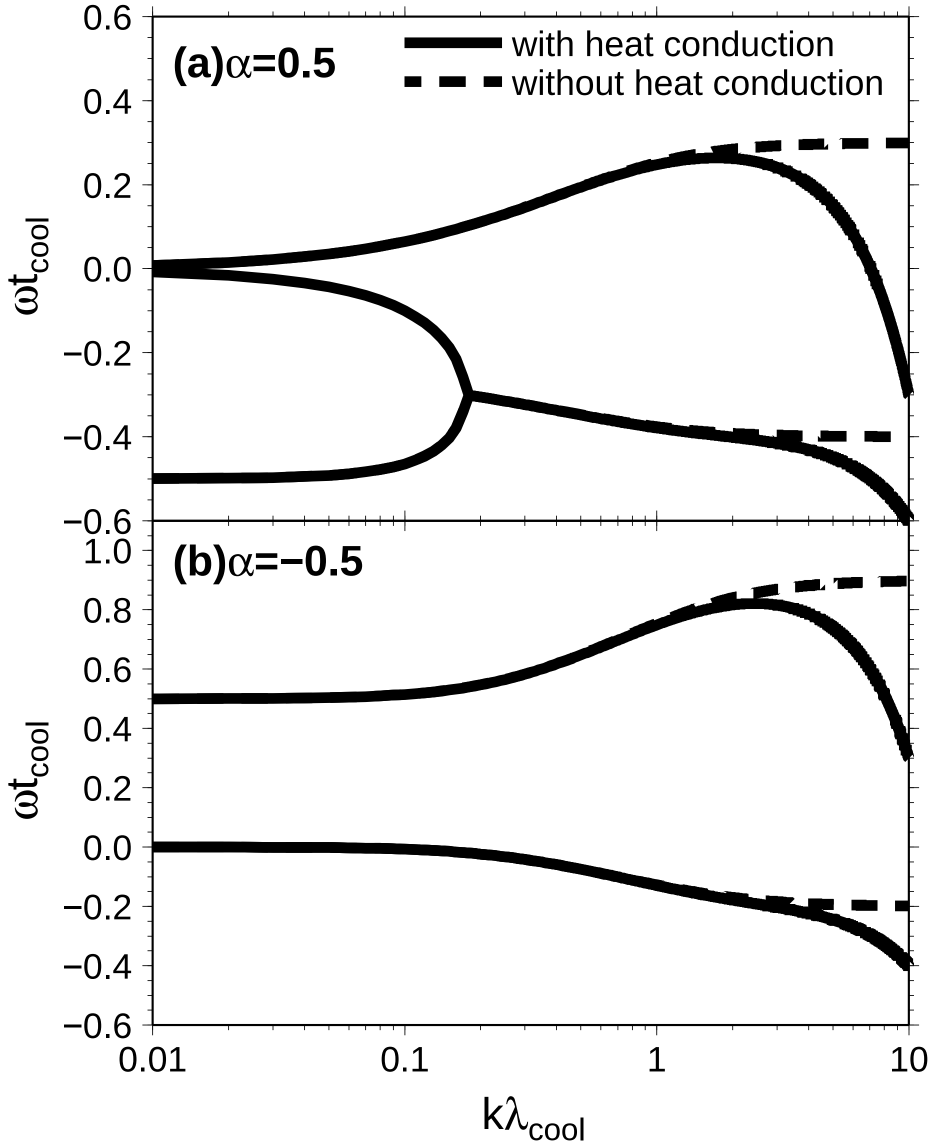

Figure 1.6: The dispersion relation for α =0.5(a) and -0.5(b), where $k_{\mathrm{K}}\lambda_{\mathrm{cool}} = 0.01$. The solid and dashed lines indicate results with and without the heat conduction, respectively. The isobaric mode is unstable for both cases of $\alpha = 0.5$ and -0.5 for $k\lambda_{\mathrm{cool}} \gg 1$. On the other hand, the isochoric mode is stable for $\alpha = 0.5$ and is unstable for $\alpha = -0.5$ for $k\lambda_{\mathrm{cool}} \ll 1$.

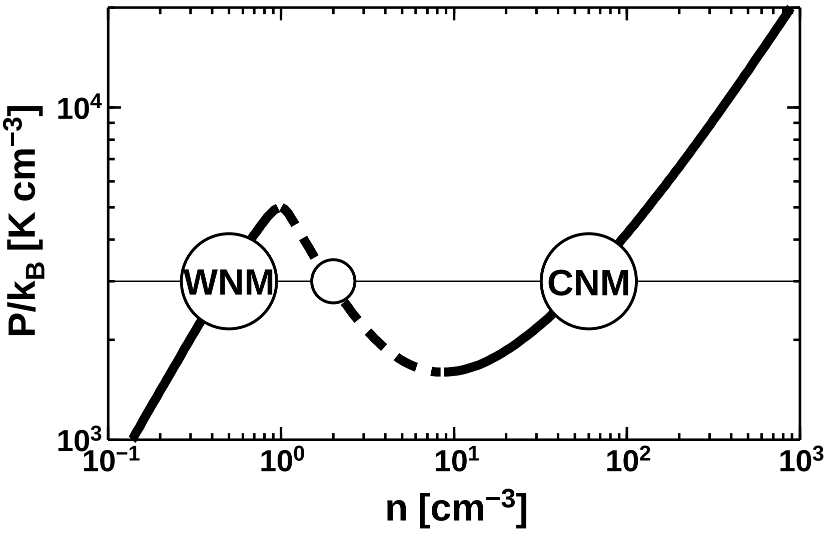

Figure 1.7: Phase diagram of thermal properties of ISM in (n, P) plane. The thick line indicates thermal equilibrium curve where the gas is thermally stable. The segment of the dashed line indicates the thermally unstable range according to Field criterion for the isobaric mode is satisfied.

1.5 Dynamical Three-Phase Model

Observations of soft X-ray background and O VI absorption lines have revealed that the significant volume of the Galaxy is occupied by the HIM (see section 1.2.2). Cox and Smith (1974) showed that the formation and maintenance of the HIM require a large energy input, such as supernovae. Therefore, the ISM is not quiescent as is assumed in the two-phase model but is disturbed by supernova shocks. Let us estimate how often supernova shocks sweep up the ISM. A supernova remnant expands until the internal pressure becomes lower than the pressure of the ambient ISM with $n = 0.1$ cm^{-3} and $T = 10^4$ K. The supernova remnant reaches the maximum radius, $R_{\rm max} = 10^{2.1}$ pc at a time, $t_{\rm max} = 10^{6.3}$yr, considering typical supernova energy of 10^{51} erg. The total volume $SR^3_{\rm max}t_{\rm max}$ that all supernova remnants occupy at $t_{\rm max}$ exceed the volume of the Galaxy, where $S = 10^{-2}$ yr^{-1} is the supernova rate in the Galaxy. This means that the supernova remnants overlap before they are dissipated, and the ISM is swept up by supernova shocks per $\sim 10^6$ yr. Therefore, this estimation shows that supernova shocks play important role in the ISM. McKee and Ostriker (1977) proposed a model of the ISM where physical properties and structures of the ISM are regulated by supernova shocks. In their model, the ISM consists of three phases (hot, warm and cold phases). The schematic picture of the three-phase model is shown in figure 1.8 that was presented in McKee and Ostriker (1977). The crosshatched and dotted regions indicate the CNM and WNM, respectively. The intercloud region is assumed to be occupied by HIM. A supernova blast wave is expanding into the region from the upper right. The inside of shock wave is filled with very hot gas that is subject to radiative cooling via Bremsstrhalung and metal lines. The HI clouds inside the hot bubble evaporate due to heat conduction (see figure 1.8). On the other hand, compressed gas collapses into dense cold shell via radiative cooling. In the three-phase model, the evaporation of the HI clouds balances the formation of the HI clouds in the swept-up shell. Moreover, the energy input by supernova shocks balances the radiative cooling. The mass balance and energy balance provide the density and the temperature of the HIM with $(n, T) = (10^{-2.5}\ \mathrm{cm}^{-3},\ 10^{5.7}\ \mathrm{K})$ that is consistent with observations.

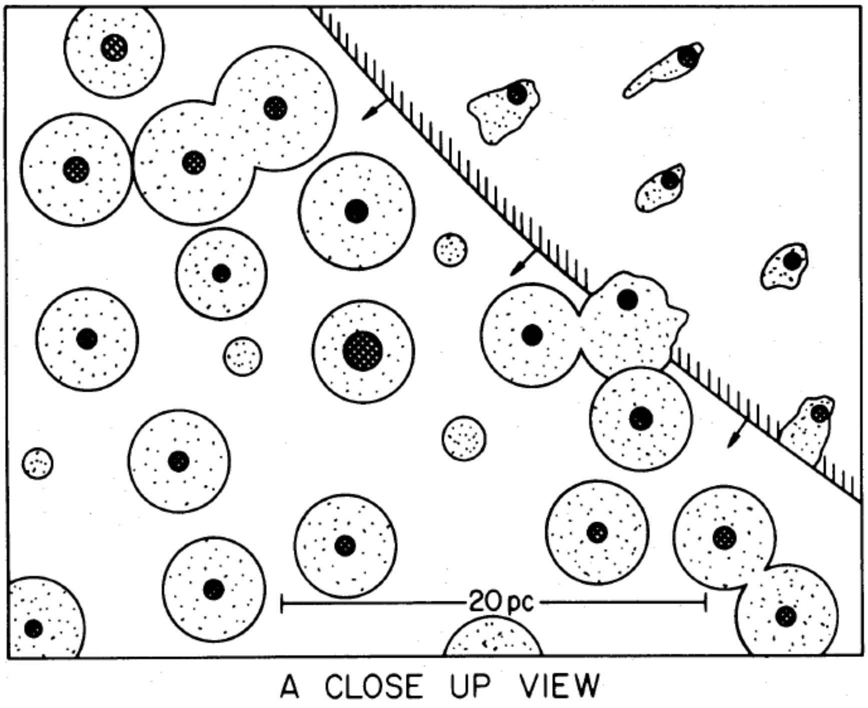

Figure 1.8: Schematic plot of the three-phase model. A cross section of a representative region 30pc×40pc in extent is shown. A supernova blast wave is expanding into the region from the upper right. The crosshatched and dotted regions indicate the CNM and WNM, respectively. This figure was presented in McKee and Ostriker (1977).

However, the three-phase model does not address the detailed process of the HI cloud formation in the postshock region. It does not contain molecular clouds that are important for considering processes leading to formation of stars. Koyama and Inutsuka (2000) investigated the shock propagation into a WNM and a CNM by one-dimensional calculations with the detailed chemical reaction and cooling and heating processes, They showed that a large amount of hydrogen molecules is generated inside a geometrically thin and dense layer that is produced by radiative cooling in shock-compressed region. Hennebelle and Pèrault (1999) investigated a converging flow of a WNM gas as other mechanism producing shock waves by using one-dimensional calculation. As mentioned in section 1.2.4, since WNM has transonic or weakly supersonic turbulence, the converging flow is possible mechanism. They derived a condition where thermal instability occurs, and thin and dense layer forms. They showed that the shock-induced thermal instability is effective in the converging flow of the WNM.

In the postshock region, results of linear analysis of Field (1965) cannot be used because the gas is far from thermal equilibrium.

1.5.1 Thermal Instability of the Gas in Thermal Nonequilibrium State

Balbus (1986) generalized the Field criterion for $\mathcal{L}_0 \neq 0$ by a local argument. Unlike the thermal equilibrium case, the background gas evolves with time. Here, we consider the cooling dominated case, $\mathcal{L} > 0$. The characteristic timescale of the evolution of the gas is given by the cooling time $\sim t_{\rm cool} = C_V T/\mathcal{L}$ (see equation (1.3)). Therefore equation (1.6) can be written as

$$\frac{\mathrm{D}\delta S}{\mathrm{D}t} = C_V \frac{\delta t_{\rm cool}}{t_{\rm cool}^2}. \tag{1.23}$$

We consider a situation where the entropy of the fluid element is lower than that of the background fluid, or $\delta S < 0$. If $\delta t_{\rm cool} > 0$, the fluid element cools slower than the background gas. Therefore, the entropy of the fluid element tends to return to the background entropy. This indicates thermal stability. If $\delta t_{\rm cool} < 0$, the fluid element cools more rapidly than the background gas. Therefore, the entropy of the fluid element continues to evolve away from the background entropy. This indicates thermal instability. Therefore, the gas is unstable if

$$\left(\frac{\partial t_{\rm cool}}{\partial S}\right)_A > 0, \quad \Longrightarrow \quad \left[\frac{\partial}{\partial S}\left(\frac{\mathcal{L}}{T}\right)\right]_A < 0, \tag{1.24}$$

where we also assume that the fluid element evolves leaving some thermodynamic variable, A, fixed. The criterion (1.24) was derived by Balbus (1986). Equation (1.24) can be written as

$$\left(\frac{\partial \mathcal{L}}{\partial S}\right)_A < \frac{\mathcal{L}_0}{T_0}\left(\frac{\partial T}{\partial S}\right)_A . \tag{1.25}$$

Balbus criterion gives weaker constraint on the cooling rate than Field criterion (1.8) because the right-hand side of equation (1.25) is positive in normal gases.

The Balbus criterion for the isobaric mode is

$$\left[\frac{\partial}{\partial T}\left(\frac{\mathcal{L}}{T}\right)\right]_P < 0 \Longrightarrow \left(\frac{\partial \ln \mathcal{L}}{\partial \ln T}\right)_\rho - \left(\frac{\partial \ln \mathcal{L}}{\partial \ln \rho}\right)_T < 1. \tag{1.26}$$

The Balbus criterion for the isochoric mode is

$$\left[\frac{\partial}{\partial T}\left(\frac{\mathcal{L}}{T}\right)\right]_\rho < 0 \Longrightarrow \left(\frac{\partial \ln \mathcal{L}}{\partial \ln T}\right)_\rho < 1. \tag{1.27}$$

Using the power-law net cooling rate (1.2), the criterion becomes

$$\begin{cases} \alpha < 2 & \text{for the isobaric mode} \\ \alpha < 1 & \text{for the isochoric mode.} \end{cases} \tag{1.28}$$

The Dispersion Relation

In the gas in thermal nonequilibrium, it is difficult to select unperturbed states because they have time dependence. Therefore, in previous studies, unperturbed state is assumed to be spatially uniform. Initially static and uniform gas cools leaving the density constant because the velocity is zero, or isochorically. Schwarz, McCray, and Stein (1972) investigated stability analysis of an isochorically cooling uniform gas by numerically solving perturbation equations. They found that perturbation grows in the isobaric mode for $\lambda_{\rm F} < \lambda < \lambda_{\rm cool}$ and that the criterion of the isobaric mode is given by equation (1.26). For the large wavelength limit, $\lambda > \lambda_{\rm cool}$, they found that the gas cools ahead of pressure equilibrium. This indicates the isochoric mode. Burkert and Lin (2000) obtained similar results by considering a simple power-law cooling function. Koyama and Inutsuka (2000) investigated stability analysis of isobarically condensing uniform gas. They introduced a contracting coordinate to express isobarically condensing background. They also found that perturbations grow in the isobaric and isochoric mode for $\lambda_{\rm F} < \lambda < \lambda_{\rm cool}$ and $\lambda_{\rm cool} < \lambda$, respectively. Therefore, from previous studies, dispersion relation of a spatially uniform gas is expected to be similar to that of the gas in thermal equilibrium.

1.5.2 Thermal Instability in the Interstellar Medium

This thesis focus on the low temperature range of $T < 10^4$ K. The thermally unstable region is shown by gray colors in figure 1.9. The light and dark gray regions indicate unstable regions in the isobaric and isochoric modes, respectively. Figure 1.9 shows that thermal instability occurs in the cooling dominated gas that is located above the thermal equilibrium curve in the temperature range between CNM and WNM.

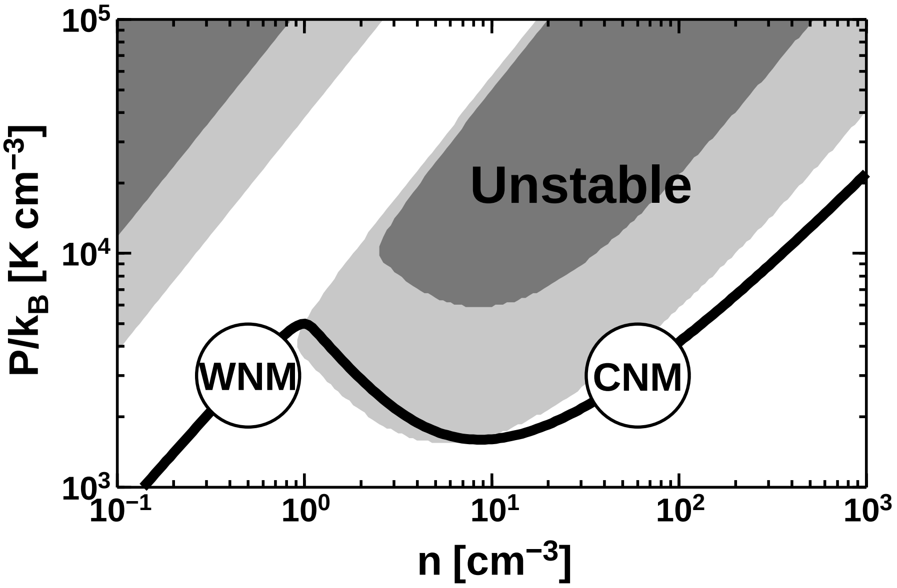

Figure 1.9: Phase diagram of thermal properties of ISM in (n, P) plane. The thick line indicates thermal equilibrium curve. The light and dark gray regions indicate unstable regions in the isobaric and isochoric modes, respectively.

1.6 Nonlinear Evolution of the Shock-induced Formation of Interstellar Clouds in One-dimensional Model

The diffuse gases are frequently disturbed by external sources, such as supernovae shock waves (McKee and Ostriker, 1977). Moreover, since the diffuse gases have transonic turbulence that velocity dispersion is about 10 km s^{-1} (Heiles and Troland, 2003), the diffuse gas can be compressed by the turbulent motion (Hennebelle and Pèrault, 1999). These compression processes can put the diffuse gas into thermally unstable state, and dynamical condensations take place. In this section, we investigate one-dimensional evolution of converging flow of diffuse gases.

1.6.1 Basic Equations

One-dimensional basic equations for the radiative gas under plane-parallel geometry are the continuity equation,

$$\frac{\partial \rho}{\partial t} + \frac{\partial}{\partial x}(\rho v) = 0 \tag{1.29}$$

the equation of motion,

$$\frac{\mathrm{D}\vec{v}}{\mathrm{D}t} + \frac{1}{\rho}\frac{\partial P}{\partial x} = 0, \tag{1.30}$$

the energy equation,

$$\frac{1}{\gamma - 1}\left(\frac{\mathrm{D}P}{\mathrm{D}t} - \gamma\frac{P}{\rho}\frac{\mathrm{D}\rho}{\mathrm{D}t}\right) = -\rho\mathcal{L}(\rho, T) - \frac{\partial}{\partial x}\left(K\frac{\partial T}{\partial x}\right), \tag{1.31}$$

and the equation of state,

$$P = \frac{k_{\mathrm{B}}}{\mu m_{\mathrm{H}}}\rho T, \tag{1.32}$$

where we adopt the heat conduction coefficient for neutral gas, $K = 2.5 \times 10^3\, T^{1/2}$ erg cm^{-1} K^{-1} s^{-1} (Parker, 1953). The net cooling rate is fitted by Koyama and Inutsuka (2002) as

$$\rho\mathcal{L} = n(-\Gamma + n\Lambda)\ \ \mathrm{erg\ cm^{-3}\ s^{-1}}, \tag{1.33}$$

where

$$\Gamma = 2 \times 10^{-26}\ \mathrm{erg\ s^{-1}}, \tag{1.34}$$

$$\frac{\Lambda}{\Gamma} = 1.0 \times 10^7 \exp\left(-\frac{118400}{T + 1000}\right) + 1.4 \times 10^{-2}\sqrt{T}\exp\left(-\frac{92}{T}\right), \tag{1.35}$$

where n is the number density of the gas. The heating rate in equation (1.34) is based on the photoelectric heating from small dusts and PAHs by typical far-ultraviolet radiation in the interstellar space in the Galaxy ($G_0 = 1.7$). The first and second terms of the cooling rate in equation (1.35) correspond to the collisional excitations of the hydrogen Lyα line and the fine-structure line of CII (158μm), respectively.

1.6.2 Initial Conditions and Numerical Methods

We consider a head-on collision between two identical gas flows in thermal equilibrium with the density, $\rho_{\rm WNM} = 0.57 m_{\rm H}$ cm^{-3} and pressure, $P_{\rm WNM} = 3.5 \times 10^3 k_{\rm B}$ dyne cm^{-2}. The two clouds collide along the x-axis at $t = 0$ and $x = 0$ with velocity of 20 km s^{-1}, i.e., the corresponding mach number is 2.17. We add the following density fluctuation into the initial condition,

$$\rho(t=0,x) = \rho_{\rm WNM} \left\{ 1 + \frac{A}{i_{\rm max}} \sum_{i=0}^{i_{\rm max}} \sin\left(\frac{2\pi x}{L_x} + \theta_i \right) \right\}, \tag{1.36}$$

where $i_{\rm max} = 10$, $A = 0.8$, the phase, θ_i, is given by random number between 0 and 2π, and $L_x = 50$ pc is the calculation box size of the x-direction.

We use the one-dimensional second-order Lagrangian Godunov scheme (van Leer, 1997).

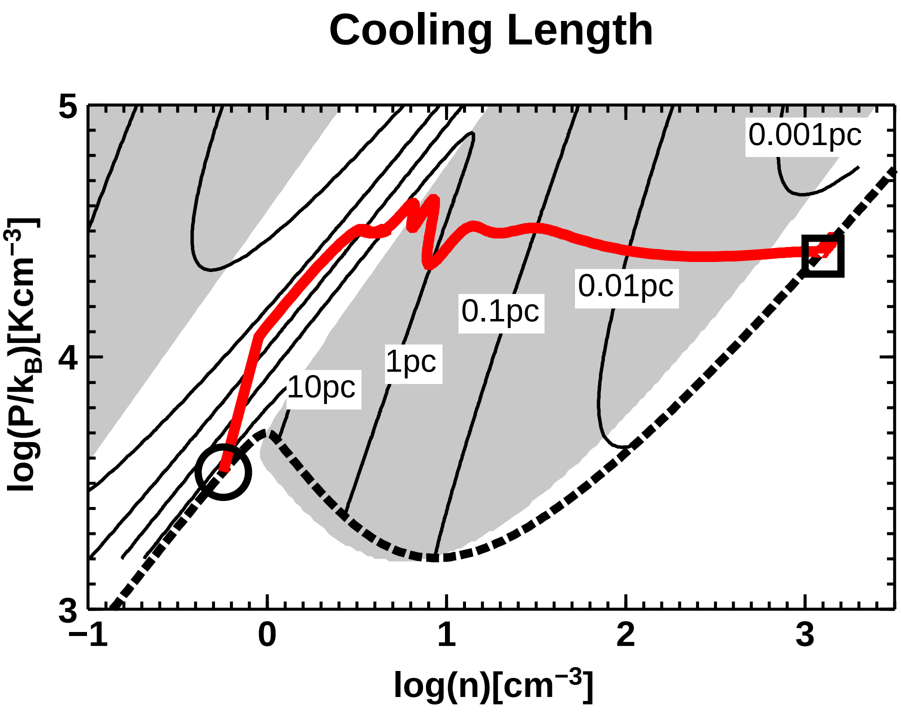

Figure 1.10: Evolutionary track of the highest density portion in the (n, P) plane that is shown the thick solid line. The preshock gas is shown by the open circle. The dashed line corresponds to the thermal equilibrium curve. The open box corresponds to the generated cold clouds. The contour map indicates the cooling length. The gray region shows the thermally unstable region where the Balbus criterion for the isobaric mode (1.26) is satisfied.

1.6.3 Results

The colliding flow produces the shock-compressed region confined by two shock waves that propagate outward. Figure 1.10 shows the evolutionary track of the highest density portion in the (n, P) plane by the red solid line. The thermal equilibrium curve is plotted by the dashed line. The open circle denotes the preshock gas. The shock wave puts the preshock gas above the thermal equilibrium curve as is shown in figure 1.10. Since the cooling rate dominates the heating rate, the shocked gas cools until it reaches a thermal equilibrium state shown by the open box. During the cooling, the pressure of the gas remains almost constant of which value is roughly determined by the ram pressure of the converging flow. The gray region in figure 1.10 is unstable region in the isobaric mode where the Balbus criterions (1.26) is satisfied. The gas at the highest density passes the unstable region during $0.2\,\mathrm{Myr} \lesssim t \lesssim 0.95\,\mathrm{Myr}$.

Figure 1.11 shows snapshots of the number density, pressure, temperature, and velocity at $t = 0.60$, 0.70, 0.80, and 0.90 Myr. The preshock gases are heated to the temperature of $> 10^4$ K by the shock compression. Thereafter, the gases rapidly lose their internal energy through the radiative cooling. This is found in figure 1.11 as the spiky features in the temperature profiles. Figure 1.11 shows that the rapid condensation breaks out around $x \sim 0.5$ pc by thermal instability keeping the pressure constant. This is the isobaric mode that is the most unstable mode (see section 1.5.1). The detailed evolutions of the density and temperature during the condensation is shown in figure 1.12 at $t = 0.80$, 0.90, 0.95, 0.96, 0.98, and 1.05 Myr. The abscissa axes of figure 1.12 are the distances from the position at the density peak, $x_{\max}(t)$ at each instant of time. Figure 1.12 shows that the gas around $x_{\max}$ condenses in a runaway fashion, leaving the surrounding gas behind. The more the gas condenses, the shorter the scale of the condensing layer becomes. At $t = 0.98$ Myr, the gas reaches the thermal equilibrium shown by the open box in figure 1.10. The scale of the cold cloud layer is as small as 5×10^{-4} pc that is smaller than the cooling length shown by contour in figure 1.10. This is consistent with the linear theory in section 1.5.1. The density of the cold cloud is as large as that of the molecular cloud $\sim 10^3$ cm^{-3} because of the high pressure. After that, the size of the cold gas layer increases by accretion of the surrounding gases as shown figure 1.12 at $t = 1.05$ Myr. Koyama and Inutsuka (2000) shows molecular hydrogen is generated in the cold gas layer during the phase of gaining weight by one-dimensional calculation with chemical reactions. Therefore, the cold clouds can be seed of molecular clouds.

Note that that time evolution of the gas appears to be self-similar in figures 1.12. The term of “self-similar” means that the profile of the density and temperature corresponding to different time can be made the same by either expanding and contracting the scales of the density, temperature, and $|x - x_{\rm max}|$ (Landau and Lifshitz, 1959; Zel’dovich and Raizer, 1967). The self-similarity of gas evolution is also seen in gravitational collapses of gas spheres (Hunter, 1977; Larson, 1969; Penston, 1969; Shu, 1977).

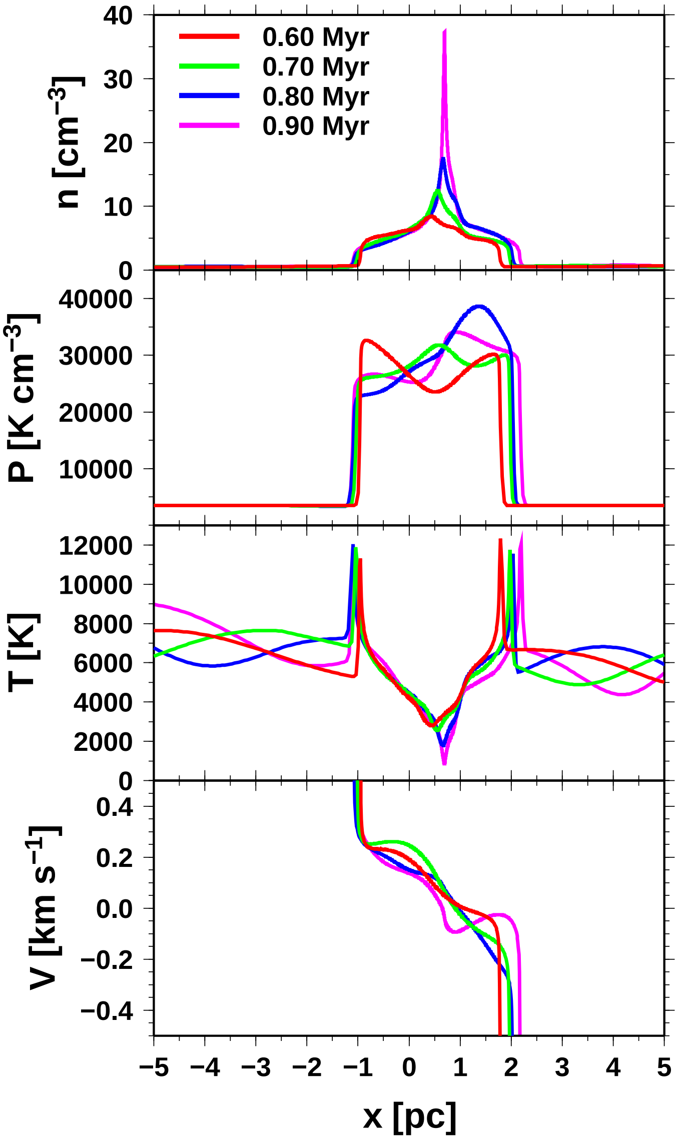

Figure 1.11: The evolutionary sequences for the number density, pressure, temperature, and velocity at $t = 0.60$, 0.70, 0.80, and 0.90 Myr.

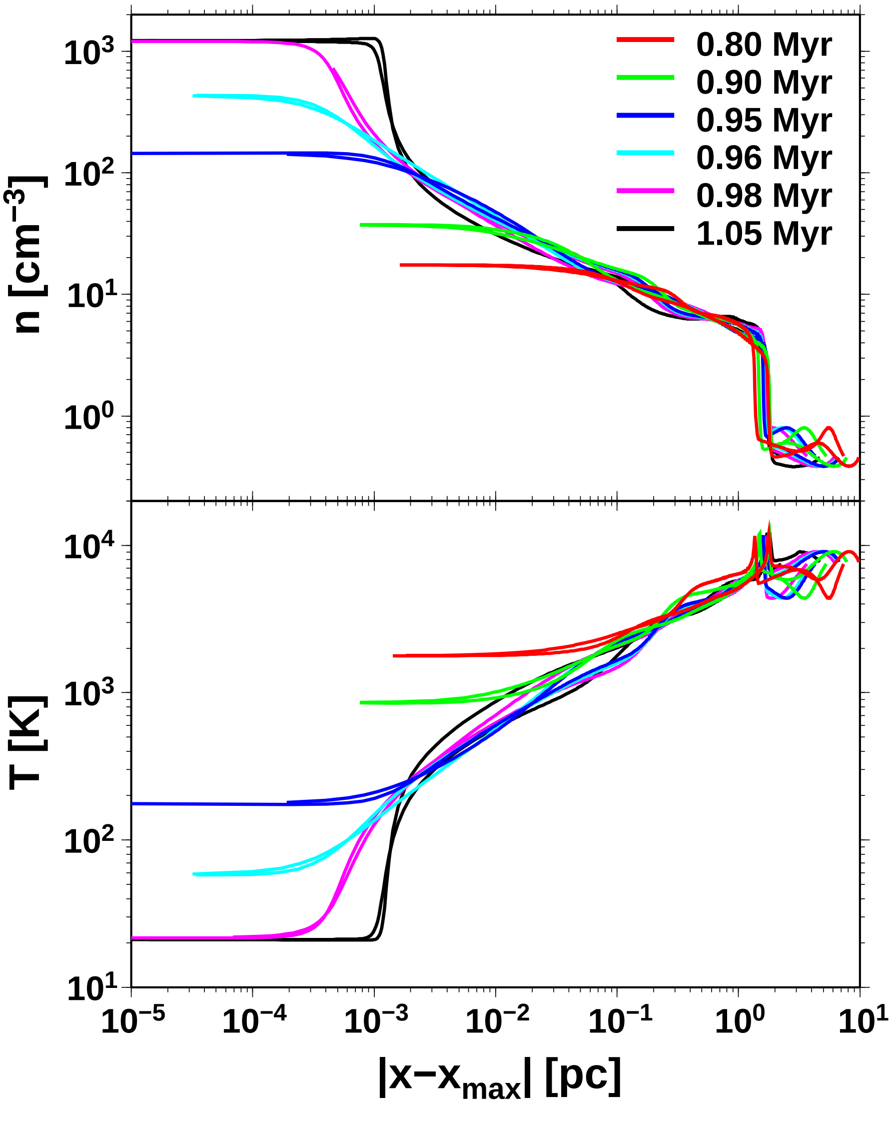

Figure 1.12: The evolutionary sequences for the number density and temperature $t = 0.80$, 0.90, 0.95, 0.96, 0.98, and 1.05 Myr. The abscissa axes indicate $|x - x_{\rm max}|$, where $x_{\rm max}$ is the position at the maximum density.

1.7 Multi-dimensional Numerical Simulations of the Formation of Interstellar Clouds

In the one-dimensional simulation in section 1.7, the runaway condensing layer is generated in shock-compressed region. The layer stops condensing when it reaches thermal equilibrium state and its size increases by accretion of the surrounding gases. Recently, many authors have investigated multi-dimensional evolutions in shock-compressed regions and have shown that the gas evolution is very different from results by one-dimensional calculation.

Koyama (2000); Koyama and Inutsuka (2002) investigated the shock propagation into WNM and development of the cold layer in the shocked region by using two-dimensional simulation. They found that the runaway cooling layer break up into several cold clouds whose density is comparable to that of molecular clouds. These cold clouds have velocity dispersion that is a fraction of the sound speed of WNM. This velocity dispersion is supersonic with respect to the sound speed of cold clouds. They suggested that the origin of observational “supersonic turbulence” of interstellar clouds is the motion of those cold clouds. Analogous processes have been studied by many authors for a colliding flow of the WNM (Audit and Hennebelle, 2005; Heitsch et al., 2005, 2006; Hennebelle and Audit, 2007; Vàzquez-Semadeni et al., 2006). In these simulations, the condensed cold clouds also have supersonic velocity dispersion the shock-compressed region.

As shown in section 1.7, the density of these cold clouds is comparable with that of molecular clouds because of the high ram pressure. However, the infant cold clouds are still too less massive to be gravitationally bound. They gain their weight by accretion of the surrounding unstable gas and by coalescence between the cold clouds. As their mass increases, the self-gravity becomes important, and molecular hydrogen is generated. Finally molecular clouds form. Including self-gravity, Heitsch and Hartmann (2008); Vàzquez-Semadeni et al. (2007) investigate evolution of these cold clouds in shock compressed region by three-dimensional simulations that do not have sufficient resolutions to see the detailed clumpy structures formed by thermal instability. They showed that rapid local gravitational collapses of the massive cold clouds break out before the global self-gravity dominates the dynamics completely (also see Heitsch et al., 2008). Hennebelle, Audit, and Miville-Deschênes (2007) showed that cold clouds in two-dimensional simulations can reasonably reproduce various observational properties of molecular clouds, such as the mass spectrum, Larson's law (see section 1.2.4), and so on although the cold clouds are less massive and consist of atomic hydrogen yet. They suggested that the fundamental properties of molecular clouds could be determined in very early phase. Therefore, the properties of the cold clouds formed by thermal instability important as seed of molecular clouds.

Recently, the effect of the magnetic field on the thermal instability has been investigated by Heitsch et al. (2009); Hennebelle and Passot (2006); Hennebelle and Pèrault (2000); Hennebelle et al. (2008); Inoue and Inutsuka (2008, 2009); Inoue et al. (2007).

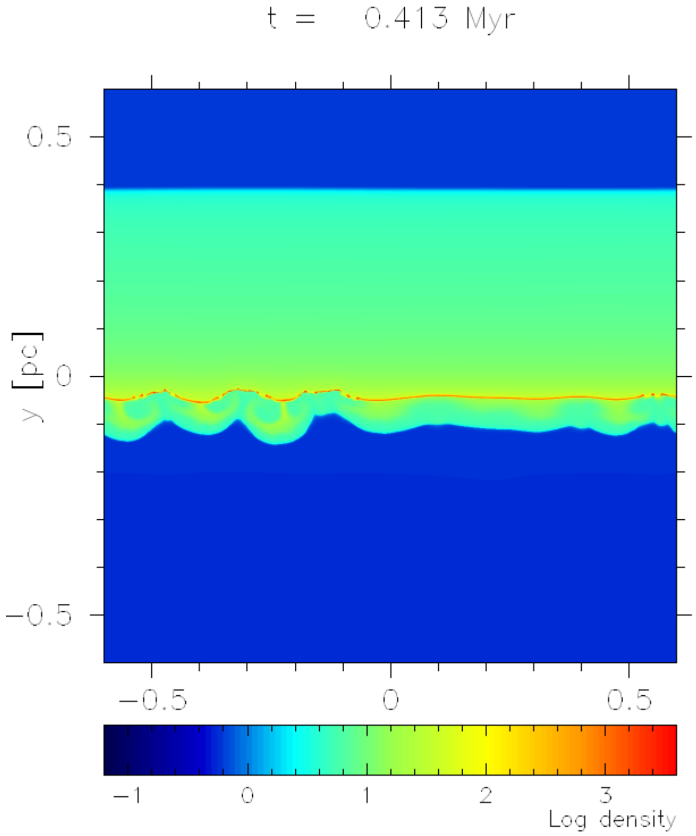

Figure 1.13: Density color maps of the shock-compressed region for t = 0.413 and 1.808 Myr. Figure was presented in Koyama (2000).

1.8 Purpose of This Thesis

In this thesis, we focus on the size distribution of infant cold clouds formed by thermal instability. Koyama (2000) investigated the shock propagation into WNM and development of the cold layer in the shocked region by using two-dimensional simulation. Figure 1.13 shows the density color map of the shock-compressed region for $t = 0.413$ Myr when the cooling layer just reaches thermal equilibrium state. The generated cold clouds are shown by the red color. The density discontinuities at $y \sim 0.4$ and -0.1 pc correspond to the shock front and the contact discontinuity that divides shock-compressed gas with a hot gas. The linear analysis of the gas in thermal nonequilibrium state (see section 1.5.1) predicts that the smaller scale is more unstable (Koyama and Inutsuka, 2000). However, figure 1.13 shows that the generated cold clouds have various shapes, such as a sphere and a filament. The sizes of these filamentary cold clouds are larger than the cooling length (see figure 1.10). The linear analysis by Koyama and Inutsuka (2000) is based on a isobarically condensing gas distributed uniformly. Moreover, Koyama and Inutsuka (2000) neglected the time evolution of the unperturbed state. However, the cooling layer is far from spatially uniform as shown in section 1.7. Moreover, it is nontrivial whether the fluctuation on the condensing layers grows faster than collapse of the unperturbed state. If the unperturbed state reaches a thermal equilibrium before perturbations grow sufficiently, the cooling layer does not split into cold fragments. Therefore, a linear analysis taking account of the spatial distribution and time evolution of the unperturbed state is required to understand evolution of condensing layers more deeply. Understanding evolution of condensing layers relates with the size and aspect-ratio distributions of the cold clouds that are important for understanding turbulent structures of shocked regions.

To investigate evolution of runaway cooling layers, in this thesis, we adopt the following three-step approach.

1. The time evolution of the condensing layer has a self-similarity from figure 1.12 in section 1.7. Therefore, we propose new self-similar solutions describing nonlinear hydrodynamical evolution of runaway cooling gas layers. The obtained new self-similar solutions describe the results of the one-dimensional calculation in section 1.7 very well as we will show later. This shows that the self-similar solutions are expected to be a good nonlinear one-dimensional model of a runaway cooling layer.

2. To investigate multi-dimensional evolution of cooling layers, we perform linear analysis of the self-similar solutions against fluctuations perpendicular, as well as parallel, to the direction of the condensation. The time evolution of the unperturbed cooling layer

is taken into account exactly.

3. We use two-dimensional numerical simulation to check the results of the linear analysis and to investigate two-dimensional nonlinear evolution of cooling layers.

1.9 Content of This Thesis

In chapter 2, we seek self-similar solutions describing nonlinear evolution of cooling layers. To investigate fragmentation process of cooling layers, we perform linear analysis of obtained self-similar solutions in chapter 3. In chapter 4, we present two-dimensional simulation of fragmentation of cooling layers, and investigate nonlinear evolution of the cooling layer. Summary and future prospects are presented in chapter 5

Chapter 2

Self-Similar Solution

From figure 1.12, the cooling layer evolves in a self-similar manner in one-dimensional calculation. Therefore, in this chapter, we propose new self-similar solutions as a one-dimensional model of nonlinear evolution of cooling layers.

This chapter is mainly based on our paper, Iwasaki and Tsuribe (2008).

2.1 Formulation

2.1.1 The Net Cooling Rate

Since we consider thermal instability in a shock-compressed region where the cooling rate dominates the heating rate, the heating rate is neglected explicitly in equation (1.2) as

$$\mathcal{L}(\rho, c_{\mathrm{s}}) = \Lambda_0 \rho c_{\mathrm{s}}^{2\alpha} \ \ \mathrm{erg\ g^{-1}\ s^{-1}}, \ \ c_{\mathrm{s}} = \sqrt{\gamma \frac{P}{\rho}}, \tag{2.1}$$

where c_{s} indicates sound speed.

2.1.2 Basic Equations

Basic equations for the radiative gas are the continuity equation,

$$\frac{\partial \rho}{\partial t} + \vec{\nabla} \cdot (\rho \vec{v}) = 0, \tag{2.2}$$

the equation of motion,

$$\frac{\mathrm{D}\vec{v}}{\mathrm{D}t} + \frac{1}{\rho}\vec{\nabla} P = 0, \tag{2.3}$$

the energy equation,

$$\frac{2}{\gamma-1}\frac{\mathrm{D}\ln c_{\mathrm{s}}}{\mathrm{D}t}-\frac{\mathrm{D}\ln\rho}{\mathrm{D}t}=-\gamma\Lambda_0\rho c_{\mathrm{s}}^{2(\alpha-1)}, \tag{2.4}$$

and the equation of state,

$$P=\frac{k_{\mathrm{B}}}{\mu m_{\mathrm{H}}}\rho T, \tag{2.5}$$

where $\mathrm{D}/\mathrm{D}t=\partial/\partial t+\vec{v}\cdot\vec{\nabla}$ indicates the Lagrangian time-derivative, and μm_{H} is mean weight per hydrogen nucleus.

2.1.3 Derivation of Self-similar Equations

We take the x-axis as the direction of the condensation driven by cooling and consider time evolution of the gas only in the x-direction. The effect of viscosity and heat conduction is neglected for simplicity. We assume that the density and temperature has a maxinum and a minimum values at $x=0$, respectively. The gas at the central region cools more rapidly than the outer region. During the runaway cooling, the gas in the central region is expected to lose initial memories and to converge to self-similar solutions that we seek.

In order to seek self-similar solutions, we introduce a similarity variable, ξ, and assume that the each physical quantity is given by the following form:

$$x=x_0(t)\xi,\ \ v(x,t)=v_0(t)V(\xi),\ \ c_{\mathrm{s}}(x,t)=v_0(t)X(\xi),$$

$$\rho(x,t)=\rho_0(t)\Omega(\xi),\ \text{ and }\ P(x,t)=P_0(t)\Pi(\xi). \tag{2.6}$$

Substituting equations (2.6) into the basic equations (2.2)-(2.4), one obtains

$$\frac{\dot\rho_0}{\rho_0}\Omega+\left(-\frac{\dot x_0}{x_0}\xi+\frac{v_0}{x_0}V\right)\frac{\mathrm{d}\Omega}{\mathrm{d}\xi}+\Omega\frac{\mathrm{d}V}{\mathrm{d}\xi}=0, \tag{2.7}$$

$$\frac{\dot v_0}{v_0}V+\left(-\frac{\dot x_0}{x_0}\xi+\frac{v_0}{x_0}V\right)\frac{\mathrm{d}V}{\mathrm{d}\xi}+\frac{v_0}{\gamma x_0}\frac{1}{\Omega}\frac{\mathrm{d}\Omega X^2}{\mathrm{d}\xi}=0, \tag{2.8}$$

and

$$\frac{2}{\gamma-1}\frac{\dot v_0}{v_0}-\frac{\dot\rho_0}{\rho_0}+\left(-\frac{\dot x_0}{x_0}\xi+\frac{v_0}{x_0}V\right)\left(\frac{2}{\gamma-1}\frac{\mathrm{d}\ln X}{\mathrm{d}\xi}-\frac{\mathrm{d}\ln\Omega}{\mathrm{d}\xi}\right)=-\gamma\Lambda_0\rho_0 v_0^{2(\alpha-1)}\Omega X^{2(\alpha-1)}. \tag{2.9}$$

To omit time dependence from equations (2.7)-(2.9), the following relations must be satisfied;

$$v_0(t)\propto\dot x_0(t) \tag{2.10}$$

and

$$\frac{v_0(t)}{x_0(t)} \propto \rho_0(t) v_0(t)^{2(\alpha-1)}. \tag{2.11}$$

We assume a power-law dependence of $x_0(t) = a(1-t/t_c)^{1/(1-\omega)}$, where ω is a parameter and t_c is an epoch when the central density becomes infinity. The factor $1 - t/t_c$ decreases with time and becomes zero at the epoch t_c. From equations (2.10) and (2.11), time dependences of $v_0(t)$, $\rho_0(t)$ and $P_0(t)$ are given by

$$v_0(t) \propto (1 - t/t_c)^{\omega/(1-\omega)}, \quad \rho_0(t) \propto (1 - t/t_c)^{\{(3-2\alpha)\omega-1\}/(1-\omega)}, \tag{2.12}$$

and

$$P_0(t) \propto (1 - t/t_c)^{\{(5-2\alpha)\omega-1\}/(1-\omega)}$$

From equation (2.12) and equations (2.7)-(2.9), we find the following definition;

$$x_0(t) = a(1 - t/t_c)^{1/(1-\omega)}, \quad v_0(t) = -\dot{x}_0 = \frac{a}{(1-\omega)\, t_c}(1 - t/t_c)^{\omega/(1-\omega)},$$

$$\rho_0(t) = \left\{\frac{1}{(1-\omega)\, t_c}\right\}^{-2\alpha+3} \frac{a^{2(1-\alpha)}}{\Lambda_0}(1 - t/t_c)^{\beta/(1-\omega)}, \text{ and } P_0(t) = \rho_0(t) v_0(t)^2, \tag{2.13}$$

where $\beta = \omega(3 - 2\alpha) - 1$. Since the dimensional scale is introduced only by Λ_0, the time dependence of the physical quantities cannot be fixed. Therefore, we leave ω as the free parameter. For convenience, instead of ω, we can use a parameter η which is given by

$$\eta = -\frac{(2-\alpha)\{(3-2\alpha)\omega - 1\}}{1-\omega}. \tag{2.14}$$

Using η, the time dependences of $\rho_0(t)$ and $P_0(t)$ are given by

$$\rho_0(t) \propto (1 - t/t_c)^{-\eta/(2-\alpha)} \text{ and } P_0(t) \propto (1 - t/t_c)^{(1-\eta)/(1-\alpha)}. \tag{2.15}$$

The self-similar equations are obtained as

$$(V + \xi)\frac{\mathrm{d}\ln\Omega}{\mathrm{d}\xi} + \frac{\mathrm{d}V}{\mathrm{d}\xi} = \beta, \tag{2.16}$$

$$(V + \xi)\frac{\mathrm{d}V}{\mathrm{d}\xi} + \frac{1}{\gamma\Omega}\frac{\mathrm{d}\ln(\Omega X^2)}{\mathrm{d}\xi} = \omega V, \tag{2.17}$$

and

$$(V + \xi)\left[\frac{2}{\gamma-1}\frac{\mathrm{d}\ln X}{\mathrm{d}\xi} - \frac{\mathrm{d}\ln\Omega}{\mathrm{d}\xi}\right] = \frac{2}{\gamma-1}\omega - \beta - \gamma\Omega X^{2(\alpha-1)}. \tag{2.18}$$

2.1.4 Homologous Special Solutions

The similarity equations (2.16), (2.17) and (2.18) have homologous special solutions with spatially uniform density and sound speed. Substituting $\Omega(\xi) = \Omega_0$ and $X(\xi) = X_0$ into the similarity equations (2.16), (2.17) and (2.18), one obtains

$$\frac{\mathrm{d}V}{\mathrm{d}\xi} = \beta, \tag{2.19}$$

$$(V + \xi)\frac{\mathrm{d}V}{\mathrm{d}\xi} = \omega V, \tag{2.20}$$

and

$$\frac{2\omega}{\gamma - 1} - \beta - \gamma\Omega_0 X_0^{2(\alpha-1)} = 0. \tag{2.21}$$

Equation (2.19) is integrated to give

$$V = \beta\xi, \tag{2.22}$$

where $V(\xi = 0) = 0$ is assumed. Substituting equation (2.22), equation (2.20) becomes

$$\beta\omega(\alpha - 1) = 0. \tag{2.23}$$

Therefore, the homologous solutions exist for $\beta = 0$ or $\omega = 0$ or $\alpha = 1$. Equation (2.21) gives the relation between Ω_0 and X_0. For $\beta = 0$, the solution is given by $\Omega(\xi) = \Omega_0$, $V(\xi) = 0$ and $X(\xi) = X_0$. The time dependence of density and sound speed are given by

$$\rho(t) = \text{const.} \quad \text{and} \quad c_{\mathrm{s}}(t) \propto (1 - t/t_{\mathrm{c}})^{1/(2-2\alpha)}, \tag{2.24}$$

respectively. This is the homologous isochoric mode. No homologous isochoric solution with equations (2.6) and (2.13) exists for $\alpha \geq 1$. This is because the sound speed increases with time by cooling from equation (2.24). This is unphysical behaviour. The solution with $\omega = 0$ shows isothermal condensation. For $\alpha = 1$, no self-similar solutions are found except for the homologous solutions as shown in section 2.2.

2.1.5 Asymptotic Behaviours

In this subsection, asymptotic behaviours of the self-similar solutions at $\xi \to \infty$ and $\xi \to 0$ are investigated.

Solutions for $\xi \to \infty$

Assuming that $\Omega(\xi)$ is decreasing function of ξ, $V(\xi)$ and $X(\xi)$ are increasing functions and $\mathrm{d}\ln|V|/\mathrm{d}\ln\xi = \mathrm{d}\ln X/\mathrm{d}\ln\xi < 1$, equations (2.16), (2.17) and (2.18) require

$$\xi\frac{\mathrm{d}\ln\Omega}{\mathrm{d}\xi} \simeq \beta, \;\; \xi\frac{\mathrm{d}V}{\mathrm{d}\xi} \simeq \omega V, \;\; \text{and} \;\; \xi\frac{\mathrm{d}\ln X}{\mathrm{d}\xi} \simeq \omega \tag{2.25}$$

in the lowest order. Expanding to the next order, the asymptotic solutions are given by

$$\Omega(\xi) \simeq \Omega_\infty \xi^\beta + \Omega_\infty^{(1)} \xi^{\beta+\omega-1}, \tag{2.26}$$

$$V(\xi) \simeq V_\infty \xi^\omega + V_\infty^{(1)} \xi^{2\omega-1}, \tag{2.27}$$

and

$$X(\xi) \simeq X_\infty \xi^\omega + X_\infty^{(1)} \xi^{2\omega-1}, \tag{2.28}$$

where

$$\Omega_\infty^{(1)} = \Omega_\infty V_\infty \frac{\beta+\omega}{1-\omega}, \tag{2.29}$$

$$V_\infty^{(1)} = \frac{1}{1-\omega}\left[\omega V_\infty^2 + \frac{X_\infty^2}{\gamma}(\beta+2\omega)\right], \tag{2.30}$$

and

$$X_\infty^{(1)} = \frac{(\gamma+1)\omega V_\infty X_\infty + \gamma(\gamma-1)\Omega_\infty X_\infty^{2(\alpha-1)}}{2(1-\omega)}. \tag{2.31}$$

Solutions for $\xi \to 0$

We expand $\Omega(\xi)$, $V(\xi)$ and $X(\xi)$ in the following forms:

$$\Omega(\xi) \simeq \Omega_{00} + \Omega_{00}^{(1)} \xi^\nu, \;\; V(\xi) \simeq V_{00}\xi + V_{00}^{(1)} \xi^{\nu+1},$$

and

$$X(\xi) \simeq X_{00} + X_{00}^{(1)} \xi^\nu. \tag{2.32}$$

Substituting equation (2.32) into (2.16), (2.17) and (2.18), we obtain the following relations for coefficients: V_{00} and $V_{00}^{(1)}$ are given by

$$V_{00} = \beta \;\; \text{and} \;\; V_{00}^{(1)} = -\frac{\nu(\beta+1)\Omega_{00}^{(1)}}{(\nu+1)\Omega_{00}}, \tag{2.33}$$

respectively. The relation between Ω_{00} and X_{00} is given by

$$\gamma(\gamma-1)\Omega_{00} X_{00}^{2(\alpha-1)} = 2\omega - \beta(\gamma-1). \tag{2.34}$$

The relation between $\Omega_{00}^{(1)}$ and $X_{00}^{(1)}$ is given by

$$\frac{\Omega_{00}^{(1)}}{\Omega_{00}} + 2\frac{X_{00}^{(1)}}{X_{00}} = 0, \tag{2.35}$$

and ν is given by

$$\nu = \frac{(2-\alpha)\epsilon_{00}}{\beta+1}, \tag{2.36}$$

where

$$\epsilon_{00} = (\gamma-1)\Omega_{00}X_{00}^{2(\alpha-1)} = \frac{2\omega - \beta(\gamma-1)}{\gamma} \tag{2.37}$$

2.1.6 Critical Point

Equations (2.16), (2.17) and (2.18) are rewritten as

$$\frac{\mathrm{d}\ln\Omega}{\mathrm{d}\xi} = \frac{I_2}{I_1}, \quad \frac{\mathrm{d}V}{\mathrm{d}\xi} = \frac{I_3}{I_1} \quad \text{and} \quad \frac{\mathrm{d}\ln X}{\mathrm{d}\xi} = \frac{I_4}{I_1}, \tag{2.38}$$

where

$$I_1 = (V+\xi)^2 - X^2, \quad I_2 = \frac{X^2}{V+\xi}g + f, \tag{2.39}$$

$$I_3 = -X^2 g + \beta I_1 - (V+\xi)f, \tag{2.40}$$

$$I_4 = -\frac{1}{2}\left[\frac{X^2 - \gamma(V+\xi)^2}{V+\xi}\right]g + \frac{\gamma-1}{2}f, \tag{2.41}$$

$$g(\Omega, X) = (\gamma-1)\left\{\Omega_{00}X_{00}^{2(\alpha-1)} - \Omega X^{2(\alpha-1)}\right\}, \tag{2.42}$$

and

$$f(\xi, V) = \beta(V+\xi) - \omega V. \tag{2.43}$$

The singular point exists where $I_1 = 0$ in each of the equations (2.38). This is the critical point ($\xi = \xi_{\mathrm{s}}$). In the self-similar solutions which is smooth at this point, the numerators (I_2, I_3 and I_4) must vanish at $\xi = \xi_{\mathrm{s}}$. Among four conditions $I_1 = I_2 = I_3 = I_4 = 0$, there are two independent conditions which are given by

$$(V+\xi)^2 = X^2 \quad \text{and} \quad \frac{X^2}{V+\xi}g + f = 0. \tag{2.44}$$

Topological Property of the Critical Point

In this subsection, the topological property of the critical point is investigated. We introduce a new variable s which is defined by $\mathrm{d}s = I_1 \mathrm{d}\xi$ (Whitworth and Summers, 1985). The dimensionless quantities at infinitesimal from the critical point, $s_\mathrm{s} + \delta s$, are given by

$$\vec{Q}(s_\mathrm{s} + \delta s) = \vec{Q}_\mathrm{s} + \delta \vec{Q}, \tag{2.45}$$

where $\vec{Q} = (\xi, \ln \Omega, V, \ln X)$. The subscript "$s$" indicates the value at the critical point. Substituting equation (2.45) into equations (2.38) and linearizing, one obtains

$$\frac{\mathrm{d}\delta Q_i}{\mathrm{d}s} = A_{ij}|_{\xi=\xi_\mathrm{s}} \delta Q_j, \quad A_{ij} = \frac{\partial I_i}{\partial Q_j}. \tag{2.46}$$

The eigenvalues, λ, of A_{ij} provide the topological property of the critical point. The eigenequation is given by

$$\left(\frac{\lambda}{X_\mathrm{s}}\right)^2 \left[\left(\frac{\lambda}{X_\mathrm{s}}\right)^2 + b\frac{\lambda}{X_\mathrm{s}} + c\right] = 0, \tag{2.47}$$

$$b = \epsilon_\mathrm{s}\left\{(\gamma-1)(\alpha-1)+1\right\} + \omega + \beta - 2 \tag{2.48}$$

and

$$\begin{aligned} c &= 2\gamma(\alpha-1)\epsilon_\mathrm{s}^2 \\ &+ (-\beta\gamma - 4\omega\alpha + 2\omega - 2\gamma\alpha + 2\alpha - 3 - 2\beta + \omega\gamma + \gamma)\epsilon_\mathrm{s} \\ &+ 4\omega - \beta + 2\omega^2 - \frac{4\omega^2 - \beta - 2\omega + 2\omega\beta}{\gamma}, \end{aligned} \tag{2.49}$$

where $\epsilon_\mathrm{s} = (\gamma-1)\Omega_\mathrm{s} X_\mathrm{s}^{2(\alpha-1)}$. The degenerate solution $\lambda = 0$ is attributed to the homologous special solutions (see subsection 2.1.4). Therefore, the topology is described by the two eigenvalues except for $\lambda = 0$.

2.1.7 Numerical Methods

In this subsection, our numerical method employed in solving the similarity equations (2.38) is described. We adopt s as the integrating variable. Using variable s, equations (2.38) are rewritten as

$$\frac{\mathrm{d}Q_i}{\mathrm{d}s} = I_i, \quad i = 1, 2, 3, 4, \tag{2.50}$$

which is not singular at the critical point.

The critical point is specified by (ξ_s, V_s) because there are four unknown quantities $\vec{Q}$ and two conditions (equations (2.44)). Moreover, the similarity equations (2.50) are invariant under a transformation $\xi \to m\xi$, $V \to mV$, $\Omega \to m^{-2(\alpha-1)}\Omega$, $X \to mX$, where m is an arbitrary constant. Therefore, the self-similar solution for $(m\xi_\mathrm{s}, mV_\mathrm{s})$ is the same as that for $(\xi_\mathrm{s}, V_\mathrm{s})$. Since one can take m in such a way that $(\xi_\mathrm{s}, V_\mathrm{s})$ satisfy a relation $\xi_\mathrm{s}^2 + V_\mathrm{s}^2 = 1$, the critical point is specified by only ξ_s.

Given ξ_s, the velocity is obtained as $V_\mathrm{s} = -\sqrt{1-\xi_\mathrm{s}^2}$. From equations (2.44), Ω_s and X_s are determined. Since $X_\mathrm{s} = V_\mathrm{s} + \xi_\mathrm{s}$ is positive, the range of ξ_s is $1/\sqrt{2} < \xi_\mathrm{s} < 1$. The similarity equations (2.50) are integrated from ξ_s to both directions ($\xi \to 0$ and $\xi \to \infty$) along the gradient derived from equation (2.46) using fourth-order Runge-Kutta method. The position of the critical point ξ_s is determined iteratively by bisection method until the solution satisfies the asymptotic solutions (see subsection 2.1.5).

2.2 Results

2.2.1 Physically Possible Range of Parameters (η, α)

In this section, we constrain the parameter space (η, α) by physical properties of the flow.

A Range of η

Using equation (2.15), the time dependence of the central density and pressure is given by

$$\rho_{00}(t) \propto (1 - t/t_\mathrm{c})^{-\eta/(2-\alpha)} \ \text{ and } \ P_{00}(t) \propto (1 - t/t_\mathrm{c})^{(1-\eta)/(1-\alpha)}, \tag{2.51}$$

where the subscript “00” indicates the value at the center, $x = 0$. During self-similar condensation by cooling, the central density (pressure) must increases (decreases) monotonically with time. Therefore, the following two conditions are obtained:

$$-\frac{\eta}{2-\alpha} < 0 \quad \Longrightarrow \eta > 0 \tag{2.52}$$

and

$$\frac{1-\eta}{1-\alpha} > 0 \quad \Longrightarrow \begin{cases} \eta < 1 & \text{for} \quad \alpha < 1 \\ \eta > 1 & \text{for} \quad \alpha > 1\ . \end{cases} \tag{2.53}$$

From equations (2.52) and (2.53), the range of η is given by

$$\begin{cases} 0 < \eta < 1 & \text{for} \quad \alpha < 1 \\ \eta > 1 & \text{for} \quad \alpha > 1 \ . \end{cases} \tag{2.54}$$

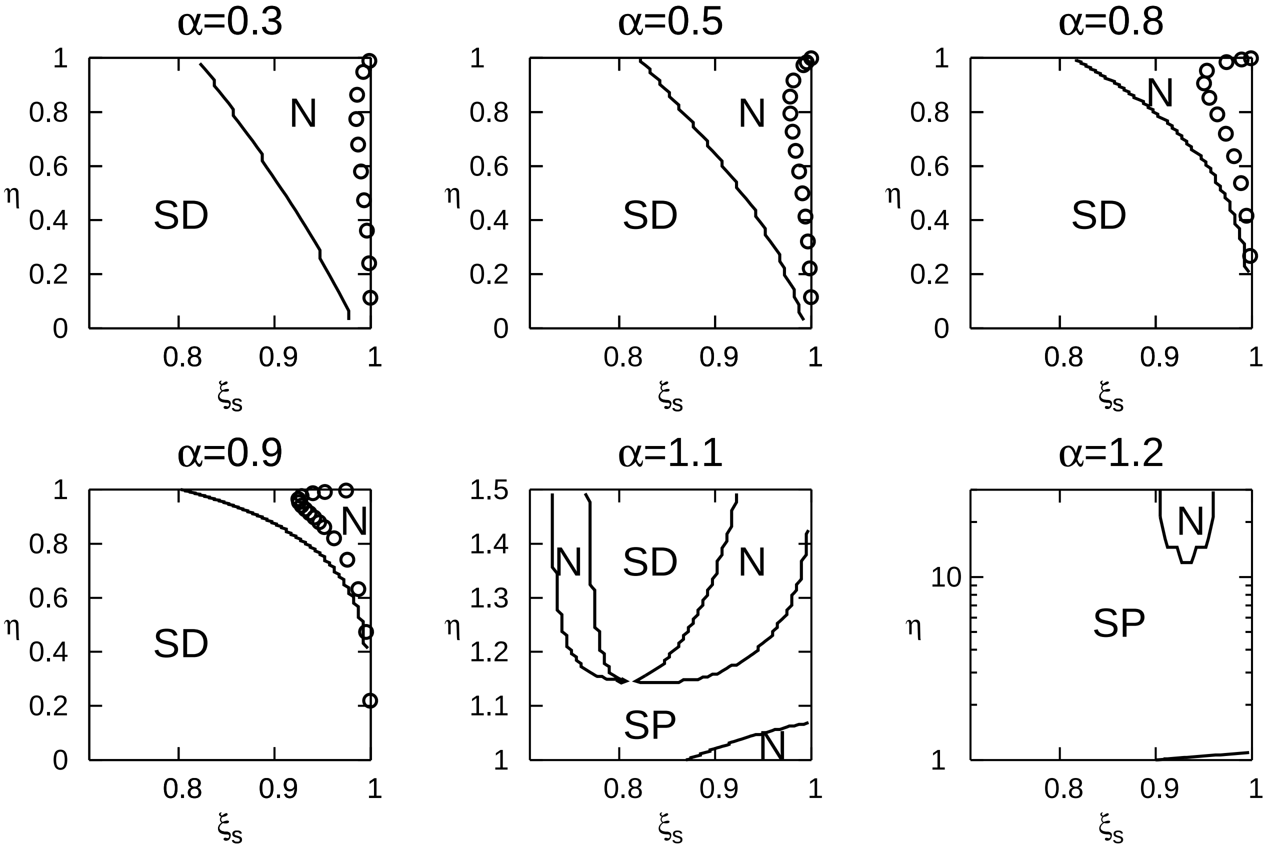

Figure 2.1: Topological property of the critical point for α =0.3, 0.5, 0.8, 0.9, 1.1 and 1.2. The ordinates and abscissas are η and ξ_s, respectively. The letters "N", "SD", and "SP" indicate a node, a saddle and a spiral, respectively. The open circles indicate obtained self-similar solutions.

A range of α

In the similarity equations (2.50), the critical point is specified by α, η and ξ_s. The property of the critical point is given by the two eigenvalues of the eigenequation (2.47) except for $\lambda = 0$. When the two eigenvalues are real and have the same sign, the critical point is referred to a node. When the two eigenvalues are real and have the opposite sign, the critical point is referred to a saddle. When the two eigenvalues are complex, the critical point is called a

η	n	$-\eta/(2-\alpha)$	$(1-\eta)/(1-\alpha)$	$\xi_{\rm s}$	Ω_{00}	X_{00}	Ω_∞	V_∞	X_∞
0.059	1.923	-0.039	1.882	0.9999	0.873	0.977	0.882	-0.0234	0.0408
0.272	1.818	-0.181	1.455	0.9975	0.768	0.883	0.782	-0.124	0.201
0.500	1.667	-0.333	1.000	0.9907	0.643	0.766	0.612	-0.244	0.391
0.692	1.538	-0.462	1.538	0.9820	0.528	0.652	0.420	-0.323	0.555
0.761	1.493	-0.507	0.615	0.9792	0.486	0.609	0.343	-0.333	0.613
0.857	1.429	-0.571	0.478	0.9779	0.426	0.546	0.234	-0.314	0.697
0.945	1.370	-0.631	0.110	0.9853	0.360	0.472	0.123	-0.223	0.805
0.995	1.337	-0.663	0.011	0.9986	0.237	0.315	0.0260	-0.0576	0.952

Table 2.1: Relevant parameters for obtained self-similar solution ($\alpha = 0.5$) are summarized.

spiral. Figure 2.1 shows the topology of the critical point in the parameter space ($\xi_{\rm s}$, η) for index parameter $\alpha = 0.3$, 0.5, 0.8, 0.9, 1.1 and 1.2. In figure 2.1, the letters "N", "SD", and "SP" indicate a node, a saddle and a spiral, respectively. The ranges of the parameters are $1/\sqrt{2} < \xi_{\rm s} < 1$ and equations (2.54). The open circles indicate the numerically obtained self-similar solutions presented in section 2.2.4. Figure 2.1 shows that the topology drastically changes at $\alpha = 1$. For $\alpha < 1$, since the critical point is a node or a saddle, the self-similar solutions is expected to exist. For $\alpha \simeq 1.1$, non-negligible fraction of the parameter space is covered by a spiral. Almost all parameter region is a spiral for $\alpha \geq 1.2$. We searched and found the self-similar solution which connects $0 < \xi < \infty$ only in N and SD for $\alpha < 1$.

Relevant parameters (η, n, $-\eta/(2-\alpha)$, $(1-\eta)/(1-\alpha)$, $\xi_{\rm s}$, Ω_{00}, X_{00}, Ω_∞, V_∞, X_∞) for obtained self-similar solution for $\alpha = 0.5$ are summarized in table 2.1.

2.2.2 Fixed Normalization of Self-Similar Solutions

As mentioned in section 2.1.7, the similarity equations (2.50) are invariant under a transformation $\xi \to m\xi$, $V \to mV$, $\Omega \to m^{-2(\alpha-1)}\Omega$, $X \to mX$, where m is an arbitrary constant. For convenience for numerical integration, we select m so that the relation, $\xi_{\rm s}^2 + V_{\rm s}^2 = 1$ is satisfied. This choice of m does not have any physical meaning. In this section, we select m so that the length scale is scaled by the cooling length at $x = 0$ as

$$x = \lambda_{\rm cool}(t)\xi, \quad \lambda_{\rm cool}(t) = \lambda_{\rm cool}(t=0)(1 - t/t_{\rm c})^{1/(1-\omega)}. \tag{2.55}$$

This selection of m has physical meaning.

We determine m so that equation (2.55) is satisfied as follows; the cooling length is given by

$$\lambda_{\rm cool}(t) = c_{00}(t)\frac{P_{00}(t)}{(\gamma-1)\Lambda_0\rho_{00}(t)^2c_{00}(t)^{2\alpha}}. \tag{2.56}$$

Using equation (2.13), equation (2.56) can be rewritten as

$$\lambda_{\rm cool}(t) = a\frac{\Omega_{00}^{-1}X_{00}^{3-2\alpha}}{\gamma(\gamma-1)}(1-t/t_{\rm c})^{1/(1-\omega)} = \frac{\Omega_{00}^{-1}X_{00}^{3-2\alpha}}{\gamma(\gamma-1)}x_0(t). \tag{2.57}$$

Performing the following scaling transformation, $\xi \to m\xi$, $V \to mV$, $\Omega \to m^{-2(\alpha-1)}\Omega$, $X \to mX$, equation (2.57) becomes

$$\lambda_{\rm cool}(t) = m\frac{\Omega_{00}^{-1}X_{00}^{3-2\alpha}}{\gamma(\gamma-1)}x_0(t). \tag{2.58}$$

Therefore, if we select

$$m = \gamma(\gamma-1)\Omega_{00}X_{00}^{2\alpha-3}, \tag{2.59}$$

$x_0(t)$ is coincident with the cooling length, or

$$\lambda_{\rm cool}(t) = x_0(t). \tag{2.60}$$

Using this transformation and equation (2.34), the central values of Ω, Π and X become

$$\Omega_{00} = \frac{(\gamma\epsilon_{00})^{3-2\alpha}}{\gamma(\gamma-1)}, \quad \Pi_{00} = \frac{(\gamma\epsilon_{00})^{5-2\alpha}}{\gamma^2(\gamma-1)}, \quad \text{and} \quad X_{00} = \gamma\epsilon_{00}, \tag{2.61}$$

respectively. From equations (2.61), the cooling time at $x = 0$ is

$$t_{\rm cool} = \frac{P_{00}(t)}{(\gamma-1)\Lambda_0\rho_{00}(t)^2c_{00}^{2\alpha}} = \frac{1-\omega}{\gamma\epsilon_{00}}t_{\rm c}(1-t/t_{\rm c}). \tag{2.62}$$

Therefore, the collapse time can be expressed using the cooling time at $t = 0$ as

$$t_{\rm c} = \frac{\gamma\epsilon_{00}}{1-\omega}t_{\rm cool}(t=0) \tag{2.63}$$

Using this normalization, equation (2.13) can be written as

$$x_0(t) = \lambda_{\rm cool}(t), \quad v_0(t) = \frac{c_{00}(t)}{\gamma\epsilon_{00}}$$

$$\rho_0(t) = \frac{\gamma(\gamma-1)}{(\gamma\epsilon_{00})^{3-2\alpha}}\rho_{00}(t), \quad \text{and} \quad P_0(t) = \rho_0(t)v_0(t)^2. \tag{2.64}$$

Hereafter, this normalization is used.

2.2.3 Physical Meaning of Parameter η

New self-similar solutions have one free parameter η that ranges from 0 to 1. In this section, we show that the parameter η is related to the ratio of the scale length of the condensing region to the cooling length. The scale length of the central condensing region, $x_{\rm L}$, is defined by the condition,

$$\frac{\rho(x_{\rm L}(t),t)}{\rho(0,t)}=\frac{\Omega(\xi_{\rm L})}{\Omega_{00}}=0.8, \tag{2.65}$$

where $\xi_{\rm L}$ is the similarity coordinate with respect to $x_{\rm L}$. Using equation (2.55), the ratio of the scale length of the condensing region to the cooling length is given by

$$\frac{x_{\rm L}}{\lambda_{\rm cool}(t)}=\xi_{\rm L} \tag{2.66}$$

Equation (2.66) shows that the ratio is independent of time. Figure 2.2 indicates the dependence of $x_{\rm L}/\lambda_{\rm cool}$ on the parameter η for $\alpha=-0.5$, 0.5 and 0.8. Figure 2.2 shows that $x_{\rm L}/\lambda_{\rm cool}\gg 0$ for $\eta\to 0$ and $x_{\rm L}/\lambda_{\rm cool}\ll 1$ for $\eta\to 1$ without depending on α. Therefore, we can discuss behaviours of the self-similar solutions for $\eta\sim 0$ and $\eta\sim 1$ in the same way in section 1.4.1.

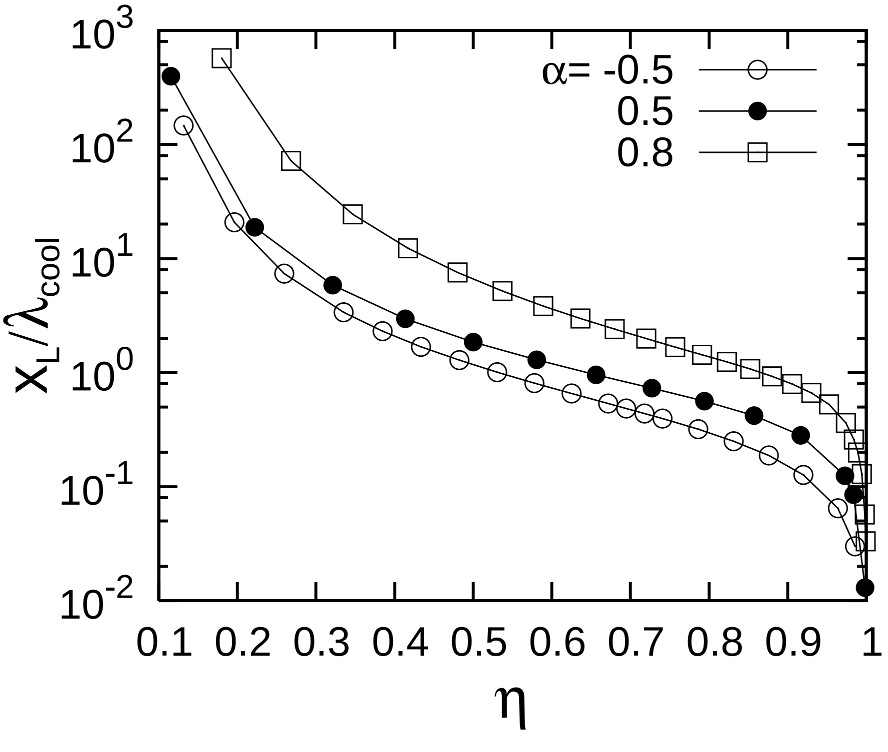

Figure 2.2: The dependence of the ratio of the scale of the condensing ration $x_{\rm L}$ to the cooling length $\lambda_{\rm cool}$ on the parameter η for $\alpha=-0.5$ (the open circles), 0.5 (the filled circles), and 0.8 (the open boxes).

$\boldsymbol{\eta \sim 0}$ ($\boldsymbol{x_{\rm L} \gg \lambda_{\rm cool}}$) This self-similar solution describes the large scale condensation. In this situation, the pressure drops while the density does not increase so much. From equation (2.51), the time evolutions of the central density and pressure are given by

$$\rho_{00}(t) \simeq \text{const.} \quad \text{and} \quad P_{00}(t) \propto (1 - t/t_{\rm c})^{1/(1-\alpha)}, \tag{2.67}$$

respectively. Therefore, this self-similar solution corresponds to the isochorically cooling layer.

$\boldsymbol{\eta \sim 1}$ ($\boldsymbol{x_{\rm L} \ll \lambda_{\rm cool}}$) This self-similar solution describes the small scale condensation. In this situation, the gas is expected to condense in pressure equilibrium with their surroundings. From equation (2.51), the time evolutions of the central density and pressure are given by

$$\rho_{00}(t) \propto (1 - t/t_{\rm c})^{-1/(2-\alpha)} \quad \text{and} \quad P_{00}(t) \simeq \text{const.}, \tag{2.68}$$

respectively. Therefore, this self-similar solution corresponds to the isobarically condensing layer.

The critical value of $\eta = \eta_{\rm eq}$ is given by the condition that the increasing rate of $\rho_{00}(t)$ is equal to the decreasing rate of $P_{00}(t)$, which is given by

$$\eta_{\rm eq} = \frac{2-\alpha}{3-2\alpha}. \tag{2.69}$$

For $\eta = \eta_{\rm eq}$, the time dependence of ρ_{00} and P_{00} is given by

$$\rho_{00}(t) \propto (1 - t/t_{\rm c})^{-1/(3-2\alpha)} \quad \text{and} \quad P_{00}(t) \propto (1 - t/t_{\rm c})^{1/(3-2\alpha)}. \tag{2.70}$$

Therefore, the self-similar solutions for $0 < \eta < \eta_{\rm eq}$ and $\eta_{\rm eq} < \eta < 1$ are close to the isochorically and the isobarically condensing layers, respectively. The family of the self-similar solutions describe nonlinear evolutions of thermal instability of all length scales.

2.2.4 Self-Similar Solutions

In this section, we present the obtained self-similar solutions for the $\eta = 0.98$, 0.76 and 0.12. The index parameter of the net cooling rate α is set to 0.5. The self-similar solutions for $\eta = 0.98$ and $\eta = 0.12$ are representative solutions of isobarically condensing layer and

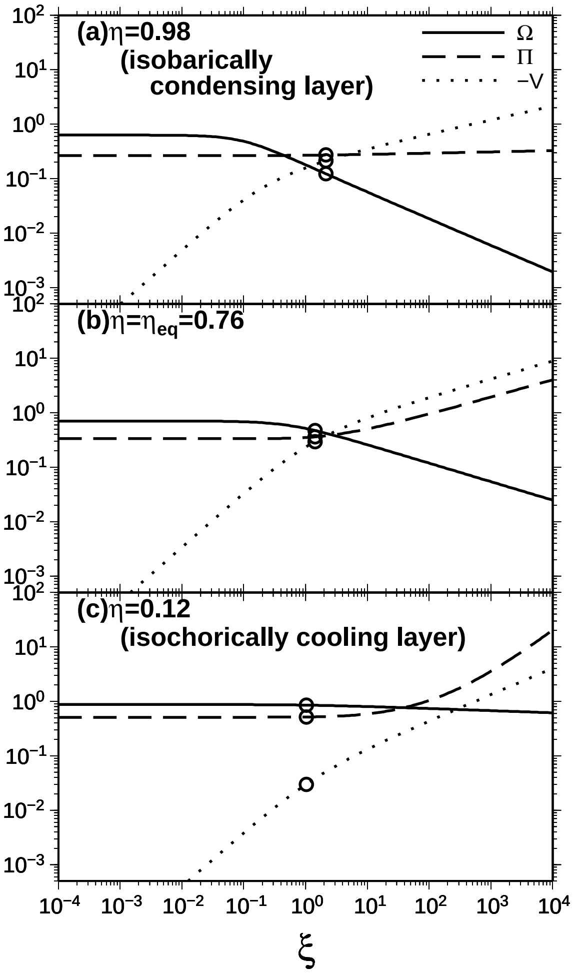

Figure 2.3: The distributions of the dimensionless density Ω, velocity $-V$, and pressure Π for (a)$\eta = 0.98$ (the isobarically condensing layer), (b)0.76 and (c)0.12 (the isochorically cooling layer). The open circles indicate the critical points.

isochorically cooling layer, respectively. The self-similar solution for $\eta = 0.76 = \eta_{\rm eq}$ indicates the intermediate case between the two limits (see equation (2.69)).

Figure 2.3a, 2.3b and 2.3c show the distributions of the dimensionless variables (Ω, Π, and $-V$) as a function of the dimensionless coordinate ξ for $\eta = 0.98$, 0.76 and 0.12, respectively. The open circles indicate the critical points (see section 2.1.6). For the isobarically condensing layer ($\eta = 0.98$), the density has a sharply peaked distribution. On the other hand, the pressure is spatially constant. For the isochorically cooling layer ($\eta = 0.12$), the density and pressure profiles are opposite to those for $\eta = 0.98$. The density is spatially constant and the pressure sharply declines towards $\xi = 0$. For $\eta = 0.76$, the profiles of the density and pressure raises and declines towards $\xi = 0$, respectively.

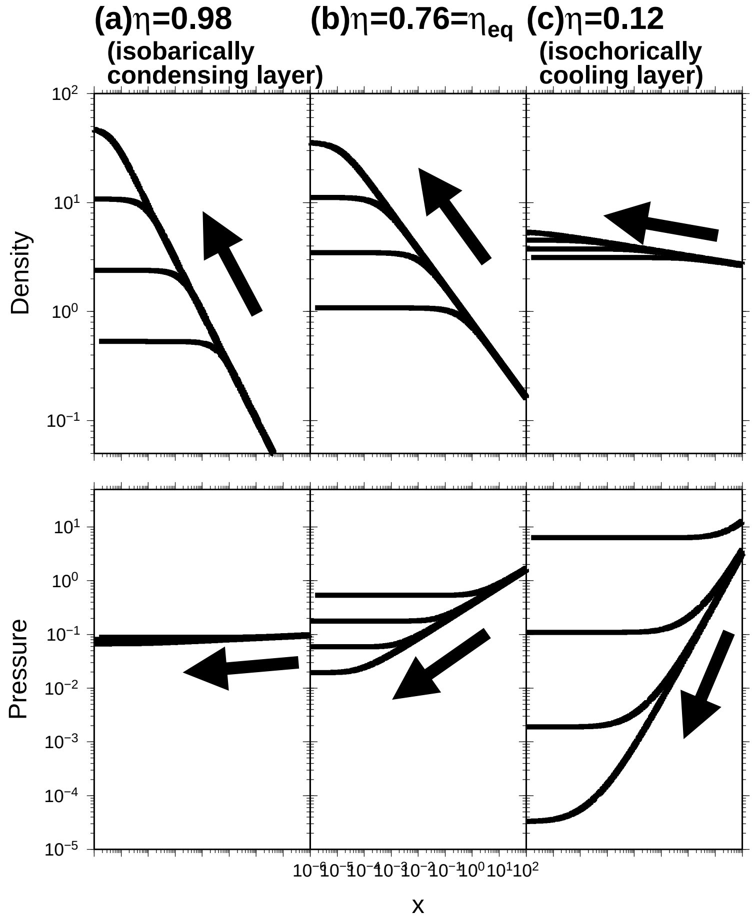

Figure 2.4: Time evolution of density ρ and pressure P. The each line is corresponding to $1 - t/t_{\rm c} = 1$, 0.1, 0.01 and 0.001 in the direction of the arrows. Each column is corresponding to (a)$\eta = 0.98$ (the isobarically condensing layer), (b)0.76 and (c)0.12 (the isochorically cooling layer) from left to right, respectively.

Figure 2.4a, 2.4b and 2.4c show the time evolutions of the density and pressure for $\eta = 0.98$, 0.76 and 0.12, respectively. Figure 2.4a clearly shows that the self-similar solution for $\eta = 0.98$ describes the isobarically condensing layer. The self-similar solutions for smaller η correspond to the larger scale condensation (see section (2.2.3)). Therefore, figure 2.4b ($\eta = 0.76$) shows that the pressure cannot be maintained constant and decreases with time. Figure 2.4c clearly shows that the self-similar solutions for $\eta = 0.12$ describe the isochorically cooling layer.

Finally, we mention the range of α where the self-similar solutions exist. When $\alpha = 1.0$, no self-similar solutions are found except for the homologous special solutions (see section 2.1.4). For $\alpha > 1.0$, we cannot find any self-similar solutions. Fouxon et al. (2007) found a family of exact solutions for $\alpha = 1.5 > 1$. Their solutions are not self-similar because $t_{\rm sound} \propto (1 - t/t_{\rm c})^{3/2}$ and $t_{\rm cool} \propto (1 - t/t_{\rm c})$ around center obey different scaling laws. During condensation, since t_{sound} becomes much smaller than t_{cool}, pressure of the central region is expected to be constant and the isobaric approximation is locally valid. Moreover, as mentioned in section 2.1.4, there are no homologous isochoric solutions for $\alpha > 1$. Therefore, for $\alpha > 1$, condensation is not expected to become self-similar.

2.3 Discussion

2.3.1 Comparison with One-dimensional Numerical Simulation

In this section, we investigate whether the obtained self-similar solutions can describe results of time-dependent numerical hydrodynamics for converging flows using one-dimensional Lagrangian 2nd-order Godunov method (van Leer, 1997) or not. We calculate two cases of the power law net cooling rate and realistic cooling rate of the ISM.

Converging flow with Power-law Net Cooling Rate

First, we consider the following power-law cooling rate,

$$\mathcal{L}(\rho, T) = \frac{1}{\gamma - 1}(\sqrt{\rho P} - 1), \tag{2.71}$$

that corresponds to $\alpha = 0.5$ in equation (1.2). We consider a convergence inflow of the gas that is distributed uniformly and is in thermal equilibrium ($\rho(x) = P(x) = 1$). A initial velocity field is given by

$$v(x) = -2\tanh(x/L), \tag{2.72}$$

where L is a free parameter in this calculation which specifies the finite scale of compressed layer. The scale of perturbation in the postshock region can be changed by changing of L. As L is larger, the scale of perturbation becomes larger. We perform numerical simulations for $L = 0.005$, 0.01, 0.02, 0.2, and 0.5. The inflow creates two shock waves which propagate outward. Runaway condensation occurs in the postshock region because the gas is thermally unstable. The maximum density continues to increase and ultimately becomes singular. During the runaway condensation, the gas around the center is expected to lost initial memory and to converge to one of the self-similar solutions. Since the self-similar solution have one parameter η that relates with the scale of the condensation, the parameter L in the calculation is expected to determine which η is chosen.

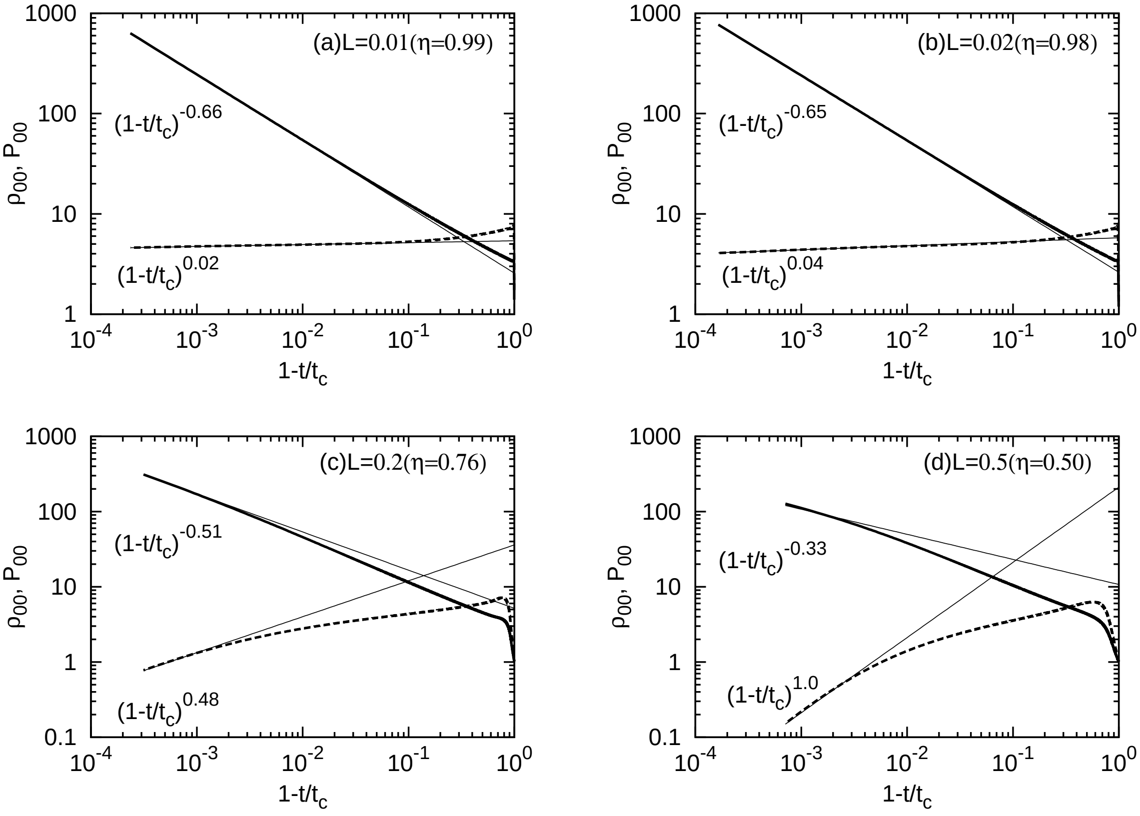

Figure 2.5: The time evolution of ρ_{00} (the thick lines) and P_{00} (the dashed lines) as the function of $1-t/t_\mathrm{c}$ for (a)$\lambda = 0.01$, (b)0.02, (c)0.2 and (d)0.2. The thin solid lines indicate the corresponding self-similar solutions. The direction of the time is from the right to the left.

To determine η, we investigate the time evolution of ρ_{00} and P_{00} that are shown in figure 2.5 as the function of $1 - t/t_\mathrm{c}$, where t_c is an epoch when ρ_{00} becomes singular estimated from the numerical results. Using equation (2.51), the time evolution of $\rho_{00}(t)$ and $P_{00}(t)$ in each simulation provides the corresponding η. Each panel indicates the case with (a)$L = 0.01$, (b)0.02, (c)0.2 and (d)0.5. As a result, the corresponding η are given by (a)0.99, (b)0.98, (c)0.76 and (d)0.50, respectively. The thin solid lines in figure 2.5 indicate the corresponding self-similar solutions. From the value of η and figure 2.5, the cases with (a) and (b) correspond to the nearly isobaric mode, the case with (c) corresponds to the intermediate mode ($\eta \sim \eta_\mathrm{eq}$) and the case with (d) corresponds to the isochoric mode.

Figure 2.6 shows the time evolution of the rescaled density $\rho(1-t/t_\mathrm{c})^{\eta/(2-\alpha)}$ and pressure $P(1 - t/t_\mathrm{c})^{-(1-\eta)/(1-\alpha)}$ as a function of the rescaled coordinate $x(1 - t/t_\mathrm{c})^{-1/(1-\omega)}$. The parameters L and η in each panel in figure 2.6 are the same as that in figure 2.5. The thick gray lines in figure 2.6 indicate the corresponding self-similar solutions. In all the cases

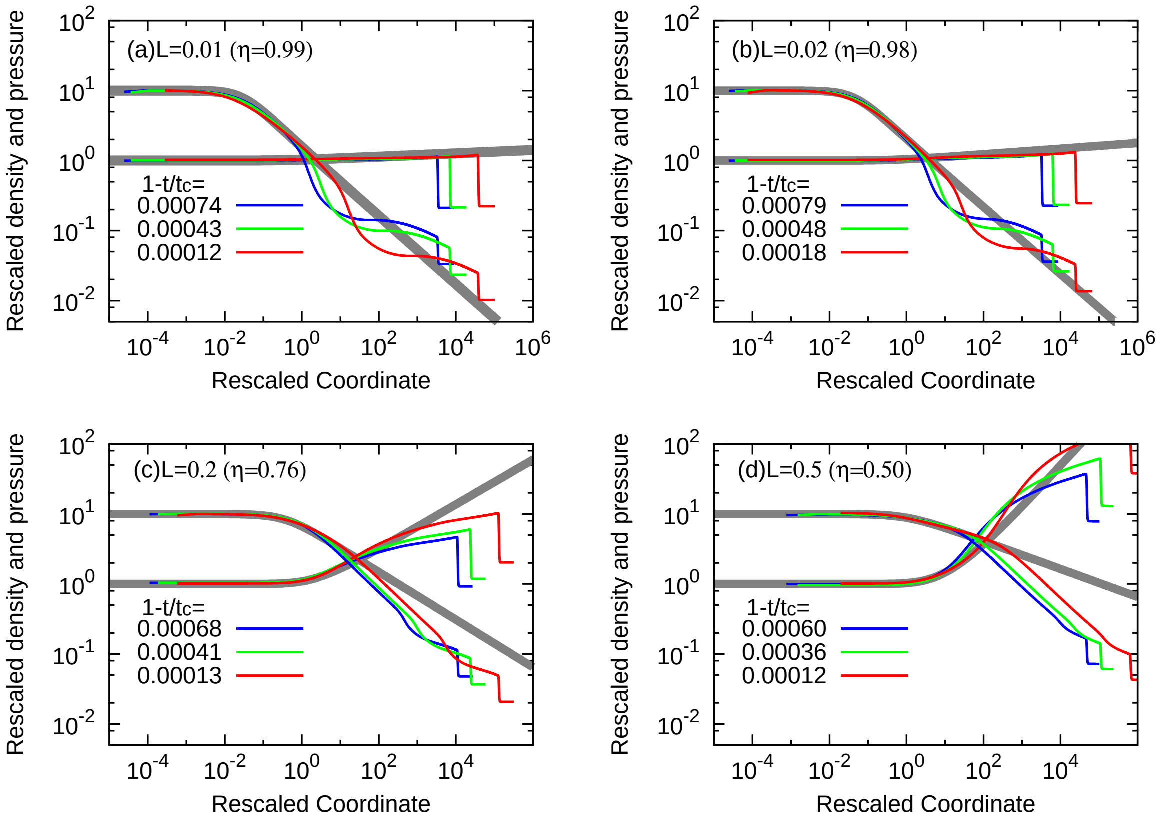

Figure 2.6: The distribution of the rescaled density $\rho(1-t/t_c)^{\eta/(2-\alpha)}$ and pressure $P(1-t/t_c)^{-(1-\eta)/(2-\alpha)}$ as the function of scaled coordinate $x(1-t/t_c)^{-1/(1-\omega)}$. In each panel, L and η are the same as that in figure 2.5. The lines are labeled by $1-t/t_c$. The rescaled density and pressure at the center set 10 and 0.1, respectively. The thick gray lines indicate the corresponding self-similar solutions.

(a-d), profiles of the density and pressure in the central region are well approximated by the corresponding self-similar solution. Moreover, it is seen that the region well approximated by the self-similar solution spreads with time in each panel. However, there is difference of the convergence speed to the corresponding self-similar solution. Figure 2.5 shows that the convergences of (a) and (b) are faster than that of (c) and (d). This is because the scale lengths of the condensed regions of (a) and (b) are smaller and sound wave can travel the cooling length many times.

From the above discussion, the nonlinear evolution of the perturbation is well approximated by the self-similar solution in large density limit. Which self-similar solution ($0 < \eta < 1$) is more likely to realise in actual environments where various-scale perturbations exist? To answer the question, the dependence of t_c on L is investigated. Figure 2.7 shows the dependence of $1/t_c$ on $1/L$. Here, $1/L$ and $1/t_c$ correspond to the wavenumber and the

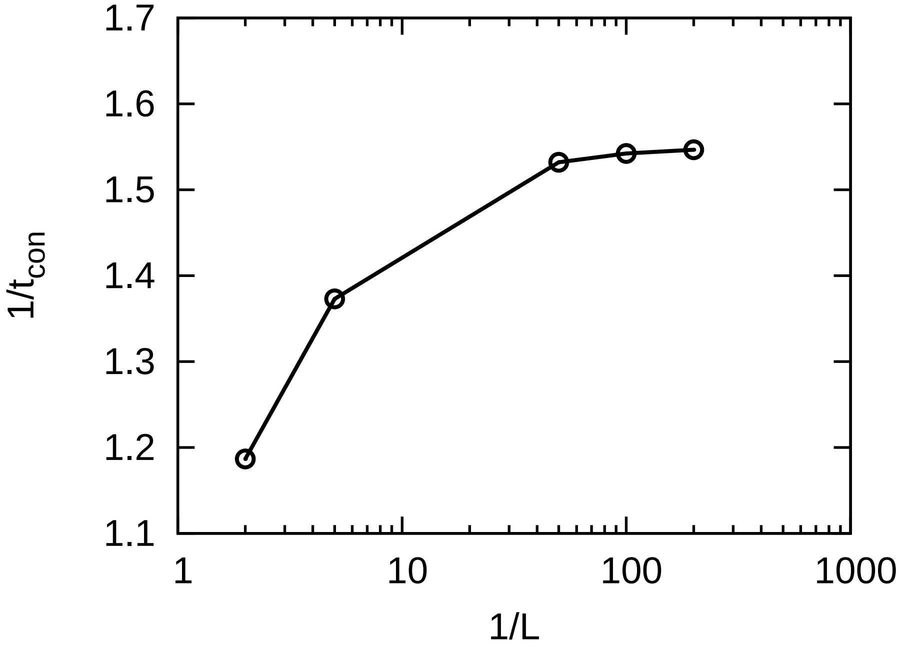

Figure 2.7: The dependence of the growth rate $1/t_{\rm c}$ on the wavenumber $1/L$.

growth rate of thermal instability, respectively. Therefore, figure 2.7 can be interpreted as an approximate dispersion relation for the nonlinear evolution of thermal instability. As $1/L$ is larger, $1/t_{\rm c}$ becomes larger and it seems that $1/t_{\rm c}$ approach a certain value asymptotically. The similar behaviour is also found in the dispersion relation of Field (1965) without heat conduction. This behaviour also can be seen from equation (2.63) that can be rewritten as

$$t_{\rm c} = \left\{ \frac{1}{1-\alpha} - \frac{1-(\gamma-1)(1-\alpha)}{(2-\alpha)(1-\alpha)}\eta \right\} t_{\rm cool}(t=0). \tag{2.73}$$

Since $\alpha < 1$ and $\gamma < 2$, equation (2.73) is the decreasing function of η. Therefore, if initial cooling time $t_{\rm cool}(t=0)$ is given, the collapse time $t_{\rm c}$ is shorter in the self-similar solutions for larger η. Therefore, from figure 2.7 and equation (2.73), the isobaric condensation is expected to realize in actual astrophysical environments. In this environment, nonlinear interaction between the isobaric and the isochoric modes will also be important.

Converging Flow with the Cooling Rate of the Interstellar Medium

The one-dimensional calculation has already done in section 1.7. In this section, we investigate whether the runaway condensing layer can be described by the self-similar solution or not. The self-similar solutions are specified by α and η. First, We evaluate the power index of the highest density portion of the gas, $\alpha_{\rm num}$ that is defined as

$$\alpha_{\rm num} = \left(\frac{\partial(\rho\mathcal{L})}{\partial T} \right)_\rho \Bigg|_{x=x_{\rm max}} \tag{2.74}$$

at each instant of time, where $x_{\rm max}(t)$ indicates the coordinate of the density peak. Figure 2.8 shows the time evolution of $\alpha_{\rm num}$. It is seen that $\alpha_{\rm num} \sim 0.61$ is approximately constant during $0.4\,{\rm Myr} < t < 0.95\,{\rm Myr}$. In this phase, the power-law cooling rate with $\alpha = 0.61$ in equation (1.2) describes the real cooling rate well. Next, we determine η from the time evolution of the maximum density $\rho_{\rm max}$ that is shown in figure 2.9 as a function of $1 - t/t_{\rm c}$, where $t_{\rm c} = 0.958$ Myr. This evolution of $\rho_{\rm max}$ is well described by the self-similar solution with $(\alpha, \eta) = (0.61, 0.98)$ that is shown by thin solid line.

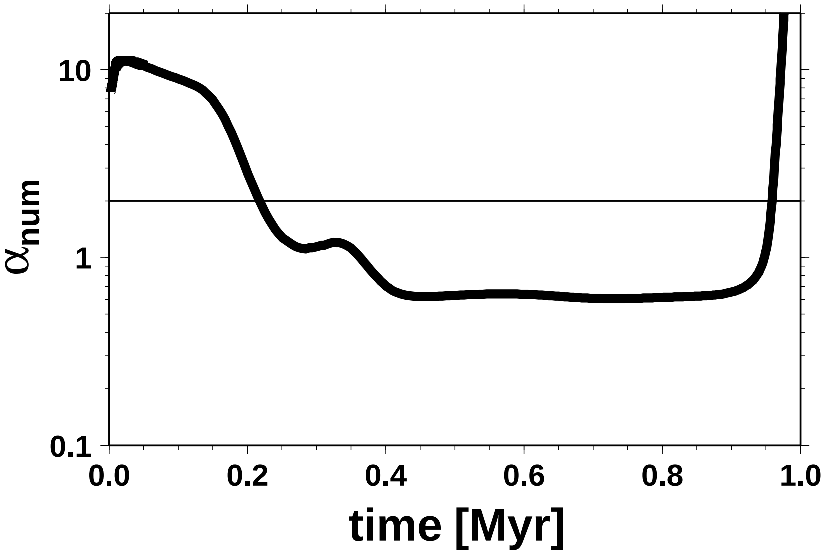

Figure 2.8: The time evolution of $\alpha_{\rm num}$ at the highest density portion. The region below the horizontal thin solid line ($\alpha_{\rm num} = 2$) is thermally unstable where the Balbus criterion for the isobaric mode (1.28) is satisfied.

The density and temperature profiles in figure 1.12 are compared to those of the self-similar solution with $(\alpha, \eta) = (0.61, 0.98)$. Figure 2.10 show the snapshots of (a) the rescaled number density, $n(1-t/t_{\rm c})^{\eta/(2-\alpha)}$, and (b) the temperature, $T(1-t/t_{\rm c})^{\{\eta-(2-\alpha)\}/\{(2-\alpha)(1-\alpha)\}}$, as a function of the rescaled coordinate, $x(1-t/t_{\rm c})^{-1/(1-\omega)}$ at $t = 0.80$, 0.90, and 0.95. The thick gray lines indicate the corresponding self-similar solution. From figure 2.10, one can see that the self-similar solution describes the results of the one-dimensional simulation very

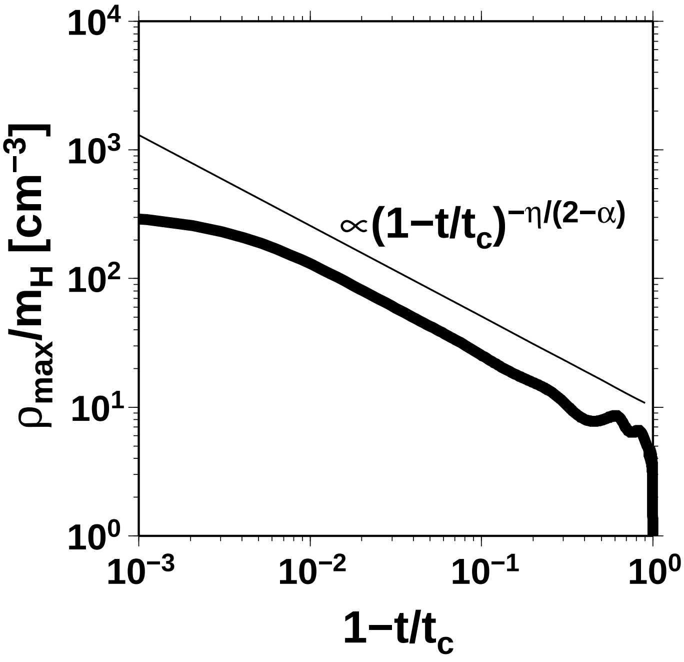

Figure 2.9: The time evolution of $\rho_{\rm max}$ as a function of $1-t/t_{\rm c}$. The thin solid line corresponds to the increasing rate of ρ_{00} with $(\alpha,\eta)=(0.61,0.98)$. The direction of the time is from the right to the left.

well. We also confirm the isobaric self-similar solutions can describe results of simulations for the case with different initial density fluctuation (see equation 1.36).

2.3.2 Effects of Dissipation

In the actual gas, the effect of viscosity and heat conduction becomes important in small scale. The importance of dissipation can be evaluated by the ratio between the advection and the dissipation terms, or Raynolds number which is given by

$$\mathcal{R}=\frac{C_{\rm V}\rho v\partial_x T}{\partial_x(K(T)\partial_x T)}\sim\frac{C_{\rm V}\rho_{00}Ux_{\rm L}}{K(T_{00})},\tag{2.75}$$

where $C_{\rm V}$, $K(T)$ and U are the specific heat at constant volume, the heat conduction coefficient and typical velocity, respectively, and $x_{\rm L}$ is the scale length of the condensing region that is defined in equation (2.66). Plandtl number is implicitly assumed to be order unity. If the flow converges to one of the self-similar solutions, the ratio ζ between the scale length of the condensing region $x_{\rm L}$ and the cooling length $\lambda_{\rm cool}$ is constant. Therefore ζ is defined

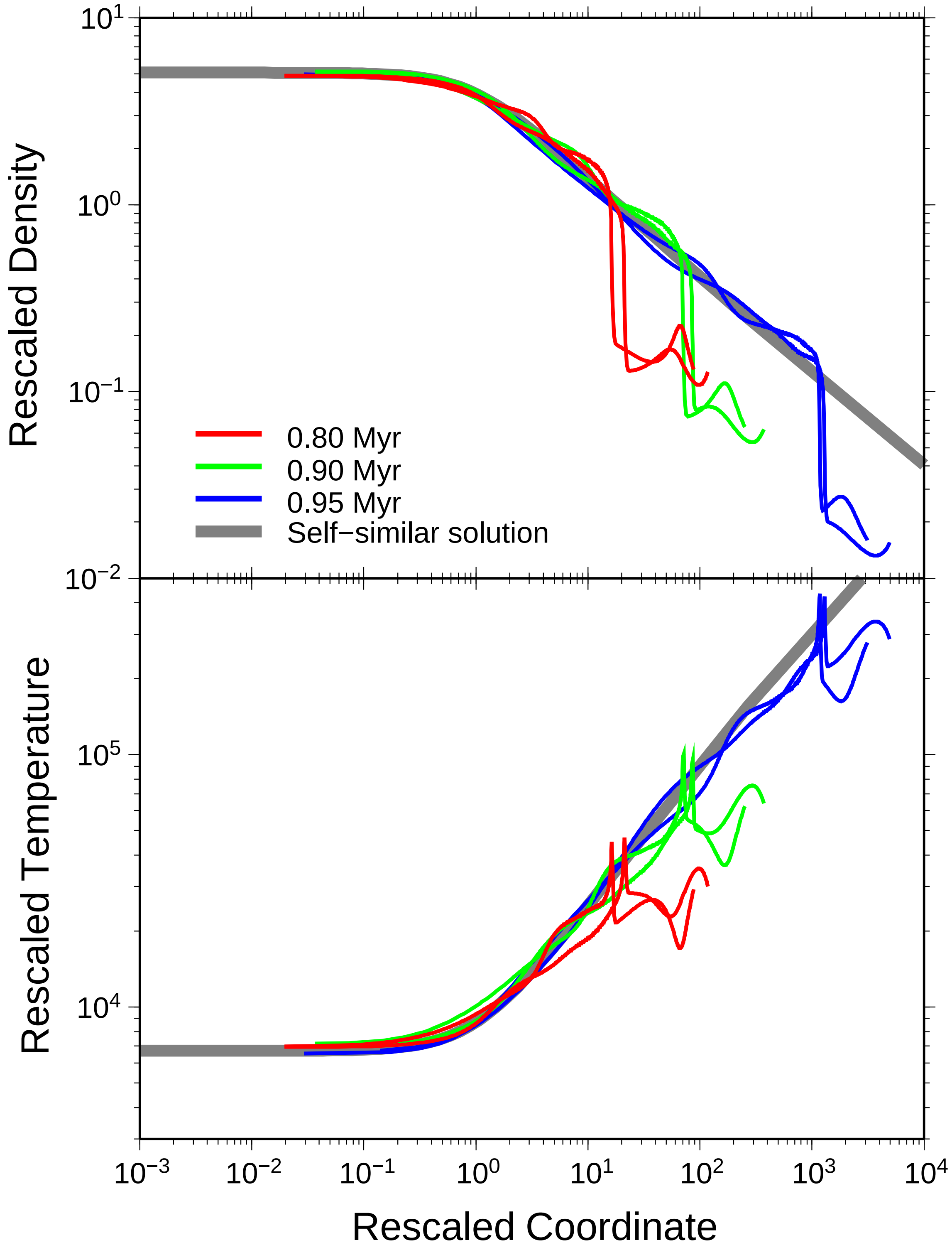

Figure 2.10: The rescaled (a)number density, $n(1 - t/t_{\rm c})^{\eta/(2-\alpha)}$ and (b)temperature, $T(1 - t/t_{\rm c})^{(1-\alpha)(1-\eta)/\{\eta(2-\alpha)\}}$ as a function of the rescaled coordinate, $x(1 - t/t_{\rm c})^{-1/(1-\omega)}$, where $t_{\rm c}$ and η are set to 0.958 Myr and 0.98, respectively. The thick gray lines in (a) and (b) indicate the corresponding self-similar solution.

by

$$\zeta = \frac{x_{\mathrm{L}}(t)}{\lambda_{\mathrm{cool}}(t)} = x_{\mathrm{L}}(t)\gamma(\gamma-1)\Lambda_0\rho_{00}c_{00}^{2\alpha-3}, \tag{2.76}$$

where c_{00} is the sound velocity at the center. Using ζ, x_{L} is written as

$$x_{\mathrm{L}} = \frac{\zeta}{\gamma(\gamma-1)\Lambda_0}\rho_{00}^{-1}c_{00}^{3-2\alpha}. \tag{2.77}$$

Substituting this equation into equation (2.75), one obtains

$$\mathcal{R} \sim \frac{C_{\mathrm{V}} f_v \zeta}{\gamma(\gamma-1)\Lambda_0 K_0} c_{00}^{4-2\alpha-\beta}, \tag{2.78}$$

where $U = f_v c_{00} (f_v < 1)$ and $K(T_{00}) = K_0 c_{00}^{\beta}$.

For the low temperature case, we adopt $K = 2.5 \times 10^3 \sqrt{T}$ ergs cm^{-1} K^{-1} s^{-1} (Parker, 1953) and the following cooling function (Koyama and Inutsuka, 2002);

$$\Lambda(T) \sim 1.0 \times 10^{20} \rho^2 \sqrt{T} \quad \mathrm{erg\ cm^{-3}\ s^{-1}}. \tag{2.79}$$

The Raynolds number is given by

$$\mathcal{R} \sim 84 \left(\frac{f_v}{0.1}\right)\left(\frac{\zeta}{0.1}\right)\left(\frac{T}{10^3 \mathrm{K}}\right). \tag{2.80}$$

We consider the self-similar solution describing isobaric condensation because the effect of the heat conduction is important for small scale. In the isobaric self-similar solution, the ratio $\zeta = x_{\mathrm{L}}/\lambda_{\mathrm{cool}}$ is less than 1 from figure 2.2. Here, we adopt $\zeta \sim 0.1$ as the representative value. From equation (2.80), since the Raynolds number is much larger than 1, dynamical condensation of the postshock region is expected to be well described by the self-similar solution. In previous section, the time evolution of the shocked gas can be described by the self-similar solution despite the heat conduction is taken account.

For the high temperature case, the cooling rate of metal lines (10^5K $< T <$ 10^7K) is given by

$$\Lambda(T) \sim 2.2 \times 10^{29} \rho^2 T^{-0.6} \quad \mathrm{ergs\ cm^{-3}\ s^{-1}}. \tag{2.81}$$

We adopt $K = 1.24 \times 10^{-6} T^{5/2}$ ergs cm^{-1} K^{-1} s^{-1} (Parker, 1953). Using this formula, the Raynolds number is given by

$$\mathcal{R} \sim 85 \left(\frac{f_v}{0.1}\right)\left(\frac{\zeta}{0.1}\right)\left(\frac{T}{10^6 \mathrm{K}}\right)^{0.1}. \tag{2.82}$$

Because of $\mathcal{R} \gg 1$, in the high temperature case, the self-similar solution is expected to well describe dynamical condensation.

As temperature decreases, $\mathcal{R}$ decreases and becomes < 1 at a certain epoch. Thereafter, our self-similar solutions are invalid and the effect of heat conduction becomes important during condensation.

2.4 Summary

In this chapter, we have presented new self-similar solutions describing dynamical condensation of cooling gas layers with the net cooling rate per unit mass, $\mathcal{L} \propto \rho T^{\alpha}$, where α is the index parameter. The results of our investigation are summarized as follows:

1. Our new self-similar solutions have one parameter η that ranges from 0 to 1 in addition to the index parameter α. The parameter, η relates with the ratio of the scale length of the condensing region $x_{\rm L}$ to the cooling length $\lambda_{\rm cool}$. The scale length of cooling layer of the self-similar solution for $\eta \sim 0$ is much larger than the cooling length, or $x_{\rm L} \gg \lambda_{\rm cool}$. In this solution, the density remains constant because $x_{\rm L}$ is too long for sound wave to travel during cooling. Therefore, the self-similar solution for $\eta \sim 0$ describes the isochorically cooling layer. The self-similar solutions for larger η have smaller scale length of the condensing region $x_{\rm L}$. Therefore, the gases interact more strongly each other within $x_{\rm L}$ for larger η. In the self-similar solution for $\eta \sim 1$, $x_{\rm L}$ is much smaller than $\lambda_{\rm cool}$. The fluid element evolves in pressure equilibrium with its surroundings because the sound wave can travel $x_{\rm L}$ many times during the cooling. The self-similar solution for $\eta \sim 1$ describes the isobarically condensing layer. Therefore, the family of the self-similar solutions describes nonlinear development of thermal instability of all length scales in one-dimensional model.

2. The self-similar solutions exist only for the range of $\alpha < 1$ where the gas is unstable in the isochoric and isobaric modes.

3. Derived self-similar solutions are compared with the results of numerical simulations for generic initial condition which is convergence flow in section 2.3.1. In any wavenumber of perturbation, our self-similar solutions well approximate the results of numerical simulations in high density limit. In the postshock region, smaller scale perturbation grows faster and asymptotically approaches to self-similar solutions for $\eta \sim 1$. There-

fore, in actual situations, the isobarically condensing self-similar solution ($\eta \sim 1$) is expected to be realized.

4. We investigate whether obtained self-similar solutions can describe the nonlinear development of the runaway condensation of the gas layer induced by the colliding WNM that is calculated in section 1.7 by the one-dimensional numerical simulation. It is found that this condensation is well described by the self-similar solution for $\eta \sim 1$ that describes the isobarically condensing layer.

Chapter 3

Linear Analysis of Self-Similar Solutions

In chapter 2, we have discovered new self-similar solutions that describe nonlinear time evolution of cooling layers in one-dimensional simulations well. However, in order to examine the size and shape distributions of condensed cold clouds, it is important to investigate multi-dimensional evolution of the condensing layer. In this chapter, we investigate linear stability of the obtained self-similar solutions against fluctuations in the direction perpendicular, as well as parallel, to the condensation. This analysis provides some insight about the size of the cold clouds.

This chapter is mainly based on our paper, Iwasaki and Tsuribe (2009).

3.1 Formulation

We take the x-axis as the direction of the condensation driven by the cooling and y-axis as the transverse direction. Since the self-similar solutions are time-dependent, it is difficult to perform linear analysis in the ordinary Cartesian coordinate, (t, x, y). Bouquet et al. (1985) introduced a zooming coordinate where self-similar solutions appear to be stationary (also see Hanawa and Matsumoto, 1999). We introduce the similar zooming coordinate since this transformation makes stability analysis easier as follows:

$$\begin{pmatrix} t \\ x \\ y \end{pmatrix} \Rightarrow \begin{pmatrix} \tau \\ \xi \\ y \end{pmatrix} = \begin{pmatrix} -\dfrac{\ln(1-t/t_{\rm c})}{1-\omega} \\ x/\lambda_{\rm cool}(t) \\ y \end{pmatrix}, \quad \lambda_{\rm cool}(t) = \lambda_{\rm cool}(t=0)(1-t/t_{\rm c})^{1/(1-\omega)}, \tag{3.1}$$

where ω is the free parameter and $t_{\rm c}$ is an epoch when the central density becomes infinity. In the zooming coordinate, density Ω, velocity $\vec{V}$, pressure Π, and sound speed X are given by

$$\Omega(\tau,\xi,y) = \rho(t,x,y)/\rho_0(t), \qquad \vec{V}(\tau,\xi,y) = \vec{v}(t,x,y)/v_0(t),$$

$$\Pi(\tau,\xi,y) = P(t,x,y)/P_0(t), \qquad X(\tau,\xi,y) = c_{\rm s}(t,x,y)/v_0(t), \tag{3.2}$$

respectively, where definitions of $\rho_0(t)$, $v_0(t)$, and $P_0(t)$ are given in equation (2.64). In the zooming coordinate, the basic equations (2.2)-(2.4) are rewritten as

$$\frac{{\rm D}\ln\Omega}{{\rm D}\tau} + \vec{\nabla}\cdot\vec{V} = \beta, \tag{3.3}$$

$$\frac{{\rm D}\vec{V}}{{\rm D}\tau} + \frac{1}{\Omega}\vec{\nabla}\Pi = \omega\vec{V}, \tag{3.4}$$

and

$$\frac{1}{\gamma-1}\frac{\rm D}{{\rm D}\tau}\left(\ln\Pi\Omega^{-\gamma}\right) = \frac{2\omega}{\gamma-1} - \beta - \gamma^{\alpha}\Omega^{2-\alpha}\Pi^{\alpha-1}, \tag{3.5}$$

respectively, where the operators of time and spatial derivative are defined by

$$\frac{\rm D}{{\rm D}\tau} = \frac{\partial}{\partial\tau} + (\vec{V}+\xi\vec{e}_{\xi})\cdot\vec{\nabla}, \quad \text{and} \quad \vec{\nabla} = \left(\frac{\partial}{\partial\xi}, \lambda_{\rm cool}(\tau)\frac{\partial}{\partial y}\right), \tag{3.6}$$

respectively, where $\vec{e}_{\xi}$ indicates the unit vector parallel to the ξ-direction. The derivation of equations (3.3)-(3.5) is presented in Appendix C. Stationary solutions, $\partial/\partial\tau = \hat{0}$, are identical to self-similar solutions obtained in chapter 2.

We apply the zooming transformation only in the x-direction but not in the y-direction in equation (3.1). This is because the gas contracts along the x-axis but not along the y-axis in the unperturbed state. In the ordinary coordinate, the transverse scale of the perturbation is expected to be constant with time. However, if the zooming transformation is also applied in the y-direction, the transverse scale of the perturbation decreases with time in the ordinary coordinate, although the unperturbed gas does not contract along the y-axis. Therefore, we apply the zooming transformation only in the x-direction.

3.1.1 Perturbation Equations

Perturbation on the self-similar solutions is considered. Perturbed variables are defined by

$$\begin{aligned}\Omega &= \Omega_0(\xi)\{1+\delta\Omega(\tau,\xi,y)\},\\ V_x &= V_0(\xi)+\delta V_x(\tau,\xi,y),\\ V_y &= \delta V_y(\tau,\xi,y),\end{aligned}$$

and

$$\Pi = \Pi_0(\xi)\{1+\delta\Pi(\tau,\xi,y)\}, \tag{3.7}$$

where subscript "0" indicates the unperturbed state. We consider the following Fourier mode with respect to y,

$$\delta\vec{Q}(\tau,\xi,y) = \delta\vec{Q}(\tau,\xi)\exp(iky), \quad \text{where } \delta\vec{Q} = (\delta\Omega, \delta\vec{V}, \delta\Pi), \tag{3.8}$$

and k indicates the wavenumber of the plane wave that propagates along the y-direction. Substituting equations (3.7) and (3.8) into equations (3.3)-(3.5) and linearizing, we get the following perturbation equations:

$$\frac{\mathrm{D}\delta\Omega}{\mathrm{D}\tau} + \frac{\partial\delta V_x}{\partial\xi} = -(\ln\Omega_0)'\delta V_x - k\lambda_{\mathrm{cool}}(\tau)i\delta V_y, \tag{3.9}$$

$$\frac{\mathrm{D}\delta V_x}{\mathrm{D}\tau} + \frac{X_0^2}{\gamma}\frac{\partial\delta\Pi}{\partial\xi} = (\omega - V_0')\delta V_x - \frac{X_0^2}{\gamma}(\ln\Pi_0)'(\delta\Pi - \delta\Omega), \tag{3.10}$$

$$\frac{\mathrm{D}i\delta V_y}{\mathrm{D}\tau} = \omega i\delta V_y + k\lambda_{\mathrm{cool}}(\tau)\frac{X_0^2}{\gamma}\delta\Pi, \tag{3.11}$$

and

$$\frac{\mathrm{D}\delta\Pi}{\mathrm{D}\tau} - \gamma\frac{\mathrm{D}\delta\Omega}{\mathrm{D}\tau} = -(2-\alpha)\gamma\epsilon_0\delta\Omega - (\alpha-1)\gamma\epsilon_0\delta\Pi - (\ln\Pi_0\Omega_0^{-\gamma})'\delta V_x, \tag{3.12}$$

where $\mathrm{D}/\mathrm{D}\tau = \partial/\partial\tau + V_0\partial/\partial\xi$,

$$\epsilon_0 = \gamma^{\alpha-1}(\gamma-1)\Omega_0^{2-\alpha}\Pi_0^{\alpha-1}, \quad \text{and } k\lambda_{\mathrm{cool}}(\tau) \equiv k\lambda_{\mathrm{cool}}(\tau). \tag{3.13}$$

The time-dependent factors remain in the form of $k\lambda_{\mathrm{cool}}(\tau)$ in (3.9)-(3.12) because the transverse scale is not zoomed (see equation (3.1)) as mentioned above. This leads to a problem that the perturbed variables cannot be expanded in the Fourier mode with respect to τ in general.

3.2 Perturbation with $k = 0$

In this section, we consider the perturbation parallel to the condensation, or for the case with $k = 0$. In this case, since the time-dependent factor, $k\lambda_{\rm cool}(\tau)$, vanishes, the perturbed variables can be expanded in the Fourier mode with respect to τ as

$$\delta Q(\tau, \xi, y) = \delta Q(\xi) \exp\left\{(1-\omega)\Sigma\tau + iky\right\}. \tag{3.14}$$

By equation (3.14), the time evolution of the perturbations is given by

$$\delta Q \propto (1 - t/t_{\rm c})^{-\Sigma}. \tag{3.15}$$

If Σ is positive value, the perturbation is unstable. Substituting equation (3.14) into the perturbation equations (3.9)-(3.12), one obtains the following ordinary differential equations:

$$\frac{{\rm d}\delta Q_i}{{\rm d}\xi} = \frac{1}{V_0^2 - X_0^2}\sum_{j=1}^{3} A_{ij}\delta Q_j, \quad \delta\vec{Q} = (\delta\Omega, \delta V_x, \delta\Pi), \tag{3.16}$$

where the detailed expression of A_{ij} is shown in Appendix D. Equations (3.16) are solved as a boundary- and eigen-value problem.

3.2.1 Boundary Conditions

We impose the boundary conditions at $\xi = 0$ and at the critical point, $\xi = \xi_{\rm s}$, where $V_0 = X_0$. The boundary conditions at $\xi = 0$ are obtained by the asymptotic limit of the perturbed variables. From the regularity of the perturbed variables at $\xi = 0$, we find that perturbed variables should have the following asymptotic forms:

$$\lim_{\xi\to 0}\delta\Omega(\xi) \simeq \delta\Omega_0, \quad \lim_{\xi\to 0}\delta V_x(\xi) \simeq -(1-\omega)\Sigma\delta\Omega_0\xi, \tag{3.17}$$

and

$$\lim_{\xi\to 0}\delta\Pi(\xi) \simeq \gamma\frac{(1-\omega)\Sigma + (\alpha-2)\epsilon_{00}}{(1-\omega)\Sigma + (\alpha-1)\gamma\epsilon_{00}}\delta\Omega_0, \tag{3.18}$$

where $\epsilon_{00} = \{2\omega - \beta(\gamma-1)\}/\gamma$

The boundary conditions at the critical point, $\xi = \xi_{\rm s}$, are obtained from the equations (3.16). At $\xi = \xi_{\rm s}$, the denominator of the righthand side becomes zero. To obtain a regular solution from $\xi = 0$ to $\xi = \infty$, the numerator of the righthand side should vanish. Therefore, the boundary conditions are given by the following three equations,

$$\left.\sum_{j=1}^{3} A_{ij}\delta Q_j\right|_{\xi=\xi_{\rm s}} = 0, \quad i = 1, 2, 3. \tag{3.19}$$

The above three equations give only one independent condition.

3.2.2 Numerical Method

Solutions of equations (3.16) have three integration constants. Therefore, if we set two constants $(\delta\Omega_0, \Sigma)$ and impose the boundary condition at $\xi = \xi_{\rm s}$, the solution is completely fixed. In this section, our numerical method for solving equations (3.16) is described.

We can set $\delta\Omega_0 = 1$ without loss of generality. For a given Σ, we integrate equations (3.16) from $\xi = 0$ to the critical point, $\xi = \xi_{\rm s}$, using a fourth-order Runge-Kutta method. Eigenvalue, Σ, is modified until the perturbed variables satisfy the boundary condition at $\xi = \xi_{\rm s}$ using the Newton-Raphson method. After that, we integrate equations (3.16) up to $\xi = 10^4$.

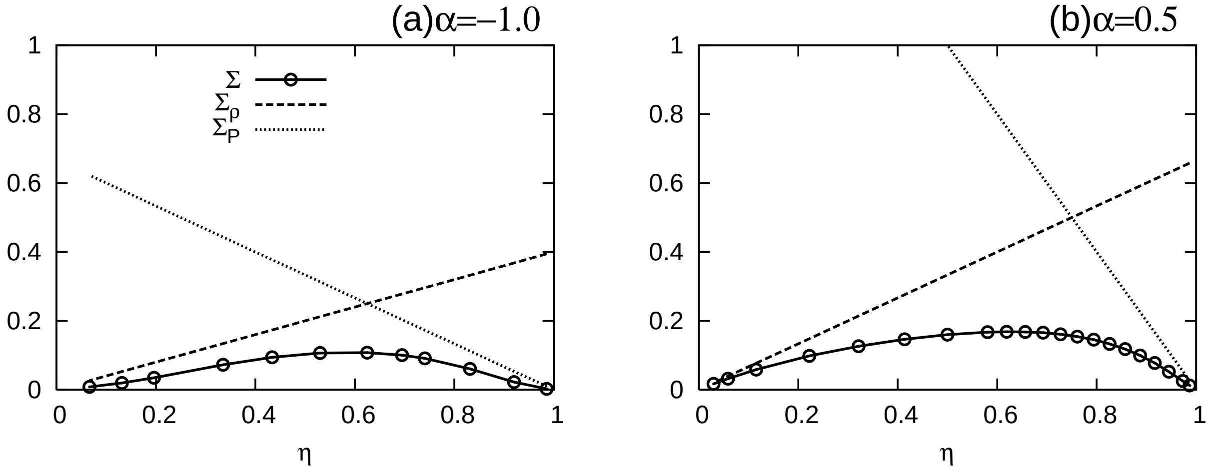

Figure 3.1: Growth rate, Σ, as a function of η for (a) $\alpha = -1.0$ and (b) 0.5 for the case with the perturbation parallel to the condensation. For comparison, the increasing rate of the unperturbed central density, Σ_ρ, and the decreasing rate of the unperturbed central pressure, Σ_P, are shown by the dashed and dotted lines, respectively.

3.2.3 Results

Figure 3.1 shows the dependence of the growth rate, Σ, on the parameter η for (a)$\alpha = -1.0$ and (b)0.5. From Figure 3.1, it is seen that $\Sigma > 0$ for a wide range of α and η. Therefore, the perturbation is unstable. We compare the growth rate Σ with the evolutionary rates of

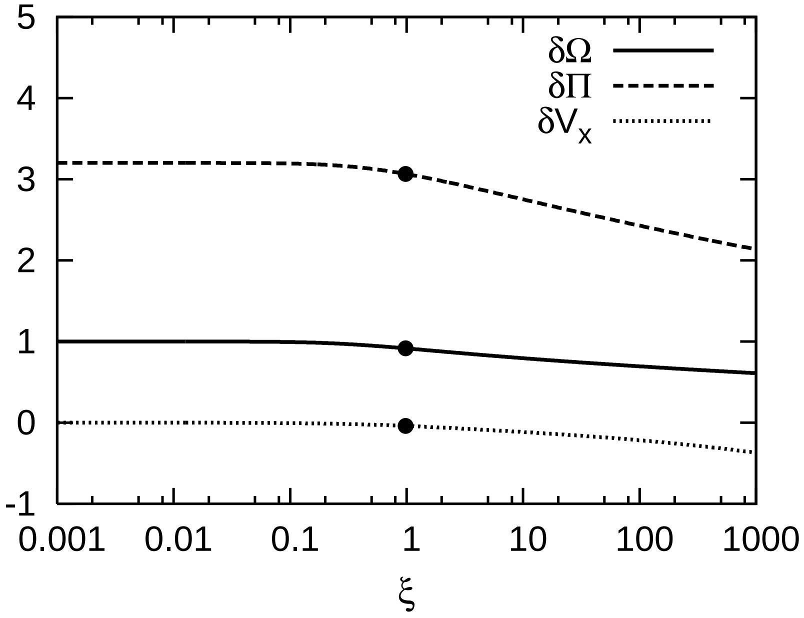

Figure 3.2: Eigenfunctions of the dimensionless density perturbation $\delta\Omega$(the solid line), pressure perturbation $\delta\Pi$(the long-dashed line), velocity perturbation δV_x(the dotted line) for the parameter $\eta = 0.917$. The index parameter of the net cooling rate α is set to 0.5. The filled circles denote the values at the critical point. The corresponding growth rate is $\Sigma = 7.76 \times 10^{-2}$.

the central density and pressure that are defined by

$$\Sigma_\rho = \left| \frac{\partial \ln \rho_{00}}{\partial \ln(1 - t/t_\mathrm{c})} \right| = \frac{\eta}{2-\alpha}, \quad \text{and} \quad \Sigma_P = \left| \frac{\partial \ln P_{00}}{\partial \ln(1 - t/t_\mathrm{c})} \right| = \frac{1-\eta}{1-\alpha}, \tag{3.20}$$

respectively (see equation (2.51)). Figure 3.1 shows that Σ is smaller than Σ_ρ and Σ_P for all η. Therefore, the growth rate is too low to grow sufficiently during the runaway condensation. This is consistent with the results of the one-dimensional numerical simulation shown in section 2.3. Figure 3.2 shows eigenfunctions of $(\delta\Omega, \delta\Pi, \delta V_x)$ for $\alpha = 0.5$ and $\eta = 0.917$. The filled circles denote the values at the critical point. The corresponding growth rate is $\Sigma = 7.76 \times 10^{-2}$. In normal thermal instability presented in Field (1965); Koyama and Inutsuka (2000), the pressure perturbation has opposite sign of the density perturbation. Therefore, as the gas condenses, the pressure drops. Therefore, the pressure gradient promotes the condensation. However, in this case, the sign of $\delta\Pi$ is the same as that of $\delta\Omega$. Moreover, figure 3.2 shows that the density perturbation is smaller than the pressure perturbation. As the gas condenses, the pressure gradient tends to prevent the condensation. This is one possible reason that the growth rate is very small.

3.3 Perturbation with $k \neq 0$

3.3.1 Static Approximation

Before we present the fully time-dependent numerical calculation in section 3.3.2, we at first consider a special case in which the time evolutions of the unperturbed self-similar solutions are slower than the growth of perturbation. In this situation, the time evolution of the unperturbed state is negligible during the growth of the perturbations. Therefore, we set $\lambda_{\mathrm{cool}}(t)$ to be a constant in equations (3.9)-(3.12). This approximation is also valid for $k \ll 1/\lambda_{\mathrm{cool}}$ where the term, $k\lambda_{\mathrm{cool}}$, is negligibly small in equations (3.9)-(3.12). We use the Fourier mode as

$$\delta\vec{Q}(\xi, y, \tau) = \delta\vec{Q}(\xi)\exp\left\{iky + (1-\omega)\Sigma\tau\right\}, \quad \delta\vec{Q} = (\delta\Omega, \delta V_x, \delta\Pi, i\delta V_y). \tag{3.21}$$

The condition under which the static approximation is valid is given by

$$\begin{aligned} \left|\frac{\mathrm{d}\ln\delta Q}{\mathrm{d}\ln(1-t/t_{\mathrm{c}})}\right| = \Sigma \gg \left|\frac{\mathrm{d}\ln k\lambda_{\mathrm{cool}}}{\mathrm{d}\ln(1-t/t_{\mathrm{c}})}\right| &= \frac{(2-\alpha)(3-2\alpha)-\eta}{2(2-\alpha)(1-\alpha)}, \\ &= \left\{ \begin{array}{ll} \dfrac{5-2\alpha}{2(2-\alpha)} & \text{for } \eta = 1 \\ \dfrac{3-2\alpha}{2(1-\alpha)} & \text{for } \eta = 0 \end{array} \right. , \end{aligned} \tag{3.22}$$

where the definition of Σ is the same as that in equation (3.15). Substituting equation (3.21) into the perturbation equations (3.9)-(3.12), we get

$$\frac{\mathrm{d}\delta Q_i}{\mathrm{d}\xi} = \frac{1}{V_0^2 - X_0^2}\sum_{j=1}^{4} A_{ij}\delta Q_j, \quad \delta\vec{Q} = (\delta\Omega, \delta V_x, \delta\Pi, i\delta V_y), \tag{3.23}$$

where the detailed expression of A_{ij} is shown in Appendix D.

We impose the boundary conditions at $\xi = 0$ and $\xi = \xi_{\mathrm{s}}$. Since we are interested in the fragmentation of the cooling layer, only the even mode is investigated. For the even mode, the perturbed variable should have the following asymptotic forms in $\xi \ll 1$:

$$\begin{aligned} \lim_{\xi\to 0}\delta\Omega(\xi) &\simeq \delta\Omega_0, \\ \lim_{\xi\to 0}\delta V_x(\xi) &\simeq \delta V_{x0}\xi, \\ \lim_{\xi\to 0}\delta V_y(\xi) &\simeq \delta V_{y0}, \\ &\text{and} \\ \lim_{\xi\to 0}\delta\Pi(\xi) &\simeq \delta\Pi_0 + \delta\Pi_{01}\xi^2. \end{aligned} \tag{3.24}$$

Substituting equations (3.24) into equations (3.23), we obtain the following relations:

$$(1-\omega)\Sigma\Omega_0 + \delta V_{x0} + k\lambda_{\rm cool} i\delta V_{y0} = 0, \tag{3.25}$$

$$\{(1-\omega)\Sigma - \omega\}\, i\delta V_{y0} = \frac{k\lambda_{\rm cool}X_{00}^2}{\gamma}\delta\Pi_0, \tag{3.26}$$

$$\{(1-\omega)\Sigma + (\alpha-2)\epsilon_{00}\}\,\gamma\delta\Omega_0 - \{(1-\omega)\Sigma + (\alpha-1)\gamma\epsilon_{00}\}\,\delta\Pi_0 = 0, \tag{3.27}$$

and

$$\{2\beta + 1 - \omega + (1-\omega)\Sigma\}\,\delta V_{x0} + 2\frac{X_{00}^2}{\gamma}\delta\Pi_{01} = 2\beta\omega(1-\alpha)(\delta\Pi_0 - \delta\Omega_0). \tag{3.28}$$

The boundary condition at $\xi = \xi_{\rm s}$ is derived in the same way in section 3.2.1, and we obtain two independent conditions. Numerical method for solving equations (3.23) is the same as that in section 3.2.2.

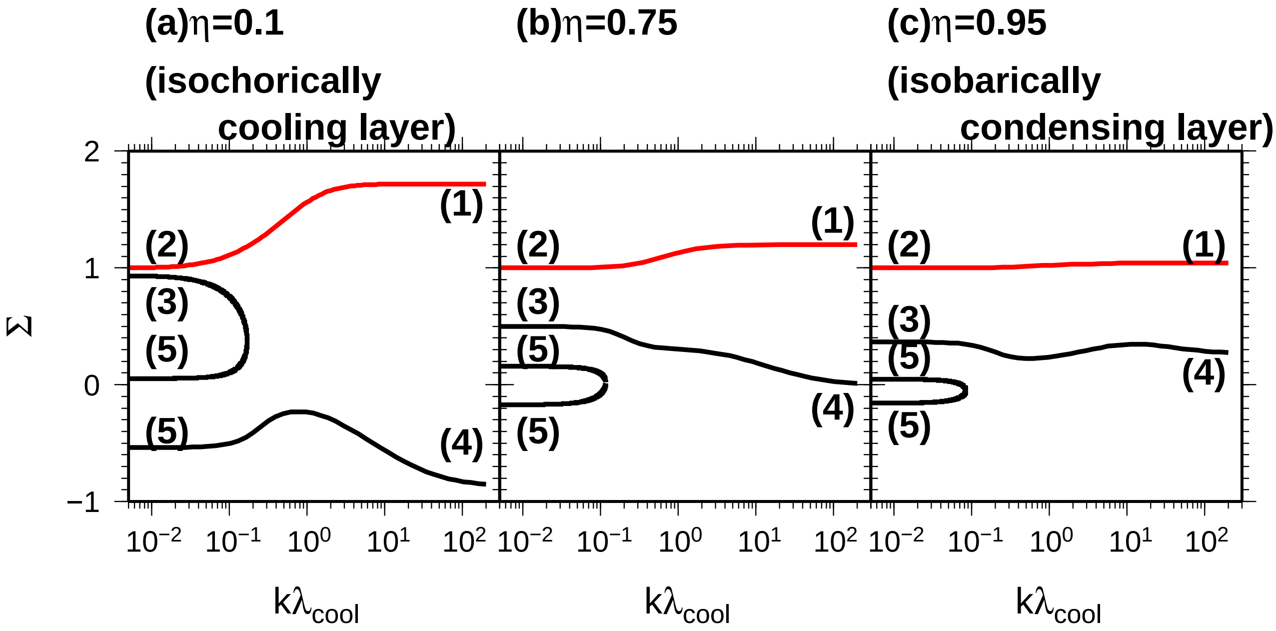

Figure 3.3: Approximate dispersion relations for (a) $\eta = 0.1$, (b) 0.75, and (c) 0.95, where $k\lambda_{\rm cool}$ is the nondimensional wavenumber, and Σ is the growth rate. The labels of number represent the branches of modes. The red lines indicates the most unstable branches.

Figures 3.3 shows approximate dispersion relations for (a)$\eta = 0.1$, (b) 0.75, and (c) 0.95. The index parameter of the net cooling rate α is set to 0.5. The self-similar solutions for $\eta = 0.10$ and $\eta = 0.95$ describe the isochorically cooling layer and the isobarically condensing layer, respectively. In Figure 3.3, one can see several branches labelled by numbers. The most unstable branch is labelled by (1) for large $k\lambda_{\rm cool}$ limit, and (2) for small $k\lambda_{\rm cool}$ limit that is shown by the red line. Each branch is explained below.

(1) The isobaric mode

The branch (1) corresponds to the most unstable mode for $k\lambda_{\rm cool} \gg 1$. Since $1/k \ll \lambda_{\rm cool}$, the sound wave can travel the wavelength of the perturbation many times during the runaway cooling of the unperturbed state. Therefore, the perturbation is expected to grow in pressure equilibrium with its surroundings, and the mode corresponds to the isobaric mode. Eigenfunctions of $(\delta\Omega, \delta\Pi, \delta V_x, \delta V_y)$ for the branch (1) are shown in figure 3.4a for ($\eta = 0.97$, $k\lambda_{\rm cool} = 4.0$) and figure 3.5a for ($\eta = 0.22$, $k\lambda_{\rm cool} = 6.0$). In both figures 3.4a and 3.5a, it is clearly seen that $|\delta\Pi| \ll |\delta\Omega|$. This also implies the isobaric mode.

The growth rate in the isobaric mode can also be derived analytically by considering the evolution of a fluid element at the center. The fluid element is assumed to have an isobaric fluctuation, $\rho = \rho_{00}(t) + \delta\rho_{00}$ and $P = P_{00}(t)$. Linearizing equation (2.4), we obtain the following perturbation equation,

$$\frac{\partial}{\partial t}\left(\frac{\delta\rho_{00}}{\rho_{00}}\right) = (2-\alpha)\gamma^{\alpha-1}(\gamma-1)\Lambda_0\rho_{00}^{2-\alpha}P_{00}^{\alpha-1}\frac{\delta\rho_{00}}{\rho_{00}}. \tag{3.29}$$

From equations (2.13) and (2.64), we have

$$\gamma^{\alpha-1}(\gamma-1)\Lambda_0\rho_{00}^{2-\alpha}P_{00}^{\alpha-1} = \frac{\epsilon_{00}}{(1-\omega)(t_{\rm c}-t)}. \tag{3.30}$$

Using equation (3.30), equation (3.29) is rewritten as

$$\frac{\partial}{\partial t}\left(\frac{\delta\rho_{00}}{\rho_{00}}\right) = \frac{(2-\alpha)\epsilon_{00}}{(1-\omega)(t_{\rm c}-t)}\frac{\delta\rho_{00}}{\rho_{00}}. \tag{3.31}$$

Equation (3.31) can be integrated to give

$$\frac{\delta\rho_{00}}{\rho_{00}} \propto \left(1-\frac{t}{t_{\rm c}}\right)^{-(2-\alpha)\epsilon_{00}/(1-\omega)}. \tag{3.32}$$

Therefore, the growth rate in isobaric mode is given by

$$\begin{aligned}\Sigma_{\rm isobaric} &= \frac{(2-\alpha)\epsilon_{00}}{1-\omega} \\ &= \left[1-\frac{2-\alpha}{\gamma(1-\alpha)}\right]\eta + \frac{2-\alpha}{\gamma(1-\alpha)} = \begin{cases} 1.72 & \text{for } \eta = 0.10 \\ 1.20 & \text{for } \eta = 0.75 \\ 1.04 & \text{for } \eta = 0.95 \end{cases}.\end{aligned} \tag{3.33}$$

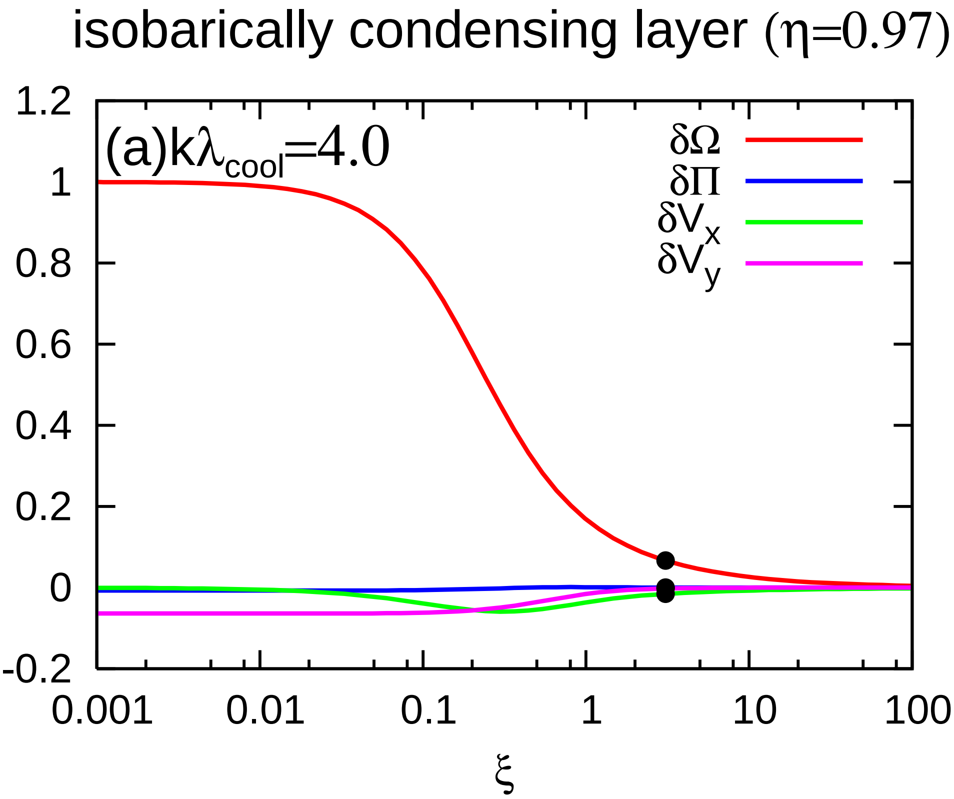

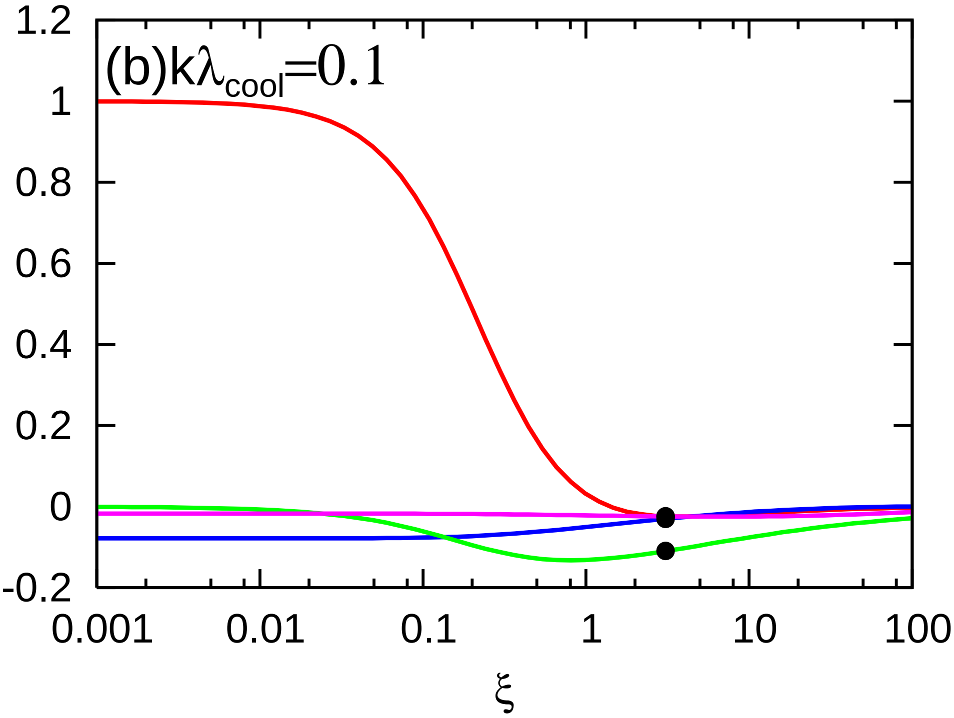

Figure 3.4: Results of the linear analysis of the isobarically condensing layer ($\eta = 0.97$) for the wavenumbers (a)$k\lambda_{\rm cool} = 4.0$ and (b)0.1. The red, blue, green and magenta lines indicate eigenfunctions of the dimensionless density perturbation $\delta\Omega$, pressure perturbation $\delta\Pi$, velocity perturbation in the x direction δV_x, and velocity perturbation in the y-direction δV_y, respectively. The filled circles indicate the values at the critical point.

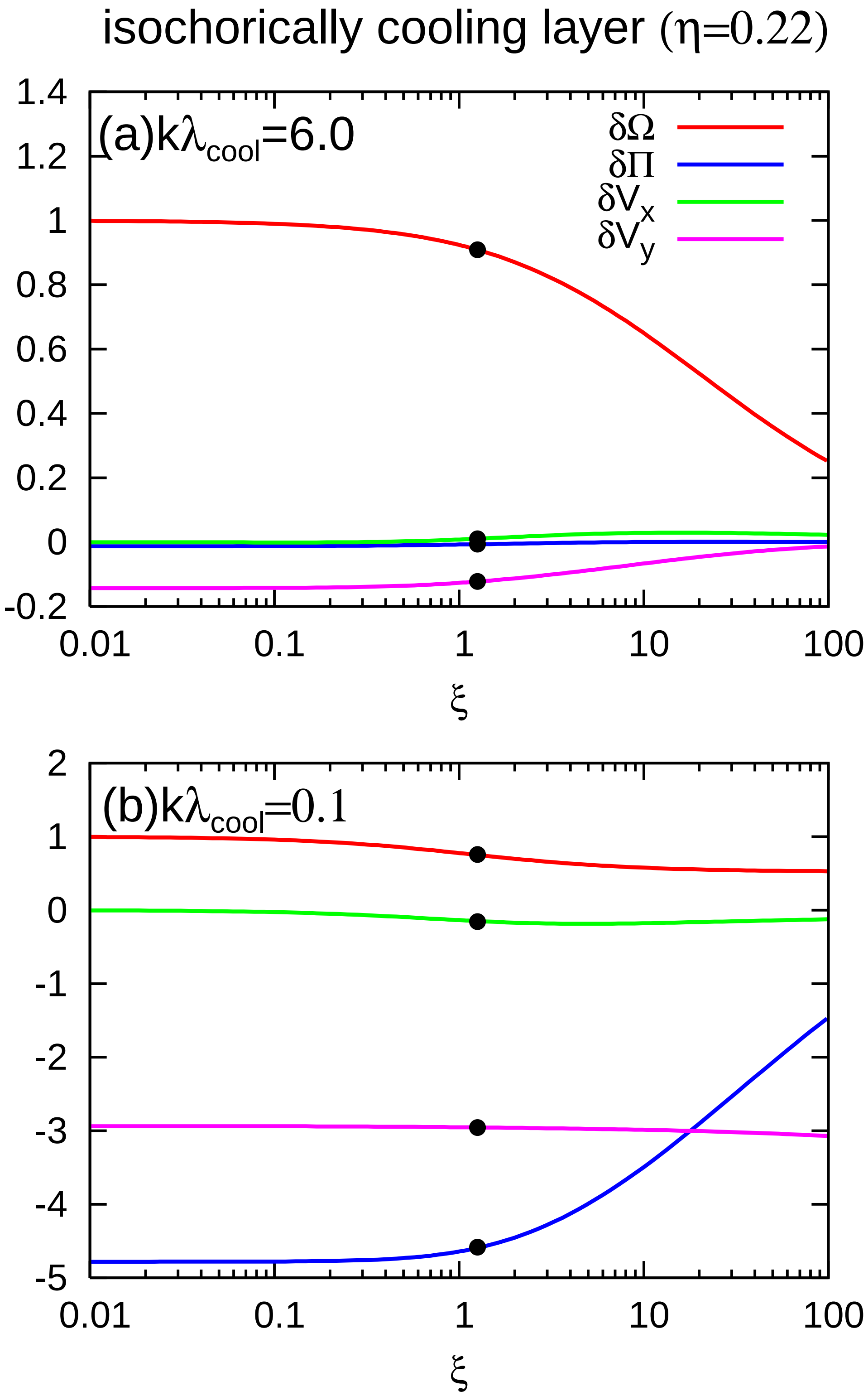

Figure 3.5: Results of the linear analysis of the isochorically cooling layer ($\eta = 0.22$) for the wavenumbers (a)$k\lambda_{\rm cool} = 6.0$ and (b)0.1. The definition of the lines and symbols are the same as figure 3.4.

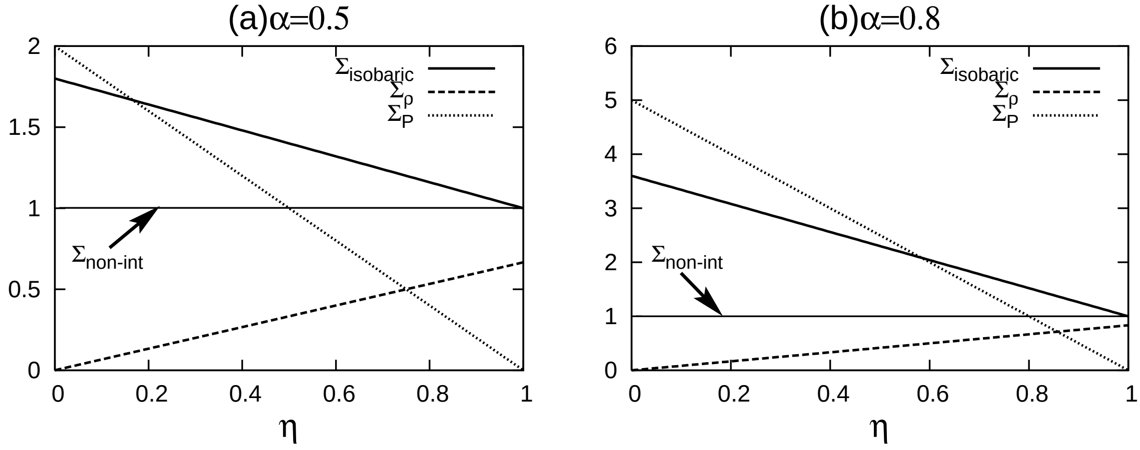

Figure 3.6: Growth rate as a function of η for (a)$\alpha = 0.5$ and (b)0.8 for the case with $k \neq 0$. The thick solid lines correspond to the growth rate of the isobaric mode, $\Sigma_{\rm isobaric}$. For comparison, the evolutionary rate of the unperturbed central density, Σ_ρ, and pressure, Σ_P are shown by the dashed and dotted lines, respectively. The thin solid lines pointed by arrows correspond to the growth rate in the noninteractive mode, $\Sigma_{\rm non-int}$.

For the isochorically cooling layer ($\eta \sim 0$), the growth rate of the isobaric mode becomes

$$\Sigma_{\rm isobaric}(\eta = 0) = \frac{2-\alpha}{\gamma(1-\alpha)}. \tag{3.34}$$

For the isobarically condensing layer ($\eta \sim 1$), the growth rate of the isobaric mode becomes

$$\Sigma_{\rm isobaric}(\eta = 1) = 1. \tag{3.35}$$

From figure 3.3, it is clearly seen that the growth rate approaches the corresponding $\Sigma_{\rm isobaric}$ in the large $k\lambda_{\rm cool}$ limit. Since the analytic growth rate is derived by the local argument, the growth rate is expected to be independent of a global structure of the system. Burkert and Lin (2000) performed a linear analysis on a spatially uniform and isochorically cooling gas. Their growth rate in the isobaric mode is the same as equation (3.34), although the spatial structure of the unperturbed state is quite different.

In order for the density perturbation to grow sufficiently during the runaway cooling, it must grow faster than the condensation of the cooling layer. This condition can be expressed by $\Sigma_{\rm isobaric} > \Sigma_\rho$. Figure 3.6 shows $\Sigma_{\rm isobaric}$, Σ_ρ and Σ_P as a function of η for (a)$\alpha = 0.5$ and (b)0.8. From figure 3.6, it is found that $\Sigma_{\rm isobaric}$ is greater than Σ_ρ for all η. For other α, we can investigate analytically as follows: subtracting Σ_ρ from $\Sigma_{\rm isobaric}$, one obtains

$$\begin{aligned}\Sigma_{\rm isobaric} - \Sigma_\rho &= \left[1 - \frac{2-\alpha}{\gamma(1-\alpha)} - \frac{1}{2-\alpha}\right]\eta + \frac{2-\alpha}{\gamma(1-\alpha)} \\ &\geq 1 - \frac{1}{2-\alpha} > 0 \ \ \text{for} \ \ \alpha < 1. \end{aligned} \tag{3.36}$$

Therefore, for $\alpha < 1$, $\Sigma_{\rm isobaric}$ is larger than Σ_ρ, and the isobaric mode can grow in the layer.

(2) The noninteractive mode

Branch (2) corresponds to the most unstable mode for $k\lambda_{\rm cool} \ll 1$. Because the wavelength is larger than the cooling length, each part evolves independently according to the self-similar solutions. We call this branch the noninteractive mode. Figure 3.7 shows the schematic picture of the noninteractive mode. In figure 3.7, similarity variables have an initial fluctuation. For example, we consider two different regions, "A" and "B", where $\rho_{\rm A} = \rho + \Delta\rho$ and $\rho_{\rm B} = \rho$. Due to the difference of the density, the regions "A" and "B" have different collapse times, $t_{\rm c} - \Delta t$ and $t_{\rm c}$, respectively. Omitting any terms that do not grow, we find the time evolution of difference, $\Delta\rho$, to be

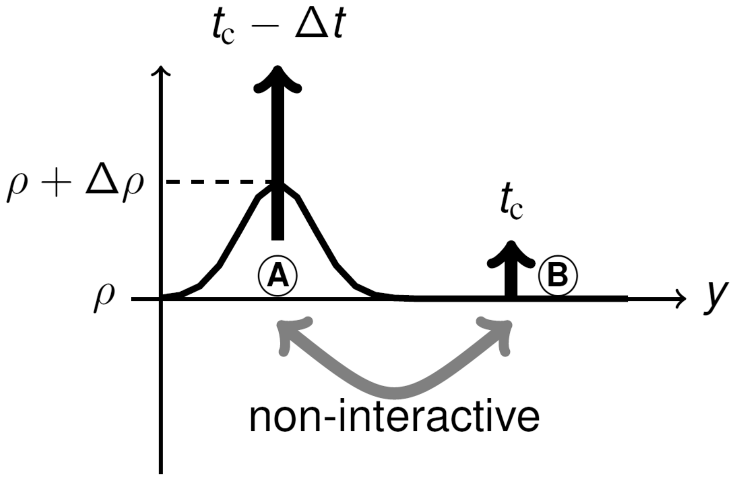

Figure 3.7: Schematic picture of the noninteractive mode.

$$\frac{\Delta\rho}{\rho_0(t)} = -\Omega_0(\xi)\Delta t\left[\Sigma_\rho + \frac{1}{1-\omega}\frac{{\rm d}\ln\Omega_0}{{\rm d}\ln\xi}\right]\frac{1}{t_{\rm c}-t}. \tag{3.37}$$

Therefore, in the zooming coordinate, the density perturbation grows as $\delta\Omega \propto (t_{\rm c} - t)^{-1}$. Other perturbed variables also grow in the same power law. Therefore, comparing with equation (3.15), the growth rate is given by

$$\Sigma_{\rm non-int} = 1, \tag{3.38}$$

which is independent of the parameters α and η. Figures 3.4b and 3.5b show eigenfunctions of $(\delta\Omega, \delta\Pi, \delta V_x, \delta V_y)$ for the noninteractive mode for ($\eta = 0.97$, $k\lambda_{\rm cool} = 0.1$) and ($\eta = 0.22$, $k\lambda_{\rm cool} = 0.1$), respectively. Figure 3.4b shows that $|\delta\Omega| \gg |\delta\Pi|$ for $\eta = 0.97$. Therefore, the noninteractive mode in the isobarically condensing layers grows like the isobaric mode. On the other hand, figure 3.5b shows that $|\delta\Omega| \ll |\delta\Pi|$ for $\eta = 0.22$. Therefore, the noninteractive mode in the isochorically cooling layers grows like the isochoric mode. This can be understood as follows: the noninteractive mode arises from the fluctuation of the collapse time, $t_{\rm c}$, due to the density and pressure perturbations. Therfore, from the physical mechanism, the perturbation grows in the same way as the unperturbed state. In other words, the perturbation of the isobarically (isochorically) cooling layer grows isobarically (isochorically).

We investigate whether the noninteractive mode grows sufficiently during the runaway cooling or not. First, we consider the case with $\eta > \eta_{\rm eq}$. Since the perturbation grows isobarically, $\Sigma_{\rm non-int}$ is compared to $\Sigma_\rho = \eta/(2-\alpha)$. From figure 3.6, it is seen that the growth rate, $\Sigma_{\rm non-int}$, is higher than Σ_ρ for all $\eta > \eta_{\rm eq} = 0.75$ and 0.86 for $\alpha = 0.5$ and 0.8, respectively. Therefore, the noninteractive mode can grow sufficiently. Next, we consider the cooling layer with $\eta < \eta_{\rm eq}$. In this layer, since the perturbation grows isochorically, $\Sigma_{\rm non-int}$ is compared to $\Sigma_P = (1-\eta)/(1-\alpha)$. Analytically, it is found that the pressure perturbation can only grow for $\eta > \alpha$.

Koyama and Inutsuka (2000) performed a linear analysis of a spatially uniform and isobarically cooling gas in their appendix. However, they did not find the noninteractive mode. This is because they fixed the collapse time to be spatially constant, and it was assumed not to be influenced by perturbation. Burkert and Lin (2000) performed linear analysis of a spatially uniform and isochorically cooling gas by taking account of the time evolution of the unperturbed state. They showed that a perturbation cannot grow in the condition for long wavelength limit. Our result is consistent with theirs.

(3) The shear mode

For $k\lambda_{\rm cool} \ll 0$, there is a solution where physical variables are very small except for

δV_y which is spatially constant, and the eigenvalue is $\Sigma = \omega/(1-\omega)$. The similar mode was found by McNamara (1993), who investigated thermal instability of a uniform granular medium. McNamara (1993) called this mode the shear mode. The growth rate is given by

$$\Sigma_{\text{shear}} = \frac{\omega}{1-\omega} = \frac{2(2-\alpha)(1-\alpha)}{(2-\alpha)(3-2\alpha)-\eta} = \begin{cases} 0.93 & \text{for } \eta = 0.10 \\ 0.50 & \text{for } \eta = 0.75 \\ 0.37 & \text{for } \eta = 0.95 \end{cases} . \tag{3.39}$$

In figure 3.3, it is seen that each growth rate in branch (3) has the corresponding value of Σ_{shear} for $k\lambda_{\text{cool}} \ll 1$. The physical meaning of this mode can be understood as follows: for $k\lambda_{\text{cool}} \ll 1$, since the effect of the pressure gradient with respect to y is very weak, the gas can freely stream with almost constant velocity, v_y, in the y direction. On the other hand, the central sound speed, $c_{00}(t)$, decreases as $\propto (t_{\text{c}} - t)^{\omega/(1-\omega)}$. Therefore, the ratio of the dynamical velocity to the thermal velocity, $v_y/c_{00}(t)$, grows with time as $\propto (t_{\text{c}} - t)^{-\omega/(1-\omega)}$, indicating that the growth rate is given by equation (3.39). For the case with larger wavenumber, the effect of the pressure gradient becomes important. Therefore, the fluid element cannot stream freely, and the growth rate is lower as shown in figure 3.3.

(4) The free-streaming mode

For large $k\lambda_{\text{cool}}$, there is another mode in which the velocity perturbation in the x-direction is much greater than that in the y-direction, $|\delta V_{x0}| \gg |\delta V_{y0}|$. We call this mode the free-streaming mode. From equation (3.28) with $\delta\Omega_0 = \delta\Pi_0 = \delta\Pi_{01} = 0$, we obtain

$$\Sigma_{\text{free}} = -1 - \frac{2\beta}{1-\omega} = -1 + \frac{2}{2-\alpha}\eta = \begin{cases} -0.87 & \text{for } \eta = 0.10 \\ 0.00 & \text{for } \eta = 0.75 \\ 0.27 & \text{for } \eta = 0.95 \end{cases} . \tag{3.40}$$

In the free-streaming mode, the growth of the velocity perturbation in the x-direction is hampered by the pressure gradient of the unperturbed state. Therefore, the growth rate is less than the shear mode.

(5) $\vec{k} = 0$ mode

The growth rate in this branch for $k\lambda_{\text{cool}} \ll 1$ coincides with the case with $k = 0$, which is obtained in section 3.2.

3.3.2 Linear Analysis Considering the Time Evolution of $k\lambda_{\rm cool}(t)$

The static approximation is valid only if Σ is much larger than $|{\rm d}\ln(k\lambda_{\rm cool})/{\rm d}\ln(1-t/t_{\rm c})|$. However, from figure 3.3, it is found that the growth rate of the most unstable mode for each $k\lambda_{\rm cool}$ is smaller than $|{\rm d}\ln k\lambda_{\rm cool}/{\rm d}\ln(1-t/t_{\rm c})|$ whose values are 1.93, 1.5, and 1.37 for $\eta = 0.1$, 0.75, and 0.95 with $\alpha = 0.5$, respectively (see equation (3.22)). Therefore, in this section, we perform linear analysis considering the time evolution of $k\lambda_{\rm cool}(\tau)$ using direct numerical integration. The upwind difference method is used as the numerical method to solve the perturbation equations that are conservation forms. We impose the boundary conditions at $\xi = 0$ and $\xi = 100$. The even mode is set as the boundary condition at $\xi = 0$. The free boundary condition is set at $\xi = 100$, but it does not influence the inner region since the gas flows out supersonically from the outer boundary of the zooming coordinate.

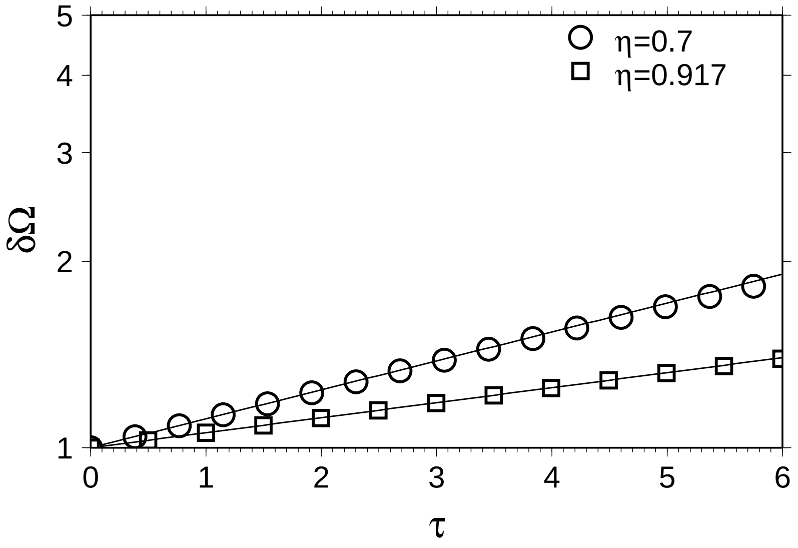

Figure 3.8: Time evolution of $\delta\Omega(\xi = 0)$ for $\eta = 0.7$(the open circles) and 0.917(the open boxes). The solid lines correspond to results from linear analysis.

First, we investigate for the case with $k = 0$ as a test of our finite difference code. We calculate two cases, $\eta = 0.7$ and 0.917. As an initial condition, we adopt the eigenfunction obtained in section 3.2 in each case. By solving equations (3.9)-(3.12), a time evolution of $\delta\vec{Q}$ is obtained. Figure 3.8 shows time evolution of $\delta\Omega(\xi = 0)$ for $\eta = 0.7$(the open circles) and 0.917(the open boxes). The initial value of $\delta\Omega(\xi = 0, \tau = 0)$ is set to unity. From linear analysis in section 3.2, the growth rates for $\eta = 0.7$ and 0.917 are $\Sigma = 0.1076$ and 0.056, respectively, that are shown by the solid lines in figure 3.8. The results by using our finite difference code agree with those of linear analysis very well.

Next, we calculate for the case with finite wavenumber. As an initial state, we adopt the eigenfunction of the isobaric mode for $k\lambda_{\rm cool} = 30$ which is obtained in section 3.3.1. During the calculation, the growth rate at τ is evaluated by

$$\Sigma_{\rm num} = \frac{1}{1-\omega} \frac{\rm d}{{\rm d}\tau} \left\{ \ln \delta\Omega(\xi = 0, \tau) \right\} \tag{3.41}$$

at each instant of time. For comparison with the result of the static approximation, we focus on a relation between $k\lambda_{\rm cool}(t)$ and the growth rate of the density perturbation at the center, $\Sigma_{\rm num}$. Figure 3.9 shows the growth rate $\Sigma_{\rm num}$ as a function of $k\lambda_{\rm cool}(\tau)$ at each instant of time for $\alpha = 0.5$ with (a)$\eta = 0.1$ and (b)0.75. The nondimensional wavenumber, $k\lambda_{\rm cool}$, decreases with time. Therefore, in figure 3.9, the direction of time is from the right to the left. For comparison, the approximate dispersion relations of branches (1)-(2) in figure 3.3 are superimposed by the dashed lines. In both of Figs. 3.9a and 3.9b, the behavior of the growth rate, $\Sigma_{\rm num}$, moderately agrees with that of the approximated dispersion relations. For $k\lambda_{\rm cool} \gg 1$, or initial phase, the growth rate agrees with $\Sigma_{\rm isobaric}$. This is because the growth rate does not depend on $k\lambda_{\rm cool}$ in the short wavelength limit. As $\lambda_{\rm cool}$ decreases and reaches about 1, $\Sigma_{\rm num}$ begins to decrease. For $\lambda_{\rm cool} \ll 1$, $\Sigma_{\rm num}$ approaches asymptotically $\Sigma_{\rm non-int}$, where the effect of $\lambda_{\rm cool}$ is negligible. The effect of time-depending $k\lambda_{\rm cool}$ is notable only for $0.1 < k\lambda_{\rm cool} < 10$. Smoother dependence of the growth rate on $k\lambda_{\rm cool}$ is obtained than the approximate dispersion relation.

3.4 Discussion

3.4.1 The Growth Rate for $1 < \alpha < 2$

Although the linear analysis on the self-similar cooling layer is limited for $\alpha < 1$, the thermal stability of the gas for $\alpha > 1$ is also roughly understood from Balbus's criterion. For $1 < \alpha < 2$, the gas is isobarically unstable, but it is isochorically stable. For $\alpha > 2$, the gas is thermally stable. In this section, we investigate the stability of the gas for $1 < \alpha < 2$ during cooling within the large and small scale limits.

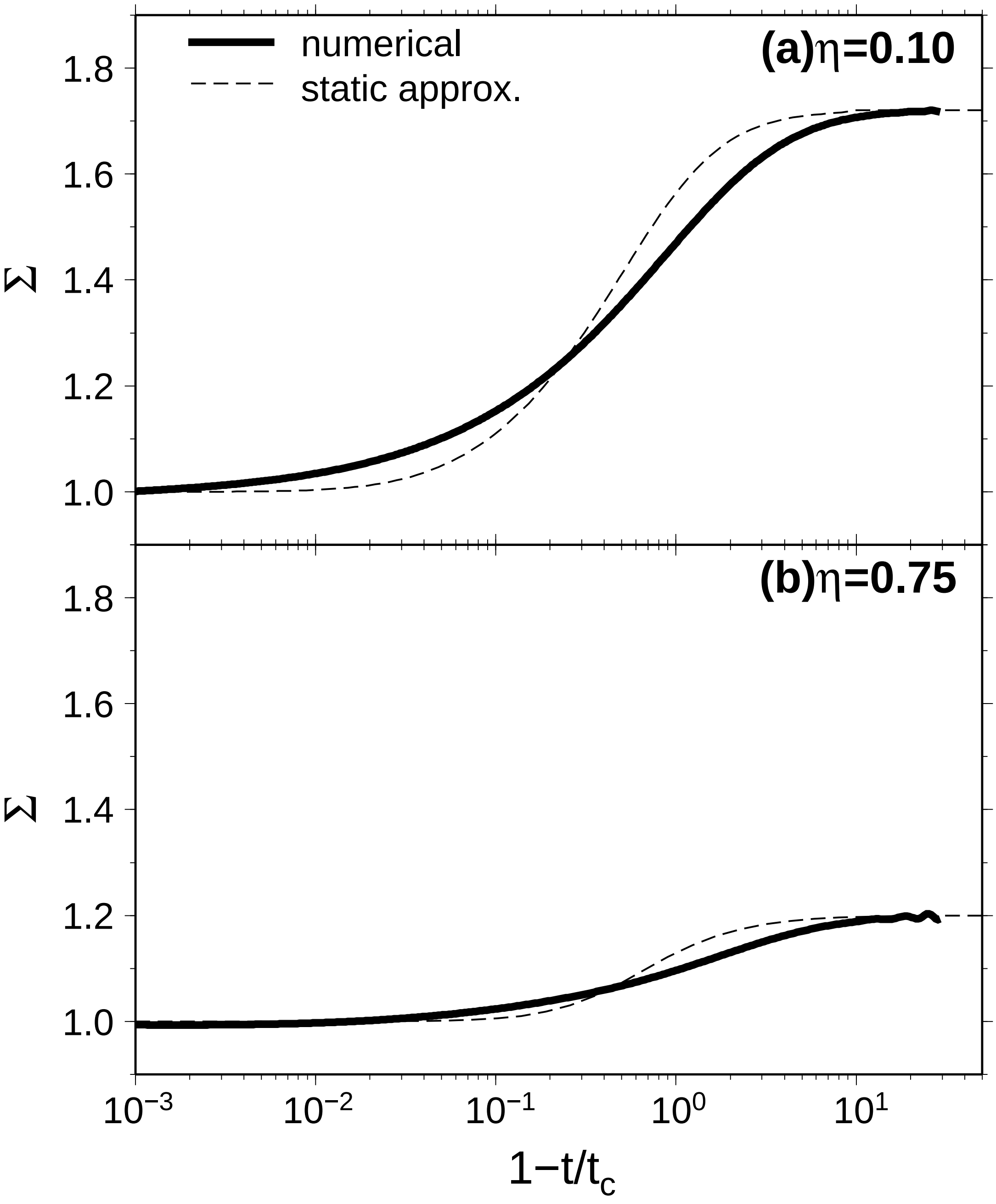

Figure 3.9: Growth rate obtained by results of numerical linear analysis for (a)$\eta = 0.1$ and (b)0.75. The thick and dashed lines indicate the results of numerical linear analysis and those of approximate linear analysis.

The Isobaric Mode

For the case with small wavelength, perturbation is expected to grow isobarically. By comparison of our results with previous studies in the literature, it is found that the growth rate in the isobaric mode is independent of the global structure of the unperturbed state. Therefore, from local arguments, the growth rate in the isobaric mode of the gas with $1 < \alpha < 2$ can also be estimated.

As an unperturbed state, we adopt a cooling gas element whose scale is assumed to be much smaller than the cooling length. In this case, the element cools isobarically. From equation (2.4), the time evolution of the unperturbed gas is given by

$$\rho(t) = \rho_i \left(1 - \frac{t}{t'_{\rm cool}}\right)^{-1/(2-\alpha)}, \frac{1}{t'_{\rm cool}} = (2-\alpha)\gamma^{\alpha-1}(\gamma-1)P_i^{\alpha-1}\rho_i^{2-\alpha}, \tag{3.42}$$

where ρ_i and P_i represent the initial density and pressure, respectively. In the above unperturbed state, we consider the following isobaric perturbation:

$$\rho = \rho_0(t) + \delta\rho(t), \tag{3.43}$$

and

$$P = P_0, \tag{3.44}$$

where subscript "0" indicates the unperturbed state, and $\delta\rho$ is the density perturbation. Linearizing equation (2.4), one obtains

$$\frac{\mathrm{d}}{\mathrm{d}t}\left(\frac{\delta\rho}{\rho_0}\right) = (2-\alpha)\gamma\gamma^{\alpha-1}\rho_0^{2-\alpha}P_0^{\alpha-1}\frac{\delta\rho}{\rho_0}. \tag{3.45}$$

Using equation (3.42), equation (3.45) is rewritten as

$$\frac{\mathrm{d}}{\mathrm{d}t}\left(\frac{\delta\rho}{\rho_0}\right) = \frac{1}{t'_{\rm cool}}\left(1 - \frac{t}{t'_{\rm cool}}\right)^{-1}\frac{\delta\rho}{\rho_0}. \tag{3.46}$$

Equation (3.46) is easily integrated to give

$$\frac{\delta\rho}{\rho_0} \propto \left(1 - \frac{t}{t'_{\rm cool}}\right)^{-1}. \tag{3.47}$$

Comparing equation (3.47) with equation (3.42), one can see that the perturbation grows more slowly than the unperturbed state for $1 < \alpha < 2$. Therefore, the gas is expected to be difficult to fragment during runaway cooling if $1 < \alpha < 2$ otherwise initial fluctuation is sufficiently large.

The Noninteractive Mode

A cooling layer that evolves isobarically is considered. The time evolution of the central density is the same as equation (3.42). When the scale of perturbation perpendicular to the condensation is too large to interact with other regions, each region evolves independently. Here, we focus on the time evolution of density perturbation at the center ($x = 0$). Initial fluctuation of the central density, $\delta\rho_i$, creates the fluctuation of the cooling time, Δt. The relative amplitude of density perturbation at $x = 0$ is given by

$$\frac{\delta\rho}{\rho_0} = \frac{1}{\rho_0}\left(\rho_i + \delta\rho_i\right)\left(1 - \frac{t}{t'_{\mathrm{cool}} - \Delta t}\right)^{-1/(2-\alpha)} - 1. \tag{3.48}$$

Linearizing equation (3.48) with omitting terms that do not grow, we have

$$\frac{\delta\rho}{\rho_0} = \frac{1}{2-\alpha}\frac{\Delta t}{t'_{\mathrm{cool}}}\left(1 - \frac{t}{t'_{\mathrm{cool}}}\right)^{-1}. \tag{3.49}$$

Comparing equation (3.49) with equation (3.42), we can see that the perturbation grows more slowly than the unperturbed state for $1 < \alpha < 2$. Therefore, the gas is expected to be difficult to fragment for $1 < \alpha < 2$ for the large-scale perturbation, as well as the small scale otherwise initial fluctuation is sufficiently large.

3.4.2 Effects of Heat Conduction

In this paper, the heat conduction is neglected for simplicity. However, for large wavenumber, the heat conduction is expected to stabilize thermal instability in the cooling layer (Field, 1965). In section 1.4.1, we evaluate k_{crit} in equation (1.17) using an order estimation. This estimation is expected to be valid in cooling layers. Since the unperturbed state is time dependent, k_{crit} also evolves with time. Detailed evolution of k_{crit} depends on K. In $T < 6000$, we adopt $K = 2.5 \times 10^3\sqrt{T}$ ergs cm^{-1} K^{-1} s^{-1} (Parker, 1953). In this case, from equation (1.17), the time evolution of k_{crit} can be derived analytically as

$$\begin{aligned}\frac{\mathrm{d}\ln k_{\mathrm{crit}}}{\mathrm{d}\ln(1 - t/t_{\mathrm{c}})} &= \frac{(2\alpha-1)\eta - (2-\alpha)(3-2\alpha)}{4(2-\alpha)(1-\alpha)} \\ &= \begin{cases} -\dfrac{7-2\alpha}{4(2-\alpha)} < 0 & \text{for } \eta = 1 \\ -\dfrac{3-2\alpha}{4(1-\alpha)} < 0 & \text{for } \eta = 0 \end{cases}.\end{aligned} \tag{3.50}$$

For $\eta = 1$ and $\eta = 0$, it is found that equation (3.50) is negative for $\alpha < 1$. Since equation (3.50) is the linear function for η, $\mathrm{d}\ln k_{\mathrm{crit}}/\mathrm{d}\ln(1 - t/t_{\mathrm{c}})$ is negative for all η. Therefore,

$k_{\rm crit}$ increases with time. This means that an initially stable perturbation with wavenumber ($k > k_{\rm crit}$) becomes unstable at a certain epoch when $k_{\rm cirt}$ catches up with k.

3.5 Summary

We have investigated the stability of self-similar solutions describing the runaway cooling of a radiative gas by linear analysis to understand multi-dimensional evolution of the dynamically cooling gas layer. The results of our investigation are summarized as follows;

1. For the case with perturbation only parallel to the flow ($k = 0$), the self-similar solutions are unstable. However, the growth rate is too low to become nonlinear during the runaway cooling. Actually, the self-similar solutions are realized in one-dimensional hydrodynamical calculations.

2. For the case with transverse perturbation ($k \neq 0$), there are several unstable modes in the self-similar solutions. The most unstable modes are the isobaric mode for $k\lambda_{\rm cool} \gg 1$ and the noninteractive mode for $k\lambda_{\rm cool} \ll 1$. In the isobaric mode, the perturbation grows in pressure equilibrium with its surroundings. On the other hand, the noninteractive mode is originated from each region in the layer condensing independently. Under a static approximation, we derive the approximated dispersion relation. The results of direct numerical integration of the time evolution agree with those using the static approximation.

3. The isobarically cooling layer $\eta \sim 0$ is unstable for any wavenumbers. The most unstable mode is the isobaric mode for large wavenumber, $k\lambda_{\rm cool} \gg 1$. The perturbation for $k\lambda_{\rm cool} \ll 1$ grows like in the isochoric mode.

4. The isobarically condensing layer $\eta \sim 1$ is unstable for any wavenumers. The remarkable result is that the perturbations grow as $\propto (1 - t/t_{\rm c})^{-1}$ without depending on wavenumbers and the index parameter, α. Moreover, the perturbations for all wavenumbers grows in the isobaric mode. Therefore, there is not a characteristic scale in thermal instability of the condensing gas layer. The linear analysis predicts that the condensing gas layer split into fragments with various scales and shapes, such as spherical and filamentary clouds.

Chapter 4

Two-dimensional Numerical Simulations of Cooling Gas Layers

In chapter 3, we investigated linear stability of the self-similar solutions describing the dynamically cooling layers. In this chapter, we check results of the linear analysis and investigate nonlinear evolutions of the cooling layers using two-dimensional numerical simulation.

4.1 Numerical Method

We use two-dimensional smoothed particle hydrodynamics (SPH) that is a Lagrangian particle method. SPH has priority in problems where high density contrast appears. The detailed description of SPH and test calculations are presented in Appendix E.

4.2 Isobarically Condensing Layer with Power-Law Net Cooling Rate

In chapter 2, we have showed the isobarically condensing layer is well described by the self-similar solution for $\eta \sim 1$. As the initial condition, we adopt the self-similar solution for $\eta = 0.917$ at $t = 0$. The index parameter in equation (2.1) is set to 0.5. We assume that $\lambda_{\rm cool}(t = 0) = 1$ and $\Lambda_0 = 1$. The initial profiles of the physical variables are given by

$$\rho(t = 0, x, y) = \Omega(x), \;\; v(t = 0, x, y) = V(x), \;\; P(t = 0, x, y) = \Pi(x). \qquad (4.1)$$

The epoch when the central density becomes infinity is $t_{\rm c} = 1/(1-\omega) = 1.389$. This simulation must resolve the scale of the density peak that is defined as $\zeta\lambda_{\rm cool}(t)$, where parameter, ζ, is smaller than 1 for the isobarically condensing layer. The resolution criterion is given by

$$\pi\rho_{00}(t)\left\{\zeta\lambda_{\rm cool}(t)\right\}^2 > N_{\rm neib}m_i, \tag{4.2}$$

where $N_{\rm neib}$ is the number of neighbor particle, m_i is the particle mass, and ρ_{00} is the central density. The left-hand side of equation (4.2) indicates the mass within the circle whose radius is $\zeta\lambda_{\rm cool}$. Using $\lambda_{\rm cool}(t) = (1-t/t_{\rm c})^{1/(1-\omega)}$ and $\rho_{00}(t) = \Omega_{00}(1-t/t_{\rm c})^{-\eta/(2-\alpha)}$, the constraint on the particle mass is

$$m_i < 8.54 \times 10^{-7}\left(\frac{\zeta}{0.5}\right)^2\left(\frac{N_{\rm neib}}{28}\right)^{-1}\left(\frac{1-t/t_{\rm c}}{0.01}\right)^{(3-2\alpha-\eta)/(1-\alpha)}. \tag{4.3}$$

In this calculation, m_i is set to be 1.058×10^{-6}. Therefore, this calculation is valid for $1-t/t_{\rm c} > 0.01$, or $t < 0.99t_{\rm c}$.

The simulation region in the x-direction is $-1.5\xi_{\rm s}(t=0) \leq x \leq 1.5\xi_{\rm s}(t=0)$. The boundary condition of the x-direction does not influence in the inner region of $-\xi_{\rm s} < x < \xi_{\rm s}$ since the gas flows out supersonically from $\xi_{\rm s}$ in the zooming coordinate (see section 3.2.2). The size of the simulation box in the y-direction is given by L_y, and the periodic boundary condition is imposed.

4.2.1 Case Without Initial Fluctuations

First, we present results without initial fluctuation. We set L_y to 0.17. Figures 4.1a and 4.1b show the snapshots of the density and pressure as a function of x, respectively, at $1-t/t_{\rm c} = 0.96$, 0.4, 0.2, and 0.05. The red dots indicate the results of SPH calculation. The solid lines denote the self-similar solution at each corresponding time. Figures 4.1a and 4.1b show that the two-dimensional SPH calculation can reproduce the self-similar solution well.

4.2.2 Case With Initial Fluctuations

We add the following sinusoidal density perturbations in the y-direction into the initial condition,

$$\rho(t=0,x,y) = \Omega(x)\left\{1 + A\sin(ky)\right\}, \tag{4.4}$$

(a) Density

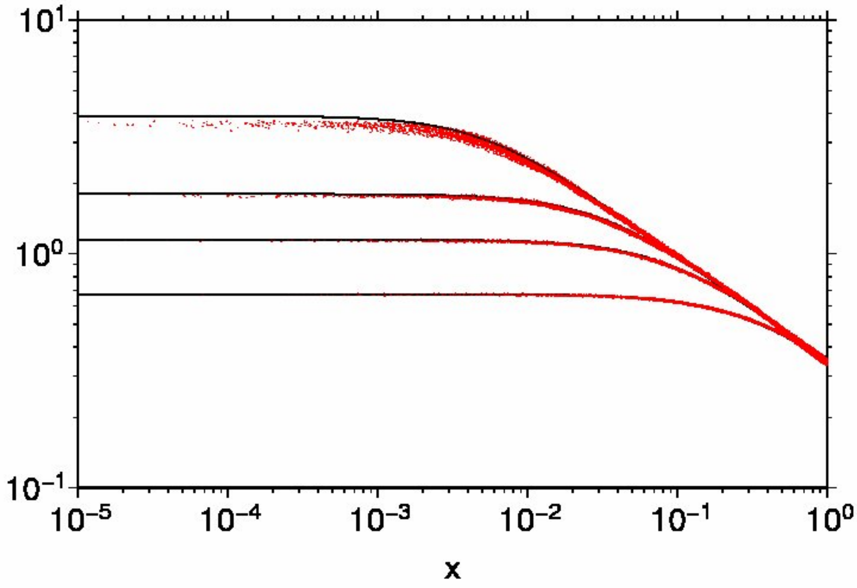

(b) Pressure

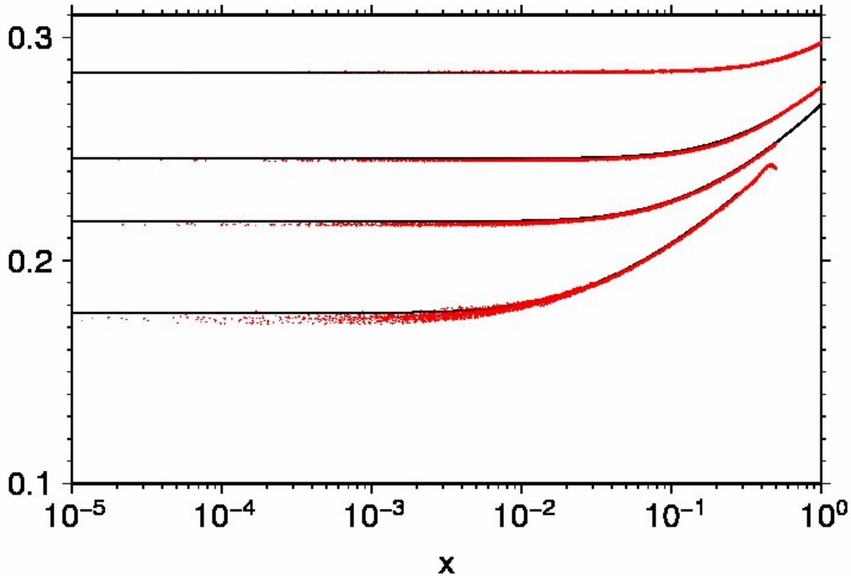

Figure 4.1: Time evolution of (a)the density and (b)the pressure profiles for $1 - t/t_{\rm c} = 0.96$, 0.4, 0.2, and 0.05. The red dots denote the results of SPH calculation. The solid lines denote the self-similar solution at each corresponding time.

where A is set to 0.1. We investigate for the case with a large wavenumber case ($k = 36.87$) and with a small wavenumber case ($k = 1.8435$). We set L_y so that the simulation box contains single wavelength. From the linear analysis in chapter 3, the growth of the perturbation is determined by $k\lambda_{\rm cool}(t)$. The perturbations grow in the isobaric mode for $k\lambda_{\rm cool}(t) \gg 1$ and in the noninteractive mode for $k\lambda_{\rm cool}(t) \ll 1$. In both modes, the amplitude of the density perturbation is larger than that of the pressure perturbation. The isobaric mode grows as $(1-t/t_{\rm c})^{-1.066}$ and the noninteractive mode grows as $(1-t/t_{\rm c})^{-1}$, where $t_{\rm c}$ is the epoch when the central density becomes infinity. Since the nondimensional wavenumber decreases with time as $k\lambda_{\rm cool}(t) = k(1-t/t_{\rm c})^{1/(1-\omega)}$, the growing mode changes from the isobaric mode to the noninteractive mode at the epoch, $t_{\rm trans}$, when $k\lambda_{\rm cool}(t)$ becomes unity. These transition epochs are $(1 - t_{\rm trans}/t_{\rm c}) = 0.07$ and 0.64 for $k\lambda_{\rm cool}(0) = 36.87$ and 1.8435, respectively.

To evaluate the growth of the perturbations, we focus on the density at $x = 0$. The simulation box in the y-direction is divided by equal-size meshes whose total number is N. The width of the meshes is set to the minimum smoothing length in all particles at each time. We define the average density,

$$\rho_{\rm ave} = \frac{1}{N}\sum_{i=1}^{N}\rho_i, \tag{4.5}$$

the density dispersion,

$$\Delta\rho = \sqrt{\frac{1}{N}\sum_{i=1}^{N}\left\{\rho_i - \rho_{\rm ave}\right\}^2}, \tag{4.6}$$

and the maximum density,

$$\rho_{\rm max} = \max_{i=1}^{N}\rho_i, \tag{4.7}$$

where ρ_i is the density at the i-th mesh.

Figures 4.2a and 4.2b show the time evolution of density perturbations for $k = 36.87$ and 1.8435, respectively. The open triangles and open circles indicate $\rho_{\rm max}/\rho_{\rm ave}$ and $\Delta\rho/\rho_{\rm ave}$, respectively. The direction of time is from the right to the left. The dotted vertical lines denote the transition epochs, $(1-t_{\rm trans}/t_{\rm c})$. Perturbations grow in the isobaric and noninteractive modes in the right and left sides of the line, respectively. For the large wavenumber case, $k = 36.87$, the perturbation grows in the isobaric mode since $(1 - t_{\rm trans}/t_{\rm c})$ is small. Figure 4.2a shows that the growths of $\rho_{\rm max}/\rho_{\rm ave}$ and $\Delta\rho/\rho_{\rm ave}$ agree with that of the isobaric

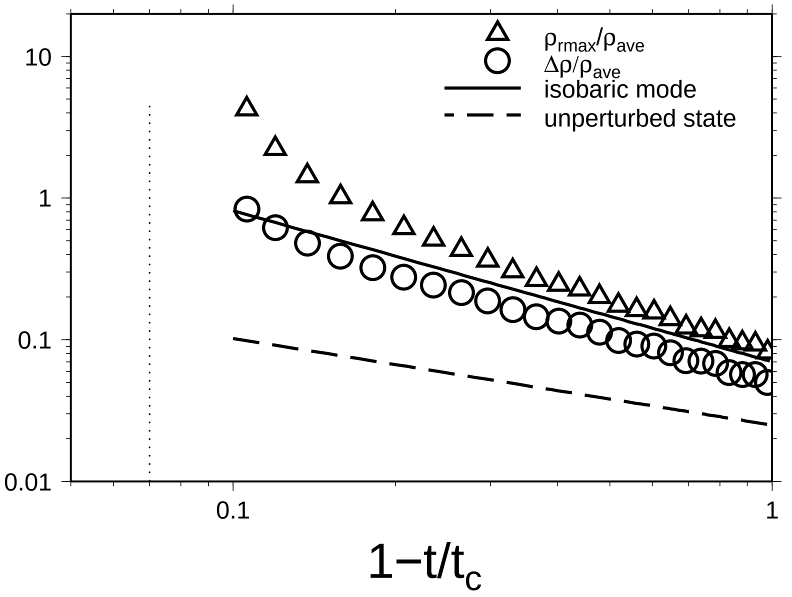
(a) $k\lambda_{\mathrm{cool}}(t=0)=36.87$

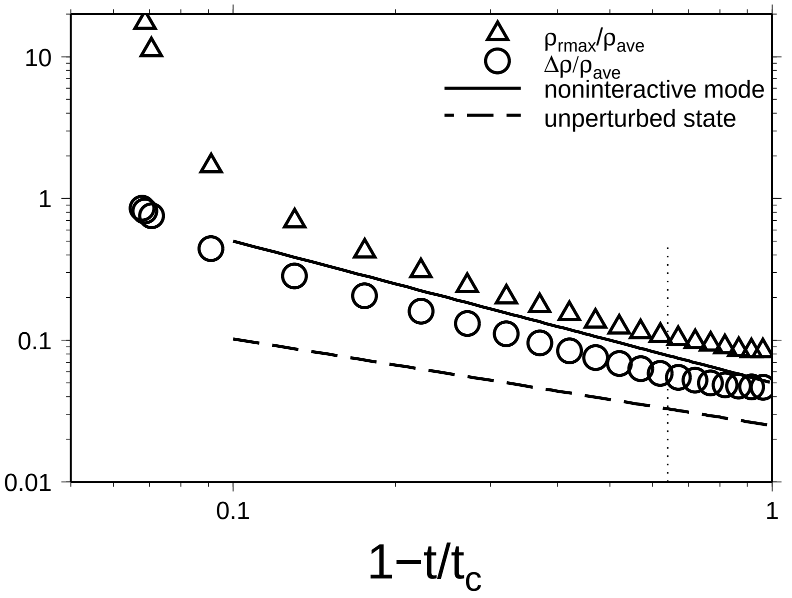
(b) $k\lambda_{\mathrm{cool}}(t=0)=1.8435$

Figure 4.2: Time evolution of density perturbations for (a)$k\lambda_{\mathrm{cool}}(t = 0) = 36.87$ and (b)1.8435. The open triangles and open circles indicate $\rho_{\mathrm{max}}/\rho_{\mathrm{ave}}$ and $\Delta\rho/\rho_{\mathrm{ave}}$, respectively. The solid lines correspond to the growth rates of (a)the isobaric mode and (b)the noninteractive mode. The dashed lines indicate the increasing rate the unperturbed density. The direction of the time is from the right to the left.

mode that is plotted by the solid line. For $k = 1.8435$, as soon as the calculation starts, the perturbation enters the noninteractive mode. Figure 4.2b shows that the growths of $\rho_{\rm max}/\rho_{\rm ave}$ and $\Delta\rho/\rho_{\rm ave}$ agree with that of the noninteractive mode that is plotted by the solid line. After perturbations become nonlinear, or $\rho_{\rm max}/\rho_{\rm ave}$ exceeds unity, $\rho_{\rm max}/\rho_{\rm ave}$ grows much faster than the prediction of the linear theory. This is because the highest density becomes infinity before the unperturbed collapse time, $t_{\rm c}$. Therefore, the growth of perturbation does not saturate in the nonlinear phase and perturbations continue to grow until the highest density becomes infinity.

The density profiles in the y-direction at $x = 0$ for $k = 36.87$ and 1.8435 are shown in figures 4.3a and 4.3b, respectively, at $1 - t/t_{\rm c} = 0.96$, 0.52, and 0.13. In figure 4.3b, the profile at $1 - t/t_{\rm c} = 0.96$ has fluctuations with larger wavenumbers than $k = 1.8435$. In SPH calculation, some amount of fluctuations based on distributions of particles always exists. These small fluctuations can grow since the growth rate of the perturbation with $k > 1.8435$ is comparable to that with $k = 1.8435$.

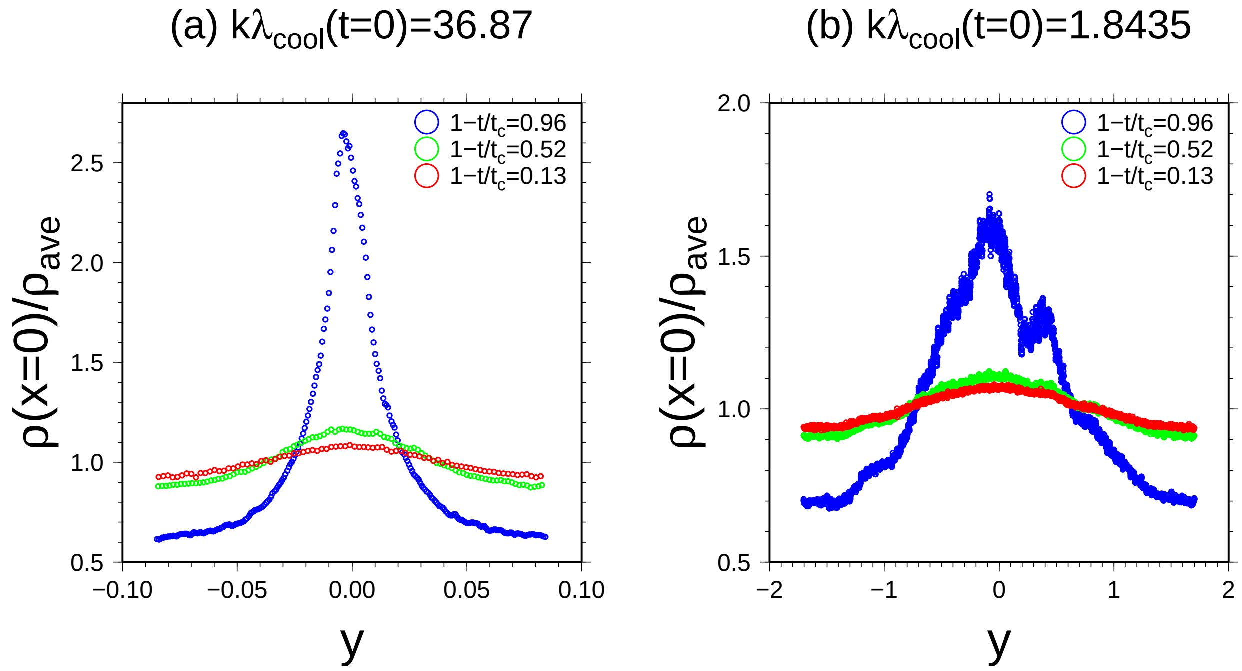

Figure 4.3: The density profiles normalized by the average densities for (a)$k\lambda_{\rm cool}(t = 0)$ =36.87 and (b)1.8435 at $x = 0$ at $1 - t/t_{\rm c} = 0.96$, 0.52, and 0.13.

4.3 Isochorically Cooling Layer with Power-Law Net Cooling Rate

We consider isochorically cooling uniform gas that corresponds to self-similar homologous solutions for $\eta = 0$ (see 2.1.4). In Appendix B, we perform linear analysis of homologous solutions for $\eta = 0$. From the linear analysis, perturbations grow in the isobaric mode for $k\lambda_{\mathrm{cool}} \gg 1$ and in the noninteractive mode for $k\lambda_{\mathrm{cool}} \ll 1$. Contrary to isobaric self-similar solutions, in the noninteractive mode, the amplitude of the density perturbation is smaller than that of the pressure perturbation. From linear analysis, the isobaric mode grows as $\propto (1 - t/t_{\mathrm{c}})^{(2-\alpha)/\{\gamma(1-\alpha)\}}$, and the noninteractive mode grows as $\propto (1 - t/t_{\mathrm{c}})^{-1}$.

Since the unperturbed state is uniform, the minimum dimension for investigating growth of thermal instability is one dimension. Therefore, we use the 2nd-order one-dimensional Godunov code (van Leer, 1997). The initial density, pressure and velocity profiles in the unperturbed state are given by

$$\rho_0(x) = \frac{1}{\gamma(\gamma-1)}\left(\frac{2}{3-2\alpha}\right)^{3-2\alpha}, \quad P_0(x) = \frac{1}{\gamma^2(\gamma-1)}\left(\frac{2}{3-2\alpha}\right)^{5-2\alpha}, \quad \text{and} \quad v_0(x) = 0, \tag{4.8}$$

where we determine $\lambda_{\mathrm{cool}}(0) = 1$, $\Lambda_0 = 1$, and $t_{\mathrm{c}} = 1/(1-\omega)$ in equation (2.64). We set the index parameter α to 0.5. A perturbation with $k = 10$ is considered. The computation domain is $-\pi/k < x < \pi/k$, and the periodic boundary condition is imposed. As the initial condition, we add eigenfunction obtained in Appendix B.

Figure 4.4 shows time evolution of $\Delta\rho/\rho_{\mathrm{ave}}$ and $\Delta P/P_{\mathrm{ave}}$. The thin solid and dotted lines indicate growth rate of the isobaric and the noninteractive mode. Initially, since $kt_{\mathrm{cool}}(t) > 1$, the density perturbation grows as the isobaric mode. An epoch when $kt_{\mathrm{cool}}(t)$ becomes unity is $1 - t/t_{\mathrm{c}} = 0.18$ that is shown by the vertical dotted line. Figure 4.4 shows that around this epoch, the growth of the density perturbation slows down. On the other hand, the pressure perturbation begins to grow faster than the density perturbation. Figure 4.4 shows that the time evolution of $\Delta P/P_{\mathrm{ave}}$ agree with the growth of the noninteractive mode for $1 - t/t_{\mathrm{c}} > 0.18$.

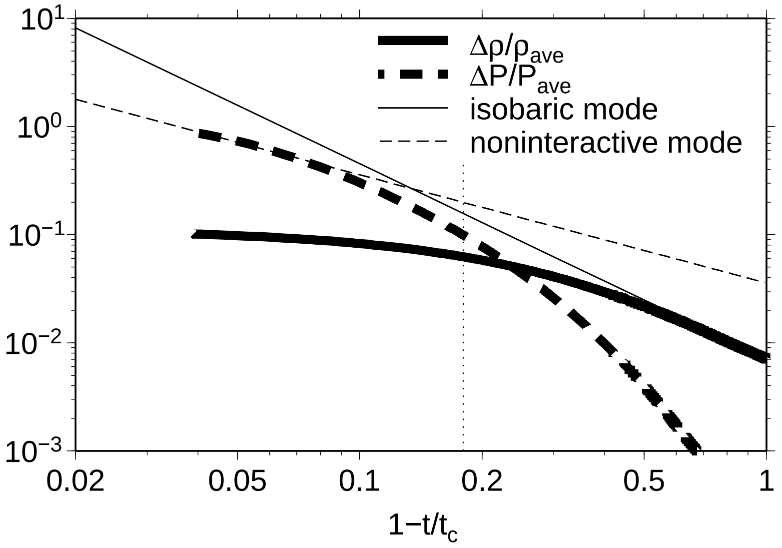

Figure 4.4: Time evolution of $\Delta\rho/\rho_{\rm ave}$ (thick solid lines) and $\Delta P/P_{\rm ave}$ (thick dashed lines) for $k\lambda_{\rm cool}(t = 0) = 10$. The thin solid and dashed lines indicate growth rates of the isobaric and noninteractive mode. The vertical dotted line indicates the transition epoch from the isobaric mode to the noninteractive mode.

4.4 Two-dimensional Simulation of the Formation of Interstellar Clouds

In this section, we investigate two-dimensional simulation of the formation of interstellar clouds. We consider head-on collision between spatially uniform WNM gas with the density of $\rho_{\rm WNM} = 0.57 m_{\rm H}$ cm^{-3} and the pressure of $P_{\rm WNM} = 3.5 \times 10^3 k_{\rm B}$ dyne cm^{-2}. Two identical gases collide along the x-axis at $t = 0$ and $x = 0$ with velocity 20 km s^{-1}, i.e., the corresponding mach number is 2.17. This situation is the same as that in section 2.3.1. The calculation domain is $-25\,{\rm pc} < x < 25\,{\rm pc}$ and $-0.1\,{\rm pc} < y < 0.1\,{\rm pc}$. The physical variables in the boundaries of the x-direction are fixed by the initial values. The periodic boundary condition is imposed in the y-direction. Koyama and Inutsuka (2004) suggests that numerical codes must contain the heat conduction and must resolve $\lambda_{\rm F}$ to obtain converging results. In this calculation, we take into account of the heat conduction, and set the particle mass m_i so that the smoothing length at $\rho = 10^3 m_{\rm H}$ is as small as 10^{-4}pc. The total number of the SPH particles is as large as 6.5×10^5.

We calculate the converging flow of the WNM without fluctuation until the highest density gas becomes unstable at $t \sim 0.4$ Myr. At $t = 0.4$ Myr, we add the following density fluctuation:

$$\delta\rho(x, y, t = 0.4\ \mathrm{Myr}) = \sum_{k=1}^{i_{\max}} \frac{A}{i_{\max}} \sin\left(\frac{2\pi}{L_y} y + \theta_i\right), \tag{4.9}$$

where θ is the random number of $[0, 2\pi]$, $i_{\max}$ and A are set to 5 and 0.1, respectively.

4.4.1 Results

In shock-compressed region, the runaway condensation breaks out. As shown in section 2.3.1, the one-dimensional evolution of the runaway condensing layer is well described by the self-similar solution for $\eta \sim 1$. The linear analysis shows that perturbations grow as $\propto (1 - t/t_{\mathrm{c}})^{-1}$ without depending on their scales. In order to compare with result of the linear analysis, we evaluate $\Delta\rho/\rho_{\mathrm{ave}}$ and $\rho_{\max}/\rho_{\mathrm{ave}}$ at $x = 0$ (see equations (4.5)-(4.7)). Figure 4.5 shows time evolution of $\Delta\rho/\rho_{\mathrm{ave}}$ and $\rho_{\max}/\rho_{\mathrm{ave}}$ at $x = 0$. The thin solid line indicates $\propto (1 - t/t_{\mathrm{c}})^{-1}$ that corresponds to the linear growth rate. The result of the two-dimensional simulation agrees with that of the linear analysis well.

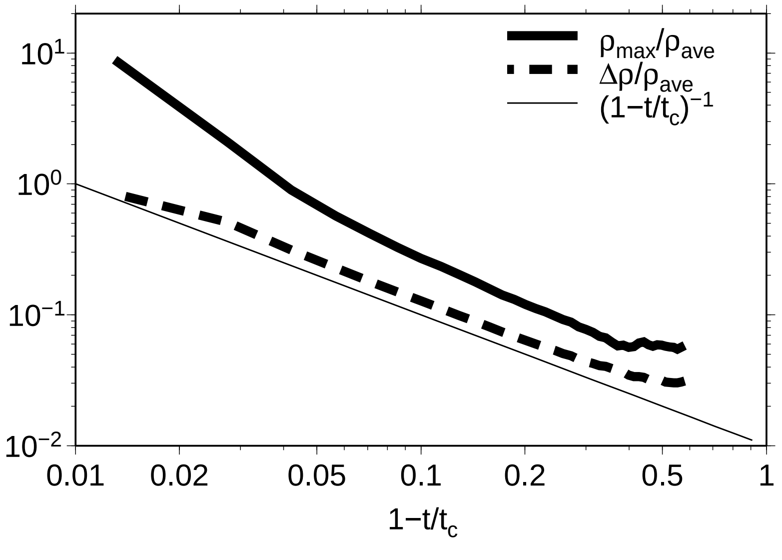

Figure 4.5: Time evolution of $\rho_{\max}/\rho_{\mathrm{ave}}$ (thick solid lines) and $\Delta\rho/\rho_{\mathrm{ave}}$ (thick dashed lines). The thin solid line indicates $\propto (1 - t/t_{\mathrm{c}})^{-1}$.

Figure 4.6 shows time evolution of $\rho_{\max}(y)$ that indicates the maximum density at y over the range of $-L_x/2 < x < L_x/2$ as a function of $(1 - t/t_{\mathrm{c}})$, where we set t_{c} to 0.985 Myr.

Initially, perturbation grows obeying the linear analysis as $\propto (1 - t/t_{\rm c})^{-1}$. The gas at the highest density portion at $y \sim -0.02$ pc reaches the thermal equilibrium phase and stops condensing at $t \sim 0.97$ Myr. After that, as the large scale perturbation continues to cool and condenses, the plateaus of CNM broaden. In the low density region of the large scale perturbation at $y \sim -0.08$ and $y \sim 0.04$, small scale fluctuations grow. In this thesis, cold clouds formation is defined by the formation of the sharp contact discontinuities that divide cold clouds and warm gases. At $t \sim 1.1$ Myr, filamentray and spherical clouds are generated. Figure 4.7 shows the number density color maps at 0.97, 1.00, 1.03, 1.06, and 1.10 Myr. One can see that the filamentary and spherical clouds are generated.

The linear analysis in chapter 3 predicts that any scale perturbations grow in the same way. In the nonlinear calculation, we confirm various scale clouds are generated. The mass distribution of cold clouds depends on initial condition, and there is not characteristic scale.

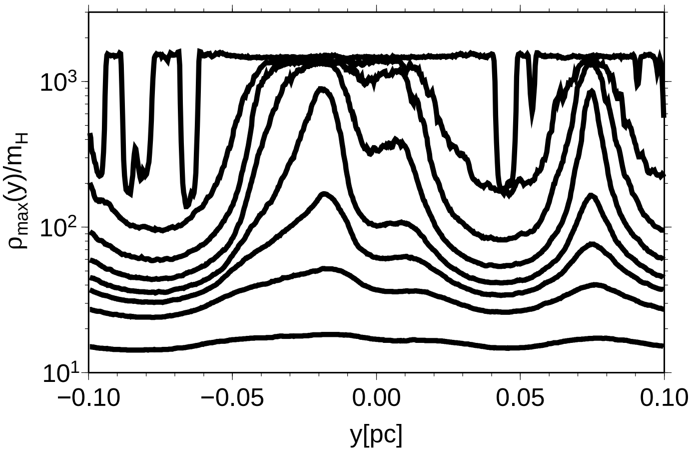

Figure 4.6: Time evolution of $\rho_{\rm max}(y)$. Each Line corresponds to t = 0.82, 0.93, 0.96, 0.97, 0.99, 1.00, 1.02, 1.1 Myr from bottom to up.

4.5 Summary

We investigate two-dimensional nonlinear evolution of the cooling layer. The results of our investigation are summarized as follows,

- We investigate nonlinear evolution of the isobarically condensing self-similar solution by using the two-dimensional simulation. We can confirm that perturbations grows as

$\propto (1 - t/t_{\rm c})^{-1}$ for all scale fluctuations. After the perturbations becomes nonlinear, they continues to condense until the maximum density becomes infinity.

- We investigate nonlinear evolution of the isochorically cooling uniform gas by the one-dimensional calculation. The perturbation for $\lambda < \lambda_{\rm cool}(t = 0)$ initially grows in the isobaric mode. This growth rate agrees with the prediction from the linear analysis well. As the gas cools, the cooling length decreases. After an epoch when $\lambda > \lambda_{\rm cool}$, the perturbation grows in the noninteractive mode where the density perturbation does not grow. We confirm that the growth rate of the pressure agrees with the linear analysis.
- The nonlinear evolution of a condensing layer arising from converging WNM flows is investigated by using the two-dimensional simulation. In the linear phase, the perturbation grows obeying prediction from the linear analysis, After the highest density gas gets thermal equilibrium, the surrounding gas continues to cool and condense. As large scale perturbations grow, filamentary structures form. In the low density region in large scale perturbations, smaller scale perturbation begins to grow and spherical clouds form. As a result, cold clouds that have various shapes and masses are generated in the shock-compressed region. There is not the characteristic size and mass of the cold clouds.

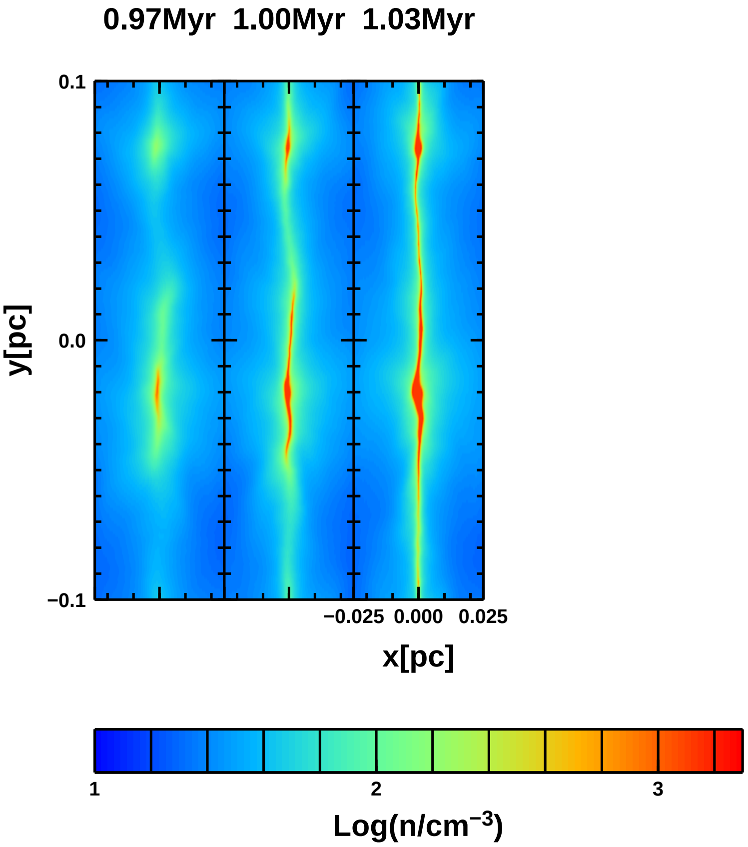

Figure 4.7: Number density color maps at 0.97, 1.00, 1.03, 1.06, 1.10 Myr.

Chapter 5

Summary and Future Prospects

5.1 Summary

In this thesis, we have investigated the formation process of cold clouds by thermal instability in shock-compressed regions. One-dimensional simulation of the formation of cold clouds shows that a isobarically condensing layer breaks out in the shock-compressed region. The condensing layer becomes cold clouds when it reaches a thermal equilibrium state. In order to understand the size and shape of the cold clouds, it is important to investigate multi-dimensional evolution of the isobarically condensing layer. In previous works of linear analysis of thermal instability, the unperturbed states are assumed to be spatially uniform and/or their time-dependences are neglected. These linear analyses cannot be applied to the stability of the isobarically condensing layer because it is far from spatially uniform and depends on time.

We proposed new self-similar solutions describing nonlinear evolution of dynamically cooling gas layers as the more realistic one-dimensional model. The self-similar solutions have one parameter η that ranges 0 from 1. The parameter η shows how the gas layer cools. In the self-similar solution for $\eta \sim 0$, the gas cools remaining density constant. This is because the scale length of the cooling layer is much larger than the cooling length that the sound wave travels within a characteristic timescale of cooling. The self-similar solutions for larger η correspond to the cooling layers with longer scale length. For $\eta \sim 1$, the scale of the cooling layer is much shorter the cooling length. Therefore, the self-similar solution for $\eta \sim 1$ describes the isobarically condensing layer because the gas cools maintaining pressure equilibrium with its surroundings. We showed that the self-similar solution for $\eta \sim 1$ well describes the one-dimensional nonlinear evolution of the runaway condensing layer in the astrophysical environment.

In order to investigate multi-dimensional evolution of the runaway cooling layer, we investigated linear stability of the self-similar solutions. The most interesting result is that the isobarically condensing layer is unstable and the perturbation grows as $(1 - t/t_{\rm c})^{-1}$ without depending on its scale, where $t_{\rm c}$ is the epoch when the unperturbed peak density becomes infinity. In the previous works, the scale of the most unstable mode is shorter than the cooling length. The linear analysis predicts the condensing layer splits into fragments with various scales. We investigated two-dimensional nonlinear evolution of the runaway condensing layer that is generated by the colliding flow of warm neutral medium using two-dimensional smoothed particle hydrodynamics. This simulation showed that the condensing layer splits into spherical clouds whose size is about < 0.01 pc and filamentary clouds whose aspect ratio can be smaller than 0.2. The size of the small spherical clouds is similar to the tiny HI clouds that have been discovered recently (Braun and Kanekar, 2005; Stanimirović and Heiles, 2005). In previous studies using two-dimensional simulation, these filamentary clouds also are observed.

Our analysis predicts the mass distribution of the infant cold clouds directly reflects the power spectrum of the fluctuation of the unstable gas. Observationally, the warm gas intrinsically has a turbulence (see section 1.2.4). Moreover, even if there is not turbulence in the warm gas, recent two-dimensional simulations show that the turbulent motion is generated in the shocked unstable gas by hydrodynamical instabilities, such as thin shell instability (Vishniac, 1994), Kelvin-Helmholtz instability (Chandrasekhar, 1961), and so on. Therefore, the mass distribution of the infant cold clouds is expected not to have a characteristic scale and to be power-law.

5.2 Future Prospects

The calculation domain of the two-dimensional simulation in this thesis is too small to investigate relation between the power spectrum of the fluctuation of the unstable gas and the mass spectrum of the formed cold clouds. Moreover, the thesis cannot address the problem of the time evolution of the mass spectrum of the cold clouds that is important for that of molecular clouds. We will address this problem for future work.

Koyama and Inutsuka (2002) found that generated CNM clouds gets supersonic velocity dispersion. The detailed mechanism of this process remains unknown. Since there is high density contrast between CNM clouds and unstable gases and WNM gases, it is possible to occur various instabilities, such as Rayleigh-Taylor instability, corrugation instability of transition front between CNM and WNM (Inoue, Inutsuka, and Koyama, 2006), and Kelvin-Helmholtz instability, and so on. We will tackle this problem for future work.

In this thesis, we do not take into account of magnetic field that is important elements in interstellar physics. Inoue and Inutsuka (2009) suggested that the magnetic field is expected to strongly affect the formation of interstellar clouds, depending on the orientation of magnetic field with respect to the shock front. If the magnetic field is perpendicular to the converging flow, the magnetic field suppresses molecular cloud formation. On the other hand, if the magnetic field is parallel to the converging flow, molecular cloud can be formed. This is because one dimensional evolution of the cooling layer is not affected by the magnetic pressure. However, the magnetic field can affect fragmentation of the cooling layer through the magnetic tension and pressure (Inoue, 2009 private communication). This process possibly modifies the size distribution of generated CNM clouds. We will perform linear analysis including magnetic field for future work.

Appendix A

Thermal Instability of Gas in Thermal Equilibrium

In this appendix, we perform linear analysis of a spatially uniform gas in thermal equilibrium, or $\Lambda = \Gamma$ (Field, 1965).

A.1 Perturbation Equations

The unperturbed state is

$$\rho(\vec{x},t) = \rho_0, \;\; P(\vec{x},t) = P_0, \;\; T(\vec{x},t) = T_0, \;\; \text{and} \;\; \vec{v} = 0. \tag{A.1}$$

We consider the following perturbed quantities,

$$\begin{aligned} \rho(\vec{x},t) &= \rho_0 + \delta\rho e^{\omega t + i\vec{k}\cdot\vec{x}} \\ P(\vec{x},t) &= P_0 + \delta P e^{\omega t + i\vec{k}\cdot\vec{x}} \\ T(\vec{x},t) &= T_0 + \delta T e^{\omega t + i\vec{k}\cdot\vec{x}} \\ \vec{v}(\vec{x},t) &= \delta\vec{v} e^{\omega t + i\vec{k}\cdot\vec{x}}. \end{aligned} \tag{A.2}$$

Substituting equation (A.3) into basic equations (2.2)-(2.5) and linearizing, one can obtain as

$$\omega\delta\rho + i\rho_0\vec{k}\cdot\delta\vec{v} = 0, \tag{A.3}$$

$$\omega\rho_0\delta\vec{v} + i\vec{k}\delta P = 0, \tag{A.4}$$

$$\frac{1}{\gamma-1}\left(\omega\delta P-\gamma\frac{P_0}{\rho_0}\omega\delta\rho\right)=-\rho_0\left(\frac{\partial\mathcal{L}_0}{\partial\ln\rho_0}\right)_T\frac{\delta\rho}{\rho_0}-\rho_0\left(\frac{\partial\mathcal{L}_0}{\partial\ln T_0}\right)_\rho\frac{\delta T}{T_0}-|\vec{k}|^2K_0\delta T, \tag{A.5}$$

and

$$\frac{\delta P}{P_0}=\frac{\delta\rho}{\rho_0}+\frac{\delta T}{T_0}. \tag{A.6}$$

Here, we define the characteristic wave number, k_{K}, that is related to the heat conduction as

$$k_{\mathrm{K}}=\frac{P_0c_{\mathrm{s}}}{(\gamma-1)K_0T_0}, \tag{A.7}$$

which is the reciprocal number of the mean free path of the gas.

A.2 Dispersion Relation

From equations (A.3)-(A.6), one can obtains the following dispersion relation,

$$\left(\gamma\omega^2+c_{\mathrm{s}}^2k^2\right)\left\{\omega+\frac{1}{t_{\mathrm{cool}}\Lambda_0}\left(\frac{\partial\mathcal{L}_0}{\partial\ln T_0}\right)_\rho+c_{\mathrm{s}}\frac{k^2}{k_{\mathrm{K}}}\right\}-c_{\mathrm{s}}^2k^2\left\{(1-\gamma)\omega+\frac{1}{t_{\mathrm{cool}}\Lambda_0}\left(\frac{\partial\mathcal{L}_0}{\partial\ln\rho_0}\right)_T\right\}=0. \tag{A.8}$$

If we use the simplified power-law cooling function (equation (1.2)), the dispersion relation becomes

$$\left(\gamma\omega^2+c_{\mathrm{s}}^2k^2\right)\left\{\omega+\frac{\alpha}{t_{\mathrm{cool}}}+c_{\mathrm{s}}\frac{k^2}{k_{\mathrm{K}}}\right\}-c_{\mathrm{s}}^2k^2\left\{(1-\gamma)\omega+\frac{1}{t_{\mathrm{cool}}}\right\}=0, \tag{A.9}$$

A.2.1 $k\lambda_{\mathrm{cool}}\gg 1$

For $k\lambda_{\mathrm{cool}}\gg 1$, the dispersion relation (A.9) becomes

$$\omega\simeq-\frac{1}{\gamma t_{\mathrm{cool}}\Lambda_0}\left(\frac{\partial\mathcal{L}_0}{\partial\ln T_0}\right)_{P_0}-\frac{c_{\mathrm{s}}}{\gamma}\frac{k^2}{k_{\mathrm{K}}}=-\frac{\alpha-1}{\gamma t_{\mathrm{cool}}}-\frac{c_{\mathrm{s}}}{\gamma}\frac{k^2}{k_{\mathrm{K}}}. \tag{A.10}$$

The second term of the right-hand side in equation (A.10) indicates the stabilization effect due to the heat conduction. Without the heat conduction, the growth rate approaches the constant value. The gas is unstable if

$$\left(\frac{\partial\mathcal{L}_0}{\partial T}\right)_P=\alpha-1<0. \tag{A.11}$$

This mode is called isobaric mode where the gas grows maintaining pressure equilibrium with its surroundings since the scale of the perturbation, $\sim 1/k$, is smaller than λ_{cool}. The heat conduction completely stabilizes the thermal instability for

$$k>k_{\mathrm{crit}}=\sqrt{k_{\mathrm{K}}\frac{1}{\lambda_{\mathrm{cool}}}\frac{1}{\gamma\Lambda_0}\left(\frac{\partial\mathcal{L}_0}{\partial\ln T_0}\right)_{P_0}}\sim\sqrt{\frac{k_{\mathrm{K}}}{\lambda_{\mathrm{cool}}}}. \tag{A.12}$$

For the smaller wave number, the growth rate of the isobaric mode is smaller because of finiteness of the sound speed. Therefore, the dispersion relation peaks at the wave number that is order of a fraction of $\sim \sqrt{k_{\rm K}/\lambda_{\rm cool}}$.

A.2.2 $k\lambda_{\rm cool} \ll 1$

For $k\lambda_{\rm cool} \ll 1$, The dispersion relation (A.9) becomes

$$\omega^2 \left\{ \omega + \frac{1}{t_{\rm cool}\Lambda_0} \left(\frac{\partial \mathcal{L}_0}{\partial \ln T_0} \right)_\rho \right\} = 0. \tag{A.13}$$

Therefore, there are three solutions,

$$\omega_1 = -\frac{1}{t_{\rm cool}\Lambda_0} \left(\frac{\partial \mathcal{L}_0}{\partial \ln T_0} \right)_\rho, \quad \omega_{2,3} = 0. \tag{A.14}$$

The solution, ω_1 is unstable if

$$\left(\frac{\partial \mathcal{L}_0}{\partial T_0} \right)_\rho = \alpha < 0, \tag{A.15}$$

the gas is unstable with the finite growth rate for $\tilde{k} \ll 1$. This is the isochoric mode. On the other hand, if the gas is stable in the isochoric mode, the growth rate declines to zero for $k\lambda_{\rm cool} \ll 1$. The solutions $\omega_{2,3} = 0$ can be expanded in the power of k as

$$\omega_{2,3}^2 = -\frac{c_{\rm s}^2 k^2}{\gamma} \frac{\left(\dfrac{\partial \mathcal{L}_0}{\partial \ln T_0} \right)_P}{\left(\dfrac{\partial \mathcal{L}_0}{\partial \ln T_0} \right)_\rho} = -\frac{\alpha - 1}{\alpha\gamma} c_{\rm s}^2 k^2. \tag{A.16}$$

Appendix B

Thermal Instability of Isochorically Cooling Gas

We consider initially spatially uniform static gas. From the continuity equation and equation of motion, the gas remains at rest and the density remains constant. Therefore, the gas cools isochorically. Since the gas distributes uniform, instead of equation (3.1), we use the following zooming coordinate,

$$\begin{pmatrix} t \\ \vec{x} \end{pmatrix} \Rightarrow \begin{pmatrix} \tau \\ \vec{\xi} \end{pmatrix} = \begin{pmatrix} -\dfrac{\ln t_*}{1-\omega} \\ \vec{x}/x_0(t) \end{pmatrix}. \tag{B.1}$$

Basic equations are

$$\frac{\partial \ln \Omega}{\partial \tau} + \vec{\nabla}_\xi \cdot (\Omega \vec{V}) = 0, \tag{B.2}$$

$$\frac{\partial \vec{V}}{\partial \tau} + \vec{V} \cdot \vec{\nabla}_\xi \vec{V} + \frac{1}{\Omega} \vec{\nabla}_\xi \Pi = \omega \vec{V}, \tag{B.3}$$

and

$$\frac{1}{\gamma - 1} \left(\frac{\partial}{\partial \tau} + \vec{V} \cdot \vec{\nabla}_\xi \right) \left(\ln \Pi \Omega^{-\gamma} \right) = \frac{2\omega}{\gamma - 1} - \gamma^\alpha \Omega^{2-\alpha} \Pi^{\alpha - 1}, \tag{B.4}$$

where $\beta = 0$ from equation (2.13). The time evolution of the gas obeys the homologous solution with $\beta = 0$ that is derived in section 2.1.4,

$$\Omega(\vec{\xi}) = \Omega_0, \;\; \Pi(\vec{\xi}) = \Pi_0, \;\; V(\vec{\xi}) = 0. \tag{B.5}$$

From equations (2.61) and (2.34) with $\beta = 0$, the homologous solution becomes

$$\Omega_0(\vec{\xi}) = \frac{1}{\gamma(\gamma-1)} \left(\frac{2}{3-2\alpha} \right)^{3-2\alpha}, \quad \Pi_0(\vec{\xi}) = \frac{1}{\gamma^2(\gamma-1)} \left(\frac{2}{3-2\alpha} \right)^{5-2\alpha}, \quad \text{and} \quad \vec{V}(\vec{\xi}) = 0. \tag{B.6}$$

Perturbed variables are expressed as

$$\begin{aligned} \Omega(\tau,\vec{\xi}) &= \Omega_0\left(1+\delta\Omega(\tau)e^{i\vec{k}\cdot\vec{x}}\right) \\ \vec{V}(\tau,\vec{\xi}) &= \delta\vec{V}(\tau)e^{i\vec{k}\cdot\vec{x}} \\ \Pi(\tau,\vec{\xi}) &= \Pi_0\left(1+\delta\Pi(\tau)e^{i\vec{k}\cdot\vec{x}}\right) \end{aligned} \tag{B.7}$$

Substituting equation (B.8) into basic equations (B.2)-(B.4), the perturbation equations can be written as

$$\frac{\partial\delta\Omega}{\partial\tau}+\vec{\kappa}(\tau)i\delta\vec{V}=0, \tag{B.8}$$

$$\frac{\partial\delta\vec{V}}{\partial\tau}+\frac{4\omega^2}{\gamma}i\vec{\kappa}(\tau)i\delta\Pi=\omega\delta\vec{V}, \tag{B.9}$$

and

$$\frac{\partial\delta\Pi}{\partial\tau}-\gamma\frac{\partial\delta\Omega}{\partial\tau}=-\left(2-\alpha\right)\gamma\epsilon_0\delta\Omega-\left(\alpha-1\right)\gamma\epsilon_0\delta\Pi, \tag{B.10}$$

where we use $\kappa(\tau)=k\lambda_{\rm cool}(\tau)$. If time evolution of the unperturbed state is slower than the growth of perturbation, time evolution of the unperturbed state is neglibible. In the situation, since we can set κ to be constant with time, the perturbed variables can be expanded with respect to time, $\delta Q\propto e^{(1-\omega)\sigma\tau}$ ($\delta Q=\delta\Omega,\ \delta\Pi,\ \delta\vec{V}$). The condition under which the static approximation is valid is given by

$$\Sigma\gg\frac{3-2\alpha}{2(1-\alpha)}. \tag{B.11}$$

From equations (B.8)-(B.10), the dispersion relation is given by

$$\sigma^3-\sigma^2+\frac{2}{(3-2\alpha)^2}\left\{1-\alpha+2\kappa^2\right\}\sigma-\frac{8(2-\alpha)}{\gamma(3-2\alpha)^3}\kappa^2=0. \tag{B.12}$$

Figure B.1 shows the dispersion relation for $\alpha=0.5$. Figure B.1 is very similar to figure 3.3 for $\eta=0.1$.

For $\kappa\gg1$, the dispersion relation becomes

$$\Sigma=\frac{\sigma}{1-\omega}=\frac{(2-\alpha)}{\gamma(1-\alpha)}. \tag{B.13}$$

This corresponds to the isobaric mode that growth rate is the same as equation (3.33) with $\eta=0$. The same growth rate was derived by Burkert and Lin (2000). Since the unperturbed density is constant with time, the isobaric mode can grow.

For $\kappa\ll1$, the dispersion relation becomes

$$\Sigma=0,\quad\frac{1}{2(1-\alpha)},\quad\text{and}\quad1, \tag{B.14}$$

that correspond to $k=0$, shear and non-interactive modes.

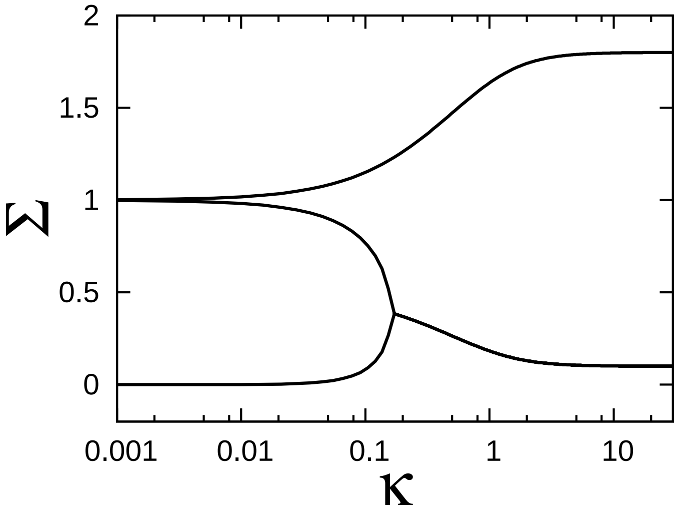

Figure B.1: Dispersion relation for $\alpha = 0.5$.

Appendix C

Derivation of Basic Equations in the Zooming Coordinate

Here, we present preparation for derivation of basic equations (2.16)-(2.18) in the zooming coordinate given by Eq. (3.1). In the zooming coordinate, the physical variables, $Q(t,x,y)$, are given by the following unified form:

$$Q(t,x,y) = Q_0(t)\Theta(\tau,\xi,y), \quad Q_0(t) \propto t_*^{-q/(1-\omega)}, \tag{C.1}$$

where $Q(t,x,y)$ corresponds to $[\rho, v_x, v_y, P]$ (see Eq. 3.2), and $\Theta = [\Omega, V_x, V_y, \Pi]$ are the physical variables in the zooming coordinate. From Eqs. (2.6)-(2.64), a parameter, q, is given by

$$q = \begin{cases} -\beta & \text{for } \; Q = \rho \\ -\omega & \text{for } \; Q = v_x, \; v_y \\ -2\omega - \beta & \text{for } \; Q = P \end{cases} . \tag{C.2}$$

The temporal and spatial derivatives of $Q(t,x,y)$ in the ordinary coordinate can be expressed in the zooming coordinate as

$$\begin{aligned} \left(\frac{\partial Q}{\partial t}\right)_{x,y} &= \frac{\mathrm{d}Q_0(t)}{\mathrm{d}t}\Theta + Q_0(t)\frac{\mathrm{d}\tau}{\mathrm{d}t}\frac{\partial\Theta}{\partial\tau} + Q_0(t)\left(\frac{\partial\xi}{\partial t}\right)_x\frac{\partial\Theta}{\partial\xi} \\ &= \frac{v_0(t)}{x_0(t)}Q_0(t)\left[q\Theta + \frac{\partial\Theta}{\partial\tau} + \xi\frac{\partial\Theta}{\partial\xi}\right], \end{aligned} \tag{C.3}$$

$$\left(\frac{\partial Q}{\partial x}\right)_{t,y} = \frac{Q_0(t)}{x_0(t)}\frac{\partial\Theta}{\partial\xi}, \quad \text{and} \quad \left(\frac{\partial Q}{\partial y}\right)_{t,x} = Q_0(t)\frac{\partial\Theta}{\partial y}, \tag{C.4}$$

respectively, where we use

$$\frac{v_0(t)}{x_0(t)} = -\frac{\dot{x}_0(t)}{x_0(t)} = \frac{1}{(1-\omega)t_c t_*} \tag{C.5}$$

from Eq. (2.6). Using Eqs. (C.3) and (C.4), the Lagrangian time derivative of Q is given by

$$\begin{aligned}&\left(\frac{\partial}{\partial t}+v_0(t)V_x\frac{\partial}{\partial x}+v_0(t)V_y\frac{\partial}{\partial y}\right)Q(t,x,y)\\&=\frac{v_0(t)}{x_0(t)}Q_0(t)\left[q+\frac{\partial}{\partial \tau}+\left(V_x+\xi\right)\frac{\partial}{\partial \xi}+V_y x_0(t)\frac{\partial}{\partial y}\right]\Theta(\tau,\xi,y).\end{aligned}\tag{C.6}$$

Using Eqs. (C.3)-(C.6),

$$\frac{v_0(t)}{x_0(t)}=\gamma^{\alpha-1}\Lambda_0\rho_0(t)^{2-\alpha}P_0(t)^{\alpha-1},\ \ \text{and}\ \ P_0(t)=\frac{\rho_0(t)v_0(t)^2}{\gamma},\tag{C.7}$$

basic equations (2.16)-(2.18) are derived in the zooming coordinate.

Appendix D

Detailed Expression of A_{ik}

In this appendix, we provide the detailed expression of A_{ik} as

$$A_{11} = -\left(\frac{V_0^2 - X_0^2}{V_0}\right)(1-\omega)\Sigma - \frac{X_0^2}{\gamma}(\ln \Pi_0)' + \frac{X_0^2}{V_0}(\alpha - 2)\epsilon_0 \tag{D.1}$$

$$A_{12} = -V_0(\ln \Omega_0)' + (1-\omega)\Sigma - \omega + V_0' - \frac{X_0^2}{\gamma V_0}(\ln \Pi_0 \Omega_0^{-\gamma})', \tag{D.2}$$

$$A_{13} = \frac{X_0^2}{\gamma}\left[(\ln \Pi_0)' - \frac{(1-\omega)\Sigma + (\alpha-1)\gamma\epsilon_0}{V_0}\right], \tag{D.3}$$

$$A_{14} = -kx_0(t)V_0, \tag{D.4}$$

$$A_{21} = \frac{X_0^2}{\gamma}\left(V_0(\ln \Pi_0)' - (\alpha-2)\gamma\epsilon_0\right), \tag{D.5}$$

$$A_{22} = X_0^2(\ln \Omega_0)' - V_0\left\{(1-\omega)\Sigma - \omega + V_0'\right\} + \frac{X_0^2}{\gamma}(\ln \Pi_0 \Omega_0^{-\gamma})', \tag{D.6}$$

$$A_{23} = -V_0 A_{14}, \tag{D.7}$$

$$A_{24} = kx_0(t)X_0^2, \tag{D.8}$$

$$A_{31} = -X_0^2(\ln \Pi_0)' + (\alpha-2)V_0\gamma\epsilon_0, \tag{D.9}$$

$$A_{32} = \gamma\left\{-V_0(\ln \Omega_0)' + (1-\omega)\Sigma - \omega + V_0' - \frac{V_0}{\gamma}(\ln \Pi_0 \Omega_0^{-\gamma})\right\}, \tag{D.10}$$

$$A_{33} = X_0^2(\ln \Pi_0)' - V_0\{(1-\omega)\Sigma + (\alpha-1)\gamma\epsilon_0\}, \tag{D.11}$$

$$A_{34} = -\gamma kx_0(t)V_0, \tag{D.12}$$

$$A_{41} = 0, \tag{D.13}$$

$$A_{42} = 0, \tag{D.14}$$

$$A_{43} = -\frac{V_0^2 - X_0^2}{V_0} \left\{(1-\omega)\Sigma - \omega\right\}, \tag{D.15}$$

and

$$A_{44} = kx_0(t)(V_0^2 - X_0^2)\frac{X_0^2}{\gamma}. \tag{D.16}$$

Appendix E

Smoothed Particle Hydrodynamics

Smoothed particle hydrodynamics (SPH) is fully Lagrangian particle method (Gingold and Monaghan, 1977; Lucy, 1977), and widely used in astrophyics and many other fields. Since resolution of a high density region automatically increases, SPH is especially suited to problems which have a large density contrast. In this appendix, we review SPH and present test calculations.

E.1 Formulation

In SPH, the fluid is expressed as an ensamble of extended spherically symmetric gas particles. The density at the position $\vec{x}$ is given by

$$\rho(\vec{x}) = \sum_k m_k W(\vec{x} - \vec{x}_k, h), \tag{E.1}$$

where m_k indicates the mass of the k-th particle, $W(\vec{x}, h)$ is a spherically symmetric kernel function, and h is a parameter of the kernel function. The kernel function must satisfy the following conditions:

$$W(\vec{x}, h) = W(-\vec{x}, h), \tag{E.2}$$

$$\int W(\vec{x}, h) \mathrm{d}^3 x = 1, \tag{E.3}$$

and

$$\lim_{h \to 0} W(\vec{x}, h) = \delta(\vec{x}). \tag{E.4}$$

In this thesis, we use the following Gaussian kernel function:

$$W(\vec{x}, h) = \left(\frac{1}{h\sqrt{\pi}}\right)^d \exp\left[-\left(\frac{\vec{x}}{h}\right)^2\right], \tag{E.5}$$

where d is the number of dimensions. The smoothing length, h, indicates the size of particles. Each particle has different the smoothe length h_i that is defined by

$$h_i = \left(\frac{m_i}{\rho_i}\right)^{1/d}, \tag{E.6}$$

where h_i is the smoothing length of i-th particle. The density of i-th particle is given by

$$\rho_i = \sum_k m_k W\left(\vec{x}_i - \vec{x}_k, \bar{h}_{ik}\right), \tag{E.7}$$

where $\bar{h}_{ik}$ is a mean value of h_i and h_k. We adopt

$$\bar{h}_{ik} = \sqrt{\frac{h_i^2 + h_k^2}{2}} \tag{E.8}$$

as the mean smoothing length.

E.1.1 Equation of Motion and Energy Equation

Inutsuka (2002) developed Godunov SPH where the solution of Rimann solver is used to estimate the numerical flux between particles. This method has been originally developed in finite difference methods (Godunov, 1959; van Leer, 1997). In the Godunov SPH, equation of motion and energy equation are given by

$$\frac{\mathrm{d}\vec{v}_i}{\mathrm{d}t} = -\sum_k m_k P^* \left(\frac{1}{\rho_i^2} + \frac{1}{\rho_k^2}\right) \vec{\nabla} W(\vec{x}_i - \vec{x}_k, \bar{h}_{ik}) \tag{E.9}$$

and

$$\frac{\mathrm{d}e_i}{\mathrm{d}t} = \sum_k m_k P^* \left(\frac{1}{\rho_i^2} + \frac{1}{\rho_k^2}\right) \left(\vec{v}^* - \frac{\mathrm{d}\vec{x}_i}{\mathrm{d}t}\right) \cdot \vec{\nabla} W(\vec{x}_i - \vec{x}_k, \bar{h}_{ik}), \tag{E.10}$$

respectively, where e_i is the specific internal energy of i-th particle, P^* and $\vec{v}^*$ are the solution of the Riemann problem along the direction of $\vec{x}_i - \vec{x}_k$ that used density, pressure and velocity of each pair of particles. The detailed derivation of equations (E.9) and (E.10) are found in Inutsuka (2002). We use spatially second order Godunov SPH where linear interpolation of the physical variables is used when solving Riemann solver (van Leer, 1997).

If the gas is subject to cooling and heating, equation (E.10) becomes

$$\frac{\mathrm{d}e_i}{\mathrm{d}t} = \sum_k m_k P^* \left(\frac{1}{\rho_i^2} + \frac{1}{\rho_k^2}\right) \left(\vec{v}^* - \frac{\mathrm{d}\vec{x}_i}{\mathrm{d}t}\right) \cdot \vec{\nabla} W(\vec{x}_i - \vec{x}_k, \bar{h}_{ik}) - \mathcal{L}(\rho_i, T_i). \tag{E.11}$$

E.1.2 Implementation of Heat Conduction

Koyama and Inutsuka (2004) shows that the numerical code must include heat conduction and must resolve Field length in order to obtain converged results. Heat conduction term contains second derivative that is found to be very sensitive to particle disorder (Monaghan, 1988). Monaghan (1992) proposed the following implementation of heat conduction that does not contains second derivative of kneral function,

$$\frac{1}{\rho}\vec{\nabla}\cdot\left(K\vec{\nabla}T\right)\Big|_{\vec{x}=\vec{x}_i} = \sum_j \frac{m_j}{\rho_i\rho_j}\frac{(K_i+K_j)(T_i-T_j)}{|\vec{x}_i-\vec{x}_j|^2}\left(\vec{x}_i-\vec{x}_j\right)\cdot\vec{\nabla}_i W(\vec{x}_i-\vec{x}_k,\bar{h}_{ik}). \tag{E.12}$$

Since equation (E.12) is antisymmetric in the particles i and j, the energy conservation is guaranteed.

E.2 Test Calculations

In this section, we present test calculations to confirm that our code produces reliable results using two-dimensional SPH code.

E.2.1 Shock-tube Problem

We calculate shock-tube problems and compare the results with the exact solutions. The simulation box is a rigid rectangular box with $-0.5 < x < 0.5$, $-1/16 < y < 1/16$. The box is divided in two regions by $x = 0$ plane. The physical variables in the left and right region are denoted by subscript L and R, respectively.

Sod's solution

First, we use Sod's solution (Sod, 1978) where initial condition is given by

$$\begin{array}{ll} \rho_{\rm L} = 1, & \rho_{\rm R} = 0.125 \\ P_{\rm L} = 1, & P_{\rm R} = 0.1 \\ v_{\rm L} = 0, & v_{\rm R} = 0 \end{array} \quad . \tag{E.13}$$

The ratio of specific heats is $\gamma = 1.4$. The mass of the particle at the right-hand side, $m_{\rm R}$, is set to be $m_{\rm L}/8$. In other words, the initial smoothing length of the particle is assumed to be spatially uniform. The total number of particle is 2000. Figure E.1 shows the snapshots of the density, pressure, velocity and internal energy at $t = 0.2$. The red and blue dots denote the results by using second and first order accuracy SPH codes, respectively. The black lines denote the exact solution. From figure E.1, SPH calculation can reproduce the exact solution well.

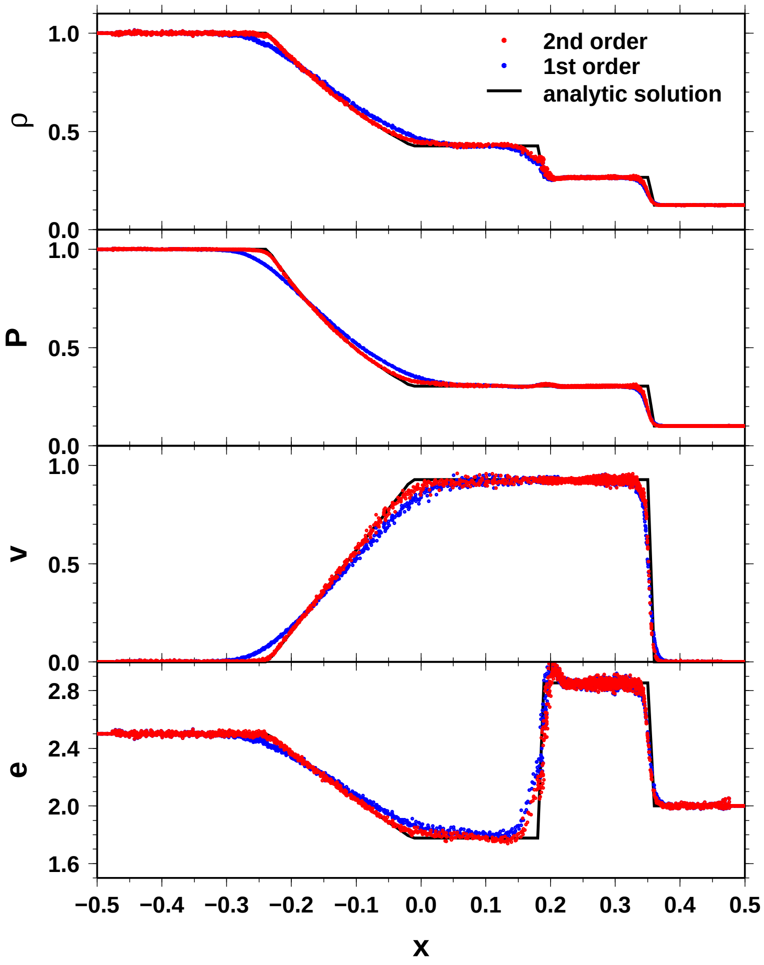

Figure E.1: Sod's solution. The red and blue dots denote the results by using second and first order SPH codes, respectively. The black lines denote the exact solution of Sod's solution.

Blast Wave

Next, we test SPH code for the case with very high mach number. The initial condition is

$$\begin{aligned} \rho_{\mathrm{L}} &= 1, & \rho_{\mathrm{R}} &= 1 \\ P_{\mathrm{L}} &= 3000, & P_{\mathrm{R}} &= 10^{-7} \ . \\ v_{\mathrm{L}} &= 0, & v_{\mathrm{R}} &= 0 \end{aligned} \tag{E.14}$$

The ratio of specific heats is $\gamma = 5/3$. The mach number is as large as 10^5. Figure E.2 shows the snapshots of the density, pressure, velocity and internal energy at $t = 0.005$. From figure E.2, it is clearly seen that the code can calculate stably and accurately the case with extreme high mach number problem.

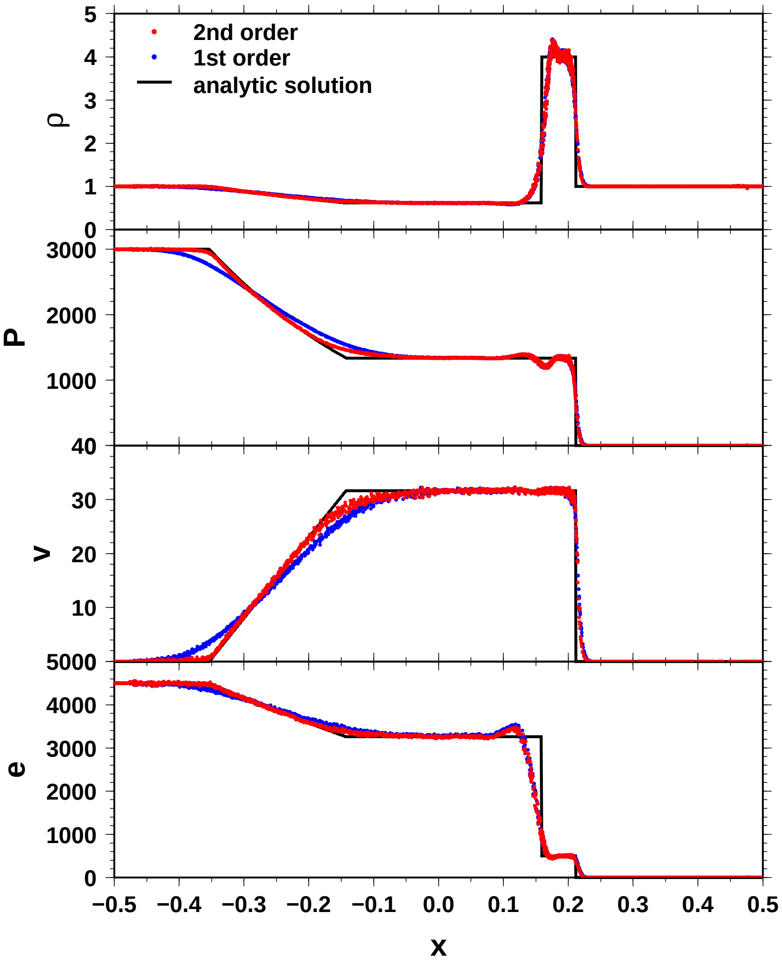

Figure E.2: The same as figure E.1 but for Blast wave.

Sjögreen test

We test the SPH code against supersonic expansion, or Stögreen test. The initial condition is given by

$$\begin{aligned} \rho_{\mathrm{L}} &= 1, & \rho_{\mathrm{R}} &= 1 \\ P_{\mathrm{L}} &= 0.4, & P_{\mathrm{R}} &= 0.4 \ . \\ v_{\mathrm{L}} &= -2, & v_{\mathrm{R}} &= 2 \end{aligned} \tag{E.15}$$

The ratio of specific heats is $\gamma = 1.4$. Figure E.3 shows the snapshots of the density, pressure, velocity and internal energy at $t = 0.1$. By the supersonic expansion, the cavity forms in the vicinity of the initial contact front, $x = 0$. Our code can reproduce the exact solution around head of the rarefaction wave at $x \sim \pm 0.3$. However, there is a significant error around $x \sim 0$. The second-order code produces better result than the first-order code around $x \sim 0$.

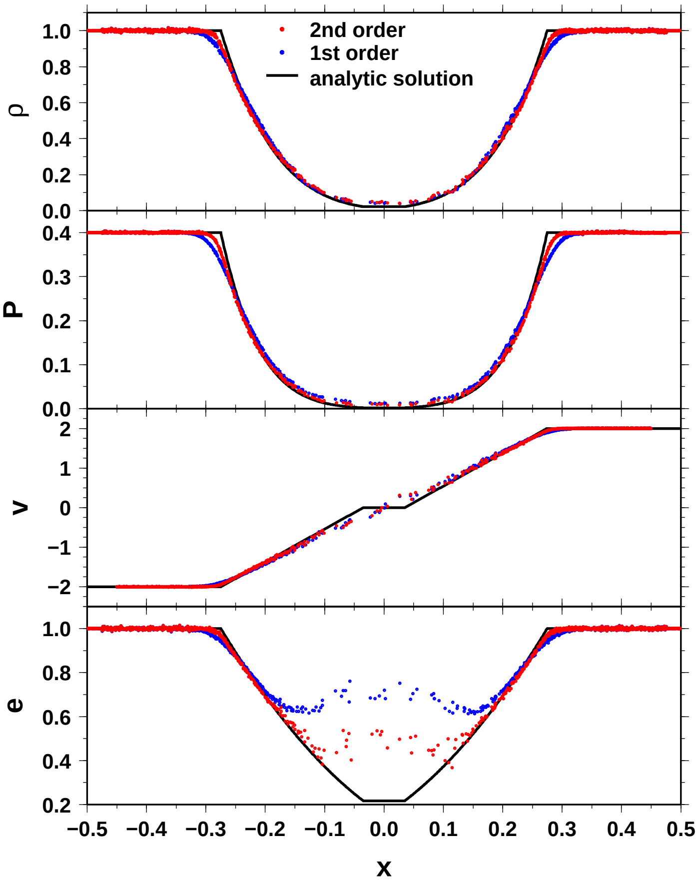

Figure E.3: The same as figure E.1 but for Sjögreen test.

Isothermal Colliding Wall

We consider a colliding flow where the initial condition is given by

$$\begin{aligned} &\rho_{\mathrm{L}} = 1, \quad &&\rho_{\mathrm{R}} = 1 \\ &P_{\mathrm{L}} = 1, \quad &&P_{\mathrm{R}} = 1 \\ &v_{\mathrm{L}} = 9.9, \quad &&v_{\mathrm{R}} = -9.9 \end{aligned} \quad . \tag{E.16}$$

The mach number is as large as 10. The equation of state is assumed to be isothermal. The gas compressed and the density increases up to 100 times. Two shock waves propagate outward. Figure E.4 shows the snapshots of the density, velocities in the x, and y direction, and distribution of SPH particles in the (x, y) plane. There is not particle penetration at the initial contact front. The density fluctuation in the shocked region is reasonably small.

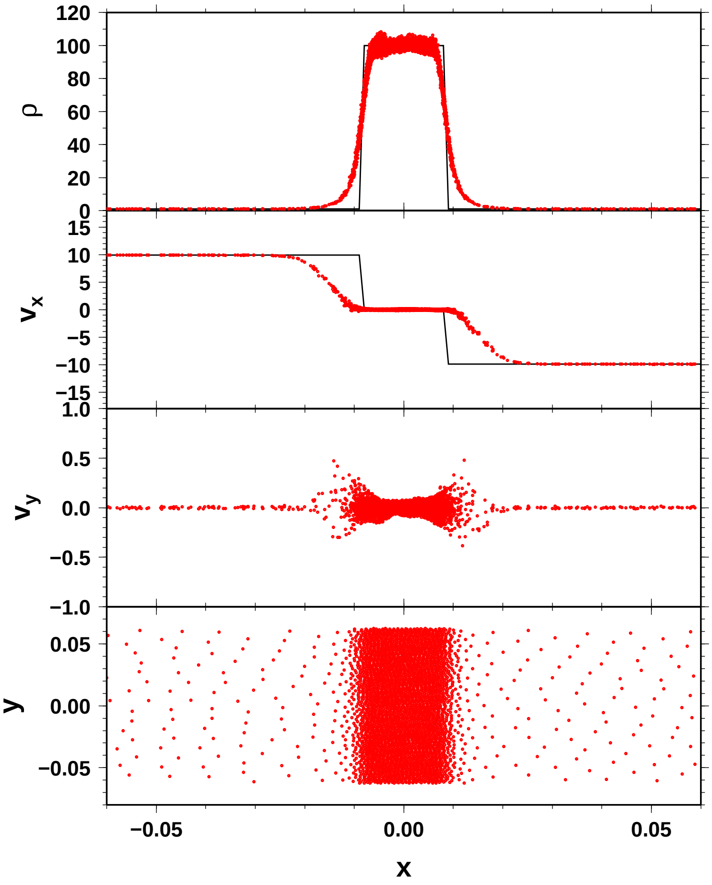

Figure E.4: Isothermal colliding wall test. The red dots denote the results of SPH calculation. The black lines indicates the analytic solution.

E.2.2 Kelvin-Helmholtz Instability

We consider Kelvin-Helmholtz instability across a density jump in two dimensions. The computational domain is $-1/6 < x < 1/6$, $-1/3 < y < 1/3$ and is divided into two regions, region "1" for $|y| < 1/6$ and region "2" elsewhere. Equal-mass particles are distributed randomly such that $\rho_1 = 2$ in region 1 and $\rho_2 = 1$ in region 2. The two regions are in pressure equilibrium with $P = 2.5$. A shear flow is set up in the x-direction with velocity $v_1 = v_{\rm shear}\rho_2/(\rho_1+\rho_2)$ in region 1 and $v_2 = -v_{\rm shear}\rho_1/(\rho_1+\rho_2)$ in region 2, where $v_{\rm shear} = v_1 - v_2 = 0.8$ is the shear velocity. To induce Kelvin-Helmholtz instability, we add the following velocity perturbation into the initial condition,

$$v_y = \begin{cases} 0.1 v_{\rm shear} \sin\left[2\pi x/\lambda\right] & \text{for} \quad |y - 1/6| < 0.025 \\ -0.1 v_{\rm shear} \sin\left[2\pi x/\lambda\right] & \text{for} \quad |y + 1/6| < 0.025 \end{cases}, \tag{E.17}$$

where $\lambda = 1/6$. The parameters ρ_1, ρ_2, and $v_{\rm shear}$ is set to 2, 1, and 0.8, respectively.

From linear analysis of incompressible fluid (Chandrasekhar, 1961) that is applicable because the shearing motion is subsonic, the growth timescale of Kelvin-Helmholtz instability is given by

$$t_{\rm KH} = \frac{\lambda(\rho_1+\rho_2)}{v_{\rm shear}\sqrt{\rho_1\rho_2}}. \tag{E.18}$$

In the initial setup shown above, it is found that $t_{\rm KH} = 0.43$.

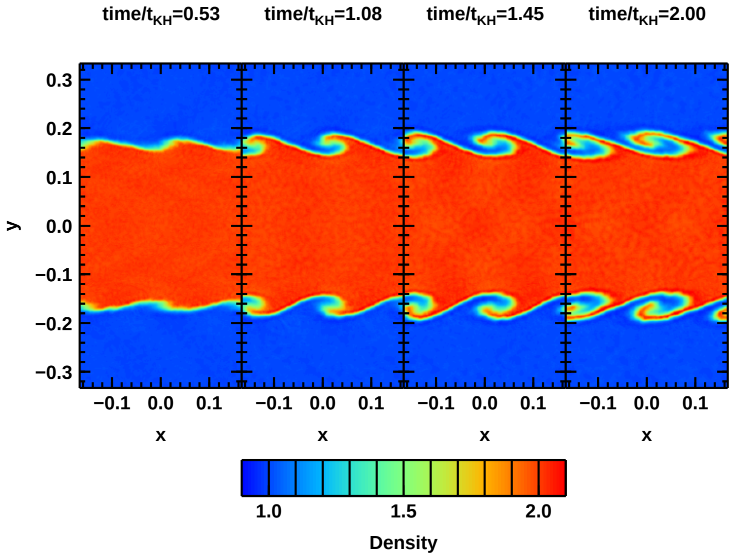

Figure E.5: Color maps of density fields at $t/t_{\rm KH} = 0.54$, 1.00, 1.46, and 2.01.

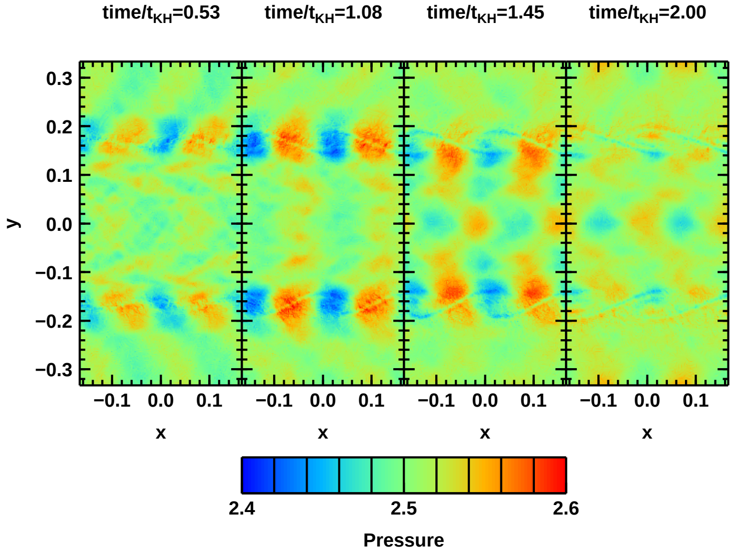

Figure E.6: The same as figure E.5 but for the pressure field.

Figure E.5 shows color maps of the density fields at $t/t_{\mathrm{KH}} = 0.54$, 1.00, 1.46, and 2.01. At $t/t_{\mathrm{KH}} = 0.51$, the contact surface fluctuates due to initial velocity perturbation. It is clearly seen that the rolled vortices develop well around the contact surface at the later snapshots in figure E.5. Figure E.6 is the same as figure E.5 but for the pressure field. There are small wiggles of the pressure at the contact surface at each snapshot.

E.2.3 Thermal Relaxation by Heat Conduction

To test the heat conduction term (E.12), we calculate the following diffusion equation,

$$\frac{\mathrm{d}e}{\mathrm{d}t} = \frac{K}{\rho}\vec{\nabla}^2 T, \tag{E.19}$$

where we assume that K and the density are constant. Using $e = C_V T$, equation (E.19) can be rewritten as

$$\frac{\mathrm{d}e}{\mathrm{d}t} = \frac{K}{C_V\rho}\vec{\nabla}^2 e. \tag{E.20}$$

We consider the following initial distribution of energy,

$$e(\vec{x}, t = 0) = 1 + \frac{1}{2}\cos(kx). \tag{E.21}$$

The density is assumed to be constant with time. Solving equation (E.20) analytically, one can get

$$e_{\mathrm{ana}}(\vec{x}, t) = 1 + \frac{1}{2}\cos(kx)\, e^{-t/\tau}, \tag{E.22}$$

where

$$\tau = \frac{C_V \rho}{K k^2}. \tag{E.23}$$

Parameters k, ρ, and K are set to 2π, 1, and C_V, respectively, and computational domain is $-0.5 < x, y < 0.5$. Periodic boundary conditions are imposed in the x and y directions.

Figures E.7a and E.7b show snapshots of the density and $(e - e_{\rm ana})/e_{\rm ana}$ at $t = 0$, 0.01, 0.02, and 0.04 as a function of x, respectively. Figure E.7b shows that our code can produce the correct results within $\sim 0.1\%$ accuracy.

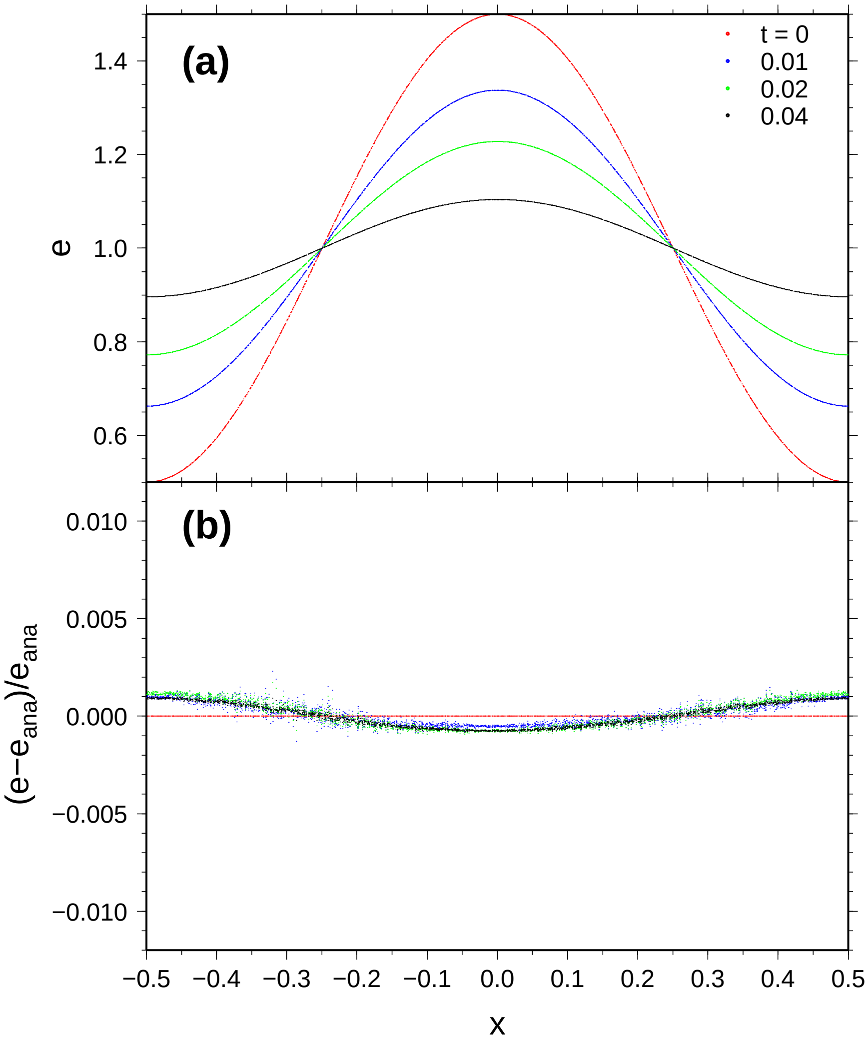

Figure E.7: (a):Snapshots of the density at $t = 0$, 0.01, 0.02, and 0.04 as (b):$(e - e_{\rm ana})/e_{\rm ana}$.

E.2.4 Thermal Instability

We investigate thermal instability of spatially uniform gas in thermal equilibrium state and compare results of SPH calculation with the linear analysis by Field (1965). We adopt the power law net cooling rate (1.2) with $\alpha = 0.5$. The critical wave number is set to $k\lambda_{\rm cool} = 10$. We consider two cases of $k\lambda_{\rm cool} = 2$ and $k\lambda_{\rm cool} = 3$.

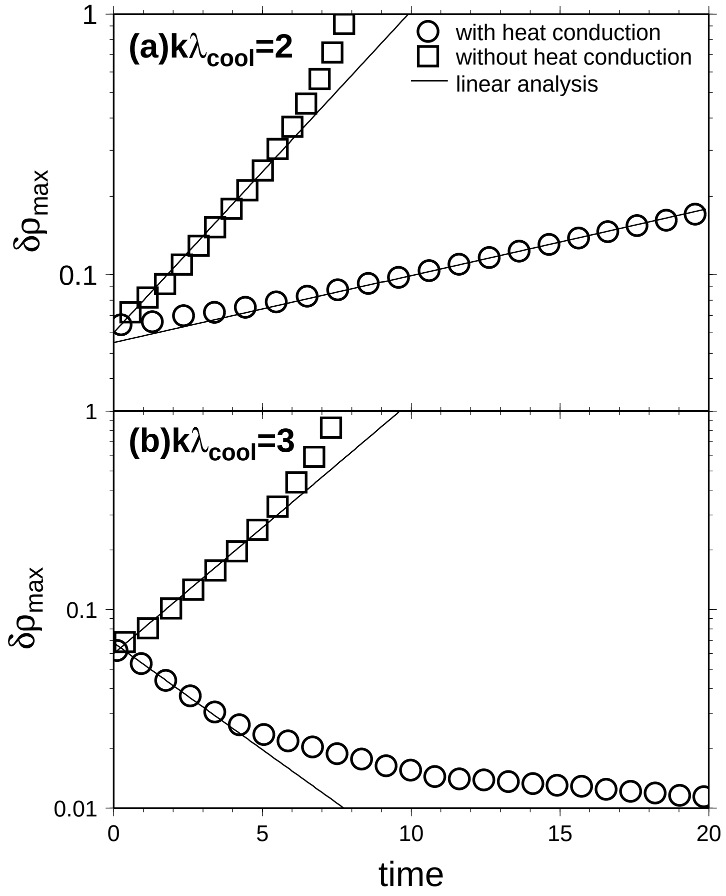

Figure E.8: Time evolution of $\delta\rho_{\rm max}$ for (a)$k\lambda_{\rm cool} = 2$ and (b)$k\lambda_{\rm cool} = 3$. The open boxes and circles correspond to results with and without heat conduction. The solid lines indicates results of the linear analysis.

Figures E.8a and E.8b show time evolution of $\delta\rho_{\rm max}$ for $k\lambda_{\rm cool} = 2$ and 3, respectively. The open boxes and circles correspond to results with and without heat conduction. The solid lines indicates results of the linear analysis. Figure E.8a shows that perturbations with heat conduction grow slower than that without heat conduction, and both results agree with prediction from the linear analysis. Figure E.8b shows that perturbation with heat conduction completely stabilized by heat conduction.

References

E. Audit and P. Hennebelle. *Astrophys. J*, 433:1, (2005).

E. L. O. Bakes and A. G. G. M. Tielens. *Astrophys. J*, 427:822–838, (1994).

S. A. Balbus. *Astrophys. J*, 303:79, (1986).

S. Bouquet, M. R. Feix, E. Fijalkow, and A. Munier. *Astrophys. J*, 293:494–503, (1985).

C. S. Bowyer, G. B. Field, and J. E. Mack. *Nature*, 217:32, (1968).

R. Braun and N. Kanekar. *Astron. & Astrophys.*, 436:L53–L56, (2005).

A. Burkert and D. N. C. Lin. *Astrophys. J*, 537:270–282, (2000).

S. Chandrasekhar. International Series of Monographs on Physics. Clarendon, Oxford, (1961).

B. G. Clark. *Astrophys. J*, 142:1398, (1965).

B. G. Clark, V. Radhakrishnan, and R. W. Wilson. *Astrophys. J*, 135:151, (1962).

D. P. Cox and B. W. Smith. *Astrophys. J*, 189:L105–L108, (1974).

A. Dalgarno and R. McCray. *Annu. Rev. Astron. Astrophys.*, 10:375, (1972).

T. M. Dame, H. Ungerechts, R. S. Cohen, I. A. de Grenier, J. May, D. C. Murphy, L. A. Nyman, and P. Thaddeus. *Astrophys. J*, 322:706–720, (1987).

T. M. Dame, D. Hartmann, and P. Thaddeus. *Astrophys. J*, 322:547–792, (2001).

Draine. *Astrophys. J*, 36:595–619, (1978).

H. I. Ewen and E. M. Purcell. *Nature*, 168:356, (1951).

G. B. Field. *Astrophys. J*, 142:531, (1965).

G. B. Field, D. W. Goldsmith, and H. J. Habing. *Astrophys. J*, 155:149, (1969).

I. Fouxon, B. Meerson, M. Assaf, and Eli Livne. *Phys. Fluid.*, 19:093303, (2007).

J. Franco and D. P. Cox. *Astrophys. J*, 273:243, (1983).

C. F. Gammie and E. Ostriker. *Astrophys. J*, 466:814–830, (1996).

R. A. Gingold and J. J. Monaghan. *Mon. Not. R. Astron. Soc.*, 171:375–389, (1977).

S. K. Godunov. *Math. Sbornik*, 47:271, (1959).

P. M. Gondhalekar and R. Wilson. *Astron. & Astrophys.*, 38:329, (1975).

H. J. Habing. *Bull. Astr. Inst. Netherlands*, 19:421, (1968).

J. P. Hagen and E. F. McClain. *Astrophys. J*, 120:368, (1954).

J. P. Hagen, A. E. Lilley, and E. F. McClain. *Astrophys. J*, 122:361, (1955).

T. Hanawa and T. Matsumoto. *Astrophys. J*, 521:703–707, (1999).

C. Heiles. *ApJS*, 55:585, (1984).

C. Heiles. *Astrophys. J*, 229:533, (1979).

C. Heiles and T. H. Troland. *Astrophys. J*, 586:1067–1093, (2003).

F. Heitsch and L. W. Hartmann. *Astrophys. J*, 689:290–301, (2008).

F. Heitsch, A. Burkert, L. W. Hartmann, A. D. Slyz, and J. E. Devriendt. *Astrophys. J*, 633:L113–L116, (2005).

F. Heitsch, A. D. Slyz, J. E. G. Devriendt, L. W. Hartmann, and A. Burkert. *Astrophys. J*, 648:1052–1065, (2006).

F. Heitsch, L. W. Hartmann, and A. Burkert. *Astrophys. J*, 683:786–795, (2008).

F. Heitsch, J. M. Stone, and L. W. Hartmann. *Astrophys. J*, 695:248–258, (2009).

P. Hennebelle and E. Audit. *Astron. & Astrophys.*, 465:431–443, (2007).

P. Hennebelle and T. Passot. *Astron. & Astrophys.*, 448:1083–1093, (2006).

P. Hennebelle and M. Pèrault. *Astron. & Astrophys.*, 359:1124–1138, (2000).

P. Hennebelle and M. Pèrault. *Astron. & Astrophys.*, 351:309–322, (1999).

P. Hennebelle, E. Audit, and M. A. Miville-Deschênes. *Astron. & Astrophys.*, 465:445–456, (2007).

P. Hennebelle, E. Banerjee, Vàzquez-Semadeni, R. S. Klessen, and E. Audit. *Astron. & Astrophys.*, 486:L43–L46, (2008).

D. Hollenbach and C. F. McKee. *Astrophys. J*, 342:306–336, (1989).

C. Hunter. *Astrophys. J*, 218:834–845, (1977).

T. Inoue and S. Inutsuka. *Astrophys. J*, 687:303–310, (2008).

T. Inoue and S. Inutsuka. *Astrophys. J*, 704:161–169, (2009).

T. Inoue, S. Inutsuka, and H. Koyama. *Astrophys. J*, 652:1331–1338, (2006).

T. Inoue, S. Inutsuka, and H. Koyama. *Astron. & Astrophys.*, 658:L99–L102, (2007).

S. Inutsuka. *J. Comput. Phys*, 179:238, (2002).

K. Iwasaki and T Tsuribe. *Mon. Not. R. Astron. Soc.*, 387:1554, (2008).

K. Iwasaki and T Tsuribe. *Astron. & Astrophys.*, 508:725–735, (2009).

E. B. Jenkins and D. A. Meloy. *Astrophys. J*, 193:L121–L125, (1974).

P. M. Kalberla, W. B. Burton, D. Hartmann, E. M. Arnal, E. Bajaja, R. Morras, and W. G. L. Pöppel. *Astron. & Astrophys.*, 440:775–782, (2005).

F. J. Kerr. *Annu. Rev. Astron. Astrophys.*, 7:39, (1969).

H. Koyama. PhD thesis, University of Tokyo, (2000).

H. Koyama and S. Inutsuka. *Astrophys. J*, 532:980–993, (2000).

H. Koyama and S. Inutsuka. *Astrophys. J. Lett*, 564:L97–L100, (2002).

H. Koyama and S. Inutsuka. *Astrophys. J*, 602:L25–L28, (2004).

L. D. Landau and E. M. Lifshitz. Pergamon, New York, (1959).

R Larson. *Mon. Not. R. Astron. Soc.*, 145:271, (1969).

R. B. Larson. *Mon. Not. R. Astron. Soc.*, 186:479–490, (1979).

R. B. Larson. *Mon. Not. R. Astron. Soc.*, 194:809–826, (1981).

L. B. Lucy. *Astron. J*, 82:1013, (1977).

M. Mac Low, R. S. Klessen, A. Burkert, and M. D. Smith. *Phys. Rev. Lett.*, 80:2754, (1998).

D. McCammon and W. T. Sanders. *Annu. Rev. Astron. Astrophys.*, 28:657, (1990).

N. M. McClure-Griffiths, J. M. Dickey, B. M. Gaensler, and A. J. Green. *Astrophys. J*, 578: 176, (2002).

C. F. McKee and J. P. Ostriker. *Astrophys. J*, 218:148–169, (1977).

S. McNamara. *Phys. Fluids A*, 5:3056–3070, (1993).

J. J. Monaghan. *Comput. Phys. Comm.*, 48:89, (1988).

J. J. Monaghan. *Annu. Rev. Astron. Astrophys.*, 30:543, (1992).

C. A. Muller and J. H. Oort. *Nature*, 168:357, (1951).

P. C. Myers. *Astrophys. J*, 171:375–389, (1977).

J. H. Oort, F. J. Kerr, and G. Westerhout. *Mon. Not. R. Astron. Soc.*, 118:379, (1958).

P. Padoan and øA. Nordlund. *Astrophys. J*, 526:279–294, (1999).

Parker. *Astrophys. J*, 117:431, (1953).

M. V. Penston. *Mon. Not. R. Astron. Soc.*, 145:457, (1969).

J. B. Rogerson, D. G. York, J. F. Drake, E. B. Jenkins, D. C. Morton, and L. Spitzer. *Astrophys. J*, 181:L110–L115, (1973).

B. D. Savage, K. R. Sembach, E. B. Jenkins, J. M. Shull, D. G. York, G. Sonneborn, H. M. Moos, S. D. Friedman, J. C. Green, W. R. Oegerle, W. P. Blair, J. W. Kruk, and E. M. Murphy. *Astrophys. J*, 538:L27–L30, (2000).

J. Schwarz, R. McCray, and R. F. Stein. *Astrophys. J*, 175:673–686, (1972).

J. A. Sellwood and S. A. Balbus. *Astrophys. J*, 511:660, (1999).

F. H. Shu. *Astrophys. J*, 214:488, (1977).

J. M. Shull and M. E. van Steenberg. *Astrophys. J*, 298:268, (1985).

G. A. Sod. *J. Comput. Phys*, 27:1, (1978).

S. Stanimirović and C. Heiles. *Astrophys. J*, 631:371–375, (2005).

R. S. Sutherland and M. A. Dopita. *Astrophys. J*, 88:253–327, (1993).

B. van Leer. *J. Comput. Phys*, 135:229–248, (1997).

E. Vàzquez-Semadeni, D. Ryu, T. Passot, R. F. González, and A. Gazol. *Astrophys. J*, 643: 245–259, (2006).

E. Vàzquez-Semadeni, G. C. Gomez, A. K. Jappsen, J. Ballesteros-Paredes, R. F. Gonzalez, and R. S. Klessen. *Astrophys. J*, 657:870–883, (2007).

E. T. Vishniac. *Astrophys. J*, 428:186–208, (1994).

H. Weaver and S. R. W. Williams. *Astron. & Astrophys. Suppl.*, 8:1–503, (1973).

A. Whitworth and D. Summers. *Mon. Not. R. Astron. Soc.*, 214:1–25, (1985).

R. W. Wilson, K. B. Jefferts, and A. A. Penzias. *Astrophys. J*, 161:L43–L44, (1970).

C. F. Wolfire, M. G. McKee, D. Hollenbach, and A. G. G. M. Tielens. *Astrophys. J*, 587: 278, (2003).

M. G. Wolfire, D. Hollenbach, C. F. McKee, A. G. G. M. Tielens, and E. L. O. Bakes. *Astrophys. J*, 443:152, (1995).

Y. B. Zel'dovich and Y. P. Raizer. New York: Academic Press, (1967).